METAL OXIDE REINFORCED/DECORATED POLYMERS AS HIGH PERMITTIVITY DIELECTRICS FOR ENERGY STORAGE DEVICES

Thesis

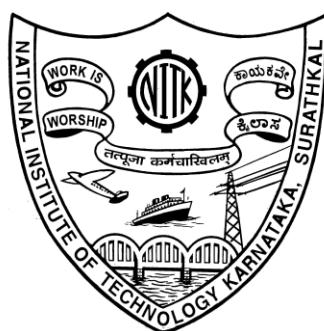Submitted in partial fulfillment of the requirements for the degree of

DOCTOR OF PHILOSOPHY

By

KISHOR KUMAR M J

(Registration No: 155097CH15F05)

DEPARTMENT OF CHEMICAL ENGINEERING

NATIONAL INSTITUTE OF TECHNOLOGY KARNATAKA

SURATHKAL

NOVEMBER, 2020

DECLARATION

I hereby *declare* that the Research Thesis entitled **"Metal oxide reinforced/decorated polymers as high permittivity dielectrics for energy storage devices"** which is being submitted to the National Institute of Technology Karnataka, Surathkal in partial fulfillment of the requirements for the award of the Degree of **Doctor of Philosophy** in the **Department of Chemical Engineering**, is a *bonafide report of the research work carried out by me*. The material contained in this Research Thesis has not been submitted to any University or Institution for the award of any degree.

KISHOR KUMAR M. J.

Registration number: 155097CH15F05

Department of Chemical Engineering

Place: NITK, Surathkal

Date: 18.11.2020

C E R T I F I C A T E

This is to certify that the Research Thesis entitled "**Metal oxide reinforced/decorated polymers as high permittivity dielectrics for energy storage devices**" submitted by **Mr. Kishor Kumar M J** (Register Number: 155097CH15F05) as the record of the research work carried out by him, is *accepted as the Research Thesis submission* in partial fulfillment of the requirements for the award of degree of Doctor of Philosophy.

Chairman- DRPC

Dr. Prasanna B. D.

Associate Professor and Head

Department of Chemical Engineering

NITK Surathkal

HEAD OF THE DEPARTMENT
CHEMICAL ENGINEERING
National Institute of Technology Karnataka, Surathkal
P.O. Srinivasnagar - 575 025, D.K., Mangalore

Research Supervisor

Dr. Jagannathan T. K.

Assistant Professor

Department of Chemical Engineering

NITK Surathkal

ACKNOWLEDGMENT

KISHOR KUMAR M. J.

ABSTRACT

High dielectric permittivity (high-k) materials are essential in fabricating energy storage devices, thin-film transistors, and piezoelectric devices. Solution-processable dielectrics are more desirable in energy storage film capacitors, and functional electronics, since they are cost-effective and can be produced in large quantities. The solution-process assisted by ultrasound is a well-known method as it provides the possibility of tuning properties of subsequent products by easily adjusting the precursor solutions. In this work, three categories of dielectrics, such as metal oxide-based dielectrics, namely, lanthanum cerium oxide (LCO), lanthanum zirconium oxide (LZO); polymer composite dielectrics, namely, polymethyl methacrylate (PMMA)-LZO and polyvinylidene fluoride-co-hexafluoropropylene (PVDF-HFP)-LZO; anisotropic dielectrics such as polystyrene-iron oxide (PS-Fe_3O_4) patchy particles and lanthanum oxide-zirconium oxide (La_2O_3-ZrO_2) dumbbell-shaped Janus particles, were fabricated at low temperatures using a sonochemical approach. In polymer composites, the main emphasis was on obtaining a uniform distribution of high-k LZO filler into a PMMA and PVDF-HFP matrix to improve their dielectric permittivity and energy storage density while lowering the dielectric loss. The effect of LZO content on dielectric properties and optimum LZO loading to achieve improved energy storage density of the films was studied. The enhanced energy storage density of 5.94 J/cm^3 at 63.6 MV/m breakdown strength for PMMA-LZO and 15.8 J/cm^3 at 545 MV/m for PVDF-HFP/LZO have been achieved.

Further, the fundamental insights into the role of the polymer-metal oxide (PS-Fe_3O_4 patchy particles) and metal oxide-metal oxide (La_2O_3-ZrO_2) interfaces on the dielectric properties have been addressed by considering experimental outcomes and computational simulations. Also, a new mechanism of charge build-up at these interfaces have been proposed. Computational outcomes reveal that the creation of interface bound-charges at the interface is predominantly responsible for the improved dielectric properties. Local morphology, dispersibility, interface area, crystallinity, and ionization of the metal oxides determine the overall dielectric permittivity of the film. Polymer-inorganic interface engineering and design open up a new area to develop hybrid materials for future energy storage systems.

NOMENCLATURE

LIST OF SYMBOLS AND UNITS

Symbol	Description
kg	kilogram
mg	milligram
g	gram
m	meter
nm	nanometer
μm	micrometer
cm	centimeter
h	hour
min	minute
s	second
wt %	weight %
vol %	volume %
V/m	Volts/meter
M	Mega
W	Watt
J	Joules
C	Capacitance
ε_r	relative permittivity
ε_o	vacuum permittivity
δ	loss factor
k	dielectric constant
Z	Impedance
θ	angle
σ	conductivity
P	Polarization
E	Electric field
X_e	susceptibility
ρ	density
F	Farad
Hz	Hertz
f	frequency
°C	degree Celsius
Pa	Pascal
N_a	Avogadro number

ABBREVIATIONS

MO	Metal oxide
High-k	High dielectric constant
LCO	Lanthanum cerium oxide
LZO	Lanthanum zirconium oxide
ITO	Indium tin oxide
PS	Polystyrene
PMMA	Polymethylmethacrylate
PVDF-HFP	Poly (vinylidene fluoride-co-hexafluoropropylene)
AIBN	Azobisisobutyronitrile
SEM	Scanning electron microscopy
TEM	Transmission electron microscopy
AFM	Atomic force microscopy
FTIR	Fourier transform and infrared radiation
XRD	X-ray diffraction
TGA	Thermogravimetric analysis
DTA	Differential thermal analysis
T_g	Glass transition temperature
RC	Resistive-capacitive
AC	Alternative current
DC	Direct current
BDS	Breakdown strength
PL	Photoluminescence
FE	ferroelectric
TFC	Thin-film capacitor
TFT	Thin-film transistor

CHAPTER 1

INTRODUCTION

Ever-increasing energy needs and fossil fuel depletion demand efficient ways of utilizing energy and the quest for sustainable and renewable resources. As a result, renewable energy production from solar and wind technologies is growing. Due to the intermittent evolution of such production and consumption requirements, the development of new, low-cost, and environmentally friendly energy conversion and storage systems such as batteries, electrochemical capacitors, fuel cells, and dielectric-based capacitors is of utmost importance. Among these energy-storage devices, dielectric capacitors provide intrinsically high-power density due to their rapid uptake and delivery of energy. They are therefore promising for the generation of high-performance electronics used in electric hybrid automobiles, transistors, inverters, medical devices, and electrical weapon systems (Dang et al., 2013). The capacitor, which stores electrical energy, restricts the flow of direct current (DC) and enables the flow of alternative current (AC), comprises simply of two parallel conductive electrodes separated by a dielectric material. Dielectric materials are the critical component responsible for the performance of capacitors.

The majority of the dielectric materials that are commercially used belong to either polymers and inorganics or combination of them. Polymers can be further categorized into polar and nonpolar polymers based on their dipole moments (Lovinger et al., 1982). Nonpolar polymers are completely covalent and have symmetric molecules in general. There are no polar dipoles in these materials, and there is no intentional effort to align any dipoles in an applied electric field. However, the electric field shifts the electrons slightly in the direction of the electrical field to establish electron polarization. Individual dipole moments cancel each other out due to symmetry in a nonpolar polymer and are therefore responsible for lower dielectric permittivity. Examples of some nonpolar polymers are polypropylene (PP) and polystyrene (PS), polytetrafluoroethylene (PTFE), low-density polyethylene (LDPE), polyolefins, etc.

The polar polymers do not have a fully covalent bond, and there is a slight imbalance in the electronic charge of the molecule. In polar polymers, dipoles are formed by an imbalance in the distribution of electrons, and the dipoles may attempt to align with the field in the presence of an electric field. In polar polymers, the dipoles typically do not cancel each other. As a result, individual dipole moments become enhanced, and they show relatively higher dielectric permittivity than nonpolar polymers. Examples of polar polymers are polymethyl methacrylate (PMMA), polyvinylidene fluoride (PVDF), polyvinyl chloride (PVC), polyamides. High-k inorganic dielectrics are vital components of the present generation and future energy storage devices. Metal oxides (MOs) are the most common inorganic dielectrics. Some of these include barium titanate ($BaTiO_3$) (Hoshina, 2013), calcium copper titanate ($CaCu_3Ti_4O_{12}$) (Chung et al., 2006), strontium titanate ($SrTiO_3$) (Nisa et al., 2008), tantalum oxide (Ta_2O_5), zirconium oxide (ZrO_2), titanium dioxide (TiO_2), lanthanum oxide (La_2O_3), hafnium oxide (HfO_2) (Karaman et al., 2008). These high-k MOs act as insulators as they have high electric bandgap so that accumulation of charges happens only on the application of an electric field.

Metal oxide-based dielectrics exhibit large dielectric permittivity, along with high stiffness and excellent thermal stability. Due to their low breakdown strength, poor flexibility, and complex processing conditions, their usage in high-energy-density capacitors is mostly hindered. On the other hand, polymer dielectrics have a relatively high electric breakdown strength, low dielectric loss, and offer processing advantages. However, most polymers still fall significantly short of the growing demands for high-energy-density capacitors because of their intrinsic low permittivity values. Therefore, the main challenge is to significantly increase the dielectric permittivity and energy storage density of polymers while sustaining their excellent other physical, mechanical, and thermal properties. New approaches have been explored, such as the use of dielectric composites to realize desirable dielectric performance.

Dielectric polymer composites, composed of the polymer as a matrix and high-k inorganic/ceramic fillers as the reinforcement, utilizes the properties of both synergistically. Fabrication of polymer inorganic dielectric composites consisting of

TiO$_2$ nanoparticles and polystyrene was first introduced by Khastgir et al. (1988). Polymers exhibit high breakdown strength and low dielectric loss, while fillers, especially metal oxides, have a high dielectric permittivity and high energy storage density (Rahimabady et al., 2013a). The combination of both offers high-performance dielectric composites depending on the type and nature of polymer matrices as well as fillers (Luo et al., 2014).

Moreover, from the energy storage point of view, several persistent challenges still have to be answered. The primary challenge is the physical dispersion of the high-k metal oxide particles in polymers. Despite the potential advantages of the dielectric composites, poor solubility/dispersibility of the high-k MOs (fillers) in the polymer matrix remains challenging. It causes undesirable agglomeration at high filler concentrations. It leads to an increase in the gate leakage current and degraded performance of the dielectric film (Yeo et al., 2002). Improvement in the dielectric permittivity of the polymer composites helps to improve the energy density slightly compared to that of the neat polymer at high filler loading. Therefore, it is necessary to determine the optimal volume fraction of high-k MOs in the polymer matrix to achieve high energy density at high electrical breakdown strength, ensuring high voltage operation of capacitors fabricated from the films of the composite materials. Also, a proper selection of high-k MOs and the dispersion techniques in polymers and their interaction at the microscopic level are essential to obtain high-performance dielectric composite films.

In the present work, the low-temperature method for the fabrication of high-k dielectrics and a formulation of metal oxide-based dielectric ink is reported considering the above issues. The dielectric characteristics of the synthesized materials are discussed. Also, the use of anisotropic structures, namely Janus particles and patchy particles, as a functional dielectric and the role of the polymer-inorganic interface in achieving high dielectric properties of composites are investigated through computational modeling and simulations.

CHAPTER 2

LITERATURE REVIEW

2.1. Introduction

Many excellent studies reported the use of dielectrics within the context of energy storage devices. Furthermore, due to the rapid development of new dielectrics and other electronic materials specifically designed for energy storage devices, it is essential to provide a comprehensive and up-to-date overview focusing on the integration of dielectrics with modern functional electronic materials. Figure 2.1 shows the Ragone plot of energy density vs. power density for different energy storage devices (Mccloskey, 2015). It is illustrating that dielectric capacitors are with the highest power density but with the lowest energy density. It also presents the region that has urgent requirements to be filled by electrostatic/dielectric capacitors, i.e., high-power-density along with high energy density, to meet the immediate need for high-rate-charging and high-energy-density devices. In the forthcoming sections, the theory of dielectrics is detailed, including various types of dielectrics, selection of materials, and processing techniques. A brief introduction to the history of capacitors and dielectrics is worth mentioning before discussing materials and processing techniques.
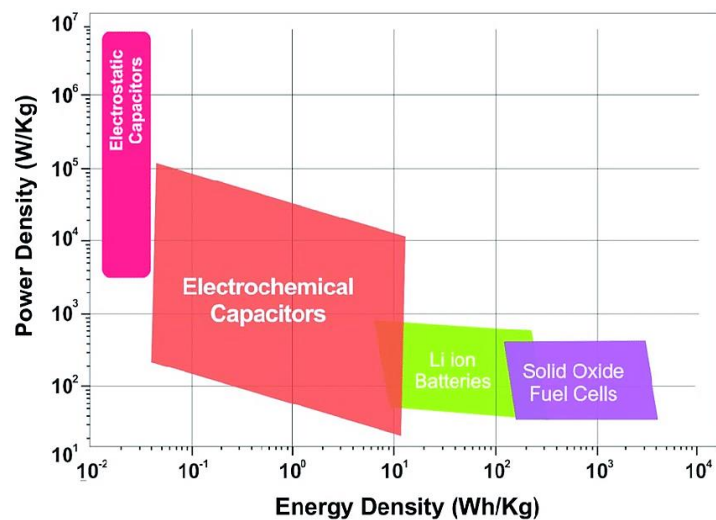
Figure 2.1 Ragone plot of energy density vs. power density of different energy storage devices.

2.2 Thin-film capacitors

A capacitor is an electrical device that can store energy in the electrical field formed between a pair of conductors separated by a dielectric (an insulator). Electrical charges of equal magnitude but opposite polarity build up on each plate when voltage is applied to the capacitor. These are used as energy storage devices in electrical circuits. Capacitors have enabled several important items to be developed in modern life, such as computer processors, television, and cameras' flash systems. The origin of capacitor engineering is attributed to the German Ewald Georg von Kleist (Scholz, 2011). Independently, the Leyden jar was invented in 1746 by Pieter van Musschenbroek, a Dutch physicist at Leyden University (Ho et al., 2010). A hundred years later, a variable capacitor was discovered by Michael Faraday (Brusso and Chaparala, 2014). He achieved this by calculating the varying capacitance of various dielectrics on the capacitors. When the first aluminum capacitor was discovered, about thirty years after Faraday's work, a Farad (F) was named in his honor by the SI unit for measuring capacitance. Since then, different forms of electrical power generation, distribution, transmission, and conversion have been invented. These are based primarily on the use of two types of materials: electrical conducting and wide-energy insulating materials.

In the 19th century, dielectric phenomena became more common and fundamental. Clausius-Mossotti explored the dielectric properties of materials in a systematic way (Felderhof et al., 1983). They aimed to correlate the specific inductive capacity a macroscopic feature of the insulator introduced by Faraday that is now popularly referred to as dielectric permittivity with the material's microscopic structure. Clausius-Mossotti was able to derive a correlation between the real part of the dielectric permittivity ε_r and the volume fraction filled by the conductive particles in the dielectric. Debye discovered at the beginning of the 20th century that certain molecules are correlated with permanent electric dipole moments. This molecular dipole moment

is crucial for the macroscopic dielectric properties of such materials (Debye, 1922). Debye succeeded in expanding the principle of Clausius-Mossotti to take into consideration the permanent moments of the molecule, which enabled him and others to determine the moment of the molecular dipole from the dielectric permittivity calculation. Throughout the 20th century, energy band gap tuning greatly expanded the energy sources and technologies of materials and devices. In the 21st century, the rising demand for electrical power and electrification has put dielectric materials as a focal point on the world stage. Figure 2.2 illustrates to represent the multitude of interactions between the many and diverse core areas of dielectrics that present challenging opportunities in research, development, and manufacturing to the community of scientists, engineers, and technologists.
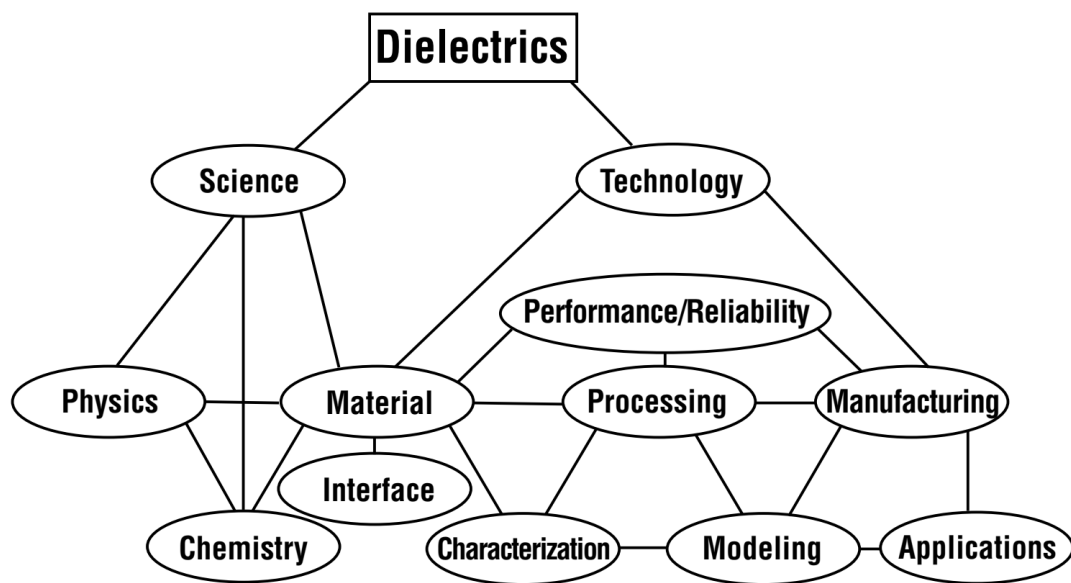
Figure 2.2 Interactions among the core areas of dielectric science and technology

The capacitors need to be small in volume, lightweight, and reliable for many applications like medical devices such as surgical lasers, defibrillators, and X-ray equipment (Thakur and Gupta, 2016). In electronic circuits, thin-film capacitors that offer significant advantages in volume, reliability, uniformity, thickness, and efficiency play a major role. High-performance thin-film capacitors should display low current leakage, low dissipation, and voltage coefficients of capacitance and high breakdown voltage and high capacitance per unit area. In a thin-film capacitor structure, electrode

resistance contributes to the total losses of the capacitor as a series resistance. The typical thin-film capacitor structure with a dielectric layer is shown in Fig. 2.3.
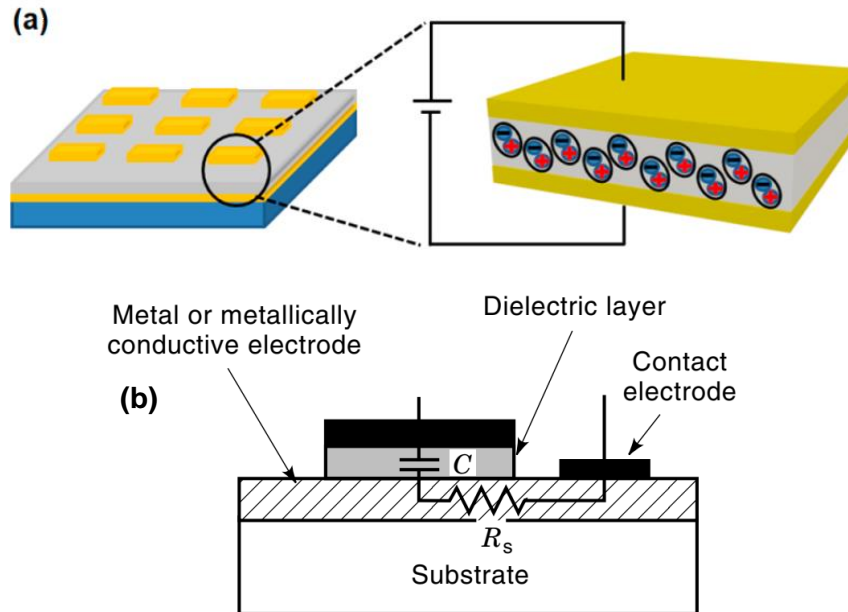
Figure 2.3 (a) Cross-sectional view of a parallel plate thin film capacitor (b) Generic structure of a thin film capacitor.

2.2.1 Capacitance of the thin film

Topologically, the area of capacitance for a thin film capacitor comprised of two parallel electrodes with a common surface area (A), separated by a dielectric film of a thickness (t) with a relative dielectric permittivity (ε_r) is given by

$$C = \frac{\varepsilon_0 \varepsilon_r A}{t} \tag{2.1}$$

where $\varepsilon_0 = 8.8541878 \times 10^{-12}$ F/cm is the permittivity of vacuum. If the dielectric thickness is much lower than the other dimensions of the dielectric, the capacitance contribution from the edges of the dielectric film is neglected (Tyunina and Levoska, 2006).

From Eq. (2.1) two approaches can be used to increase the capacitance value per unit area: (a) to reduce the dielectric thickness and (b) to use a higher dielectric-constant material as a dielectric. Nevertheless, the dielectric cannot be too thin to retain the performance of the capacitor. In other words, for a given dielectric material, there is a

maximum capacity value per unit area achievable. Hence, understanding the theory and mechanism of dielectrics is essential.

2.3 Theory of dielectrics

The dielectric permittivity or relative permittivity of a material determines the electrostatic energy stored for a given voltage in that material per unit volume. Clausius-Mossotti relation (Hannay, 1983) is used to describe the numerical evaluation of a dielectric in an electrical field (Eq. 2.2).

$$P = \frac{\varepsilon_r - 1}{\varepsilon_r + 2} \cdot \frac{M}{\rho} = \frac{N_A \alpha}{3\varepsilon_0} \tag{2.2}$$

P is the molar polarizability, ε_0 is the permittivity in a vacuum, ε_r is the relative permittivity, M is the molecular weight of a repeat unit, α is polarizability, ρ is density, and N_A is the Avogadro constant. This equation demonstrates that the dielectric permittivity depends on the polarizability and the free volume of the elements present in the materials. Polarizability refers to the constant of proportionality under the influence of the electric field for the formation of a dipole. Its value is, therefore, typical of each atom or molecule type. An applied electrical field can polarize a dielectric. When a dielectric is under the influence of the electrical field, electrical charges move from their average position of equilibrium, creating dielectric polarization.

Polarization is defined as the total dipole moments in a dielectric per unit volume (Felderhof et al., 1983). In general, the dielectric cannot polarize instantaneously in response to the applied electric field (E). Thereby, a more general formula of the polarization density (P) as a function of time (t) is

$$P(t) = \varepsilon_0 \int_0^t X_e(t - t') E(t) \, dt' \tag{2.3}$$

where ε_0 is the electric permittivity of vacuum (8.854×10^{-12} Fm^{-1}), and X_e is the electrical susceptibility, it is related to the dielectric permittivity (k) by Eq. 2.4

$$X_e = k - 1 \tag{2.4}$$

Dielectric relaxation, caused by a delay in polarization in a dielectric medium concerning a changing electric field, indicates irreversible energy degradation. Dielectric loss (tan δ) a measure of dielectric relaxation can be defined as,

$$\tan\delta = \frac{k'}{k} \tag{2.5}$$

where k and k′ are the real and imaginary dielectric permittivity, respectively. An interesting class of dielectric materials for thin-film capacitor applications is the one associated with a very low dielectric loss, typically <0.01.

The frequency-dependent behavior of dielectric permittivity (k) and dielectric loss (tan δ) characterizes the amplitude and time scale of fluctuations in charge density across the sample shown in Fig. 2.4. The electron cloud is displaced from the nuclei in the opposite direction to the applied field. As a result, the positive and negative charges are separated, and the molecules act as an electric dipole. There are four types of polarization, and these polarizations (shown in Fig. 2.4) are highly dependent on material types.
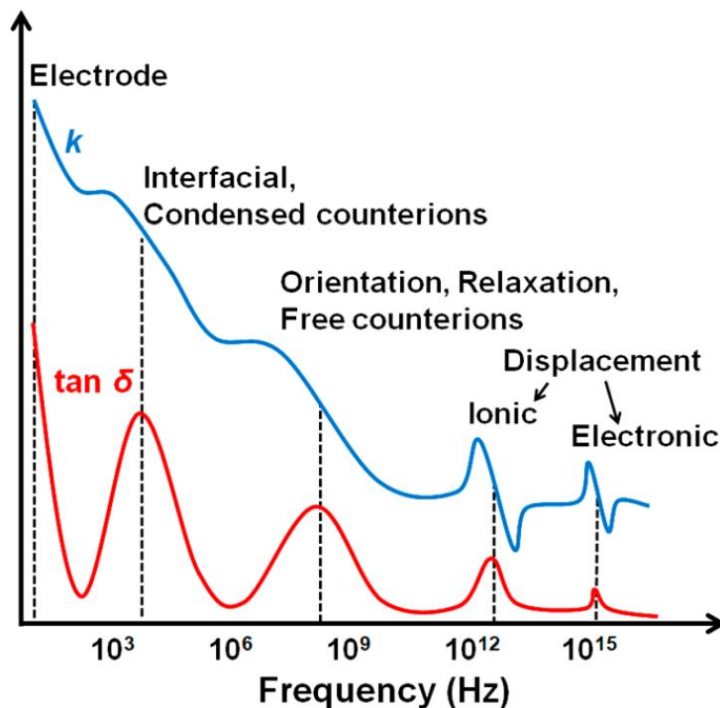
Figure 2.4 Different types of frequency-dependent polarization that are interfacial, orientation, ionic, and electronic polarization. Dielectric permittivity and corresponding losses depicted with blue and red lines, respectively.

Electronic polarization (Fig. 2.5a), operating at frequencies up to 10^{15} Hz, arises in atoms when the negative electronic cloud is distorted by an electric field around the material's positive atomic nuclei in the opposite direction to the field (Bécu et al., 2006). Typically, ionic polarization (Fig. 2.5b) arises in ionic compounds and reacts to field frequencies of up to approximately 10^{12} Hz. The cations and anions become pushed in opposite directions when an external field is applied, resulting in an induced polarization. Orientational polarization (Fig. 2.5c) takes place when there is a permanent dipole moment in the material that rearranges when an electric field is applied. The reorientation of permanent molecular dipole moments and dipolar molecules (Fig. 2.5d) attached to polymers in the direction of the applied field induces polarization. Their relaxation frequencies are at an intermediate-frequency range ($\sim 10^{8}$–10^{10} Hz) (Chernyak, 2006).
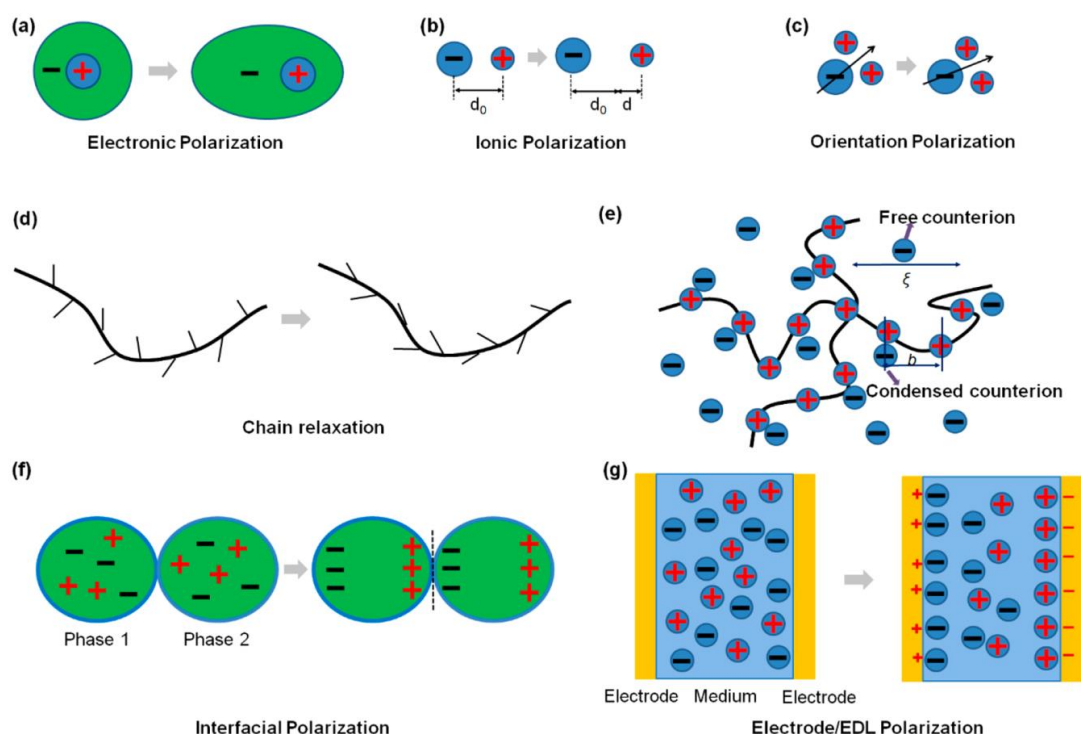
Figure 2.5 Schematic of (a) electronic polarization, (b) ionic polarization, (c) orientation polarization, (d) chain relaxation polarization, (e) free counterion and condensed counterion polarizations in a polyelectrolyte, (f) interfacial polarization, and (g) electrode or EDL (electric double layer) polarization. The monomer size b in panel (e) is the average spacing between charged groups on the polyion chain. ξ is the

correlation length. In all diagrams, the electric field direction is horizontal to the right (Wang et al., 2018).

A dielectric electrolyte comprises of free and condensed counterions in large concentrations (Fig. 2.5e). Free counterions react to the applied field at frequencies in the MHz (10^6 Hz) range and polarize on the length of the correlation scale. Polarization between the interfaces and the electrode/EDL can only contribute to the dielectric response at low frequencies ($<10^3$ Hz). Interfacial polarization (Fig. 2.5f) occurs when a heterogeneous substance composed of more than one phase accumulates charges at the interfaces. This kind of polarization affects both free and bound charges. Due to which, interfacial polarization is generally observed in polycrystalline solids and hybrid systems. About electrode/EDL polarization, all-electric/ionic conducting systems comprise free charges and ions that move towards the electrode interface under the influence of an electric field eventually led to the development of electric/ionic double layers in these regions (Fig. 2.5g). The polarization of the electrodes depends on many factors such as conductivity, structure, composition, temperature, and electrode physicochemical condition, usually the physicochemical parameters that describe the bulk phase (Bordi et al., 2004).

2.4 Classification of dielectric materials

Dielectric materials are classified into inorganic, polymers, and polymer composites/hybrid dielectrics, which have undergone an exciting research and development process in modern history. The advantage of a high dielectric permittivity (k) or permittivity in inorganic dielectrics resulted in high capacitance of thin-film capacitors and miniaturization of multilayer ceramic film capacitor, whereas polymer dielectrics, which offer a high breakdown strength and self-healing feature, that enables reliable operation and higher energy storage stability (Tan, 2019). The perfect dielectric material should possess a wide energy bandgap (E_g) to avoid the leakage current. Too small energy band offset to undesirable high leakage currents due to the thermionic

emission of electrons or holes into the dielectric bands. Figure 2.6 shows the schematic representation of the energy gap offset of an insulator, semiconductor, and conductor.
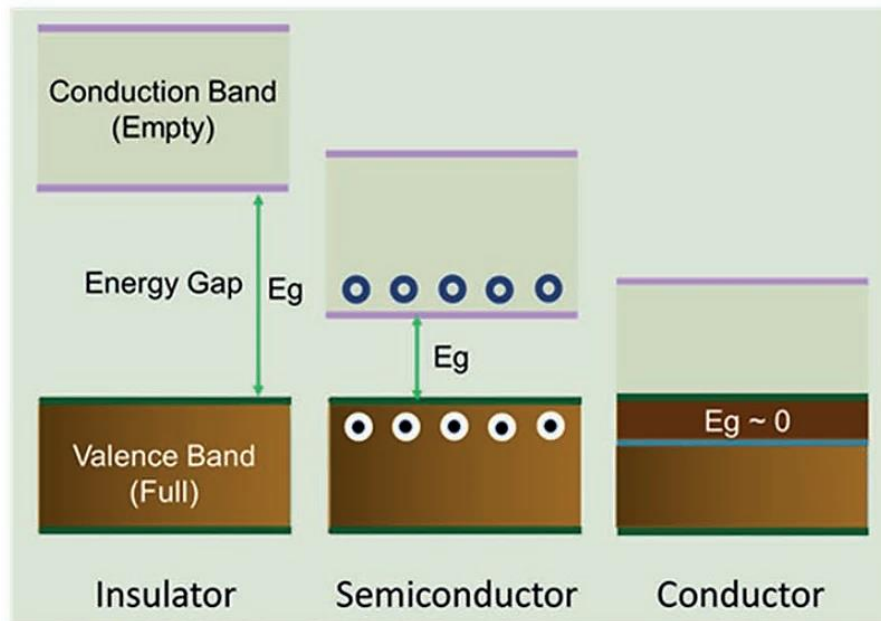
Figure 2.6 Schematic of energy band structure for dielectric/insulating, semiconducting and metal/conducting materials

2.4.1 Inorganic dielectrics

High-k inorganic dielectrics are critical components of the present era and future electronic devices. The focus on new dielectric materials emerged primarily from the need for low-cost device manufacturing processes and the reduction of the operating voltages needed for new flexible printed electronics. One of these needs is to reduce the size of the device, which can also be achieved with high-capacitance dielectrics. In this sense, SiO_2 has attained its scaling limit (Tseng and Ellenbogen, 2001), which directs the research of many groups in quest of alternative high-k dielectrics. Metal oxides (MOs) such as Zirconium oxide (ZrO_2), Hafnium oxide (HfO_2), Lanthanum oxide (La_2O_3), Tantalum pentoxide (Ta_2O_5), Aluminum oxide (Al_2O_3), Yttrium oxide (Y_2O_3), Cerium oxide (CeO_2), Titanium oxide (TiO_2), and perovskites are the most common inorganic dielectrics.
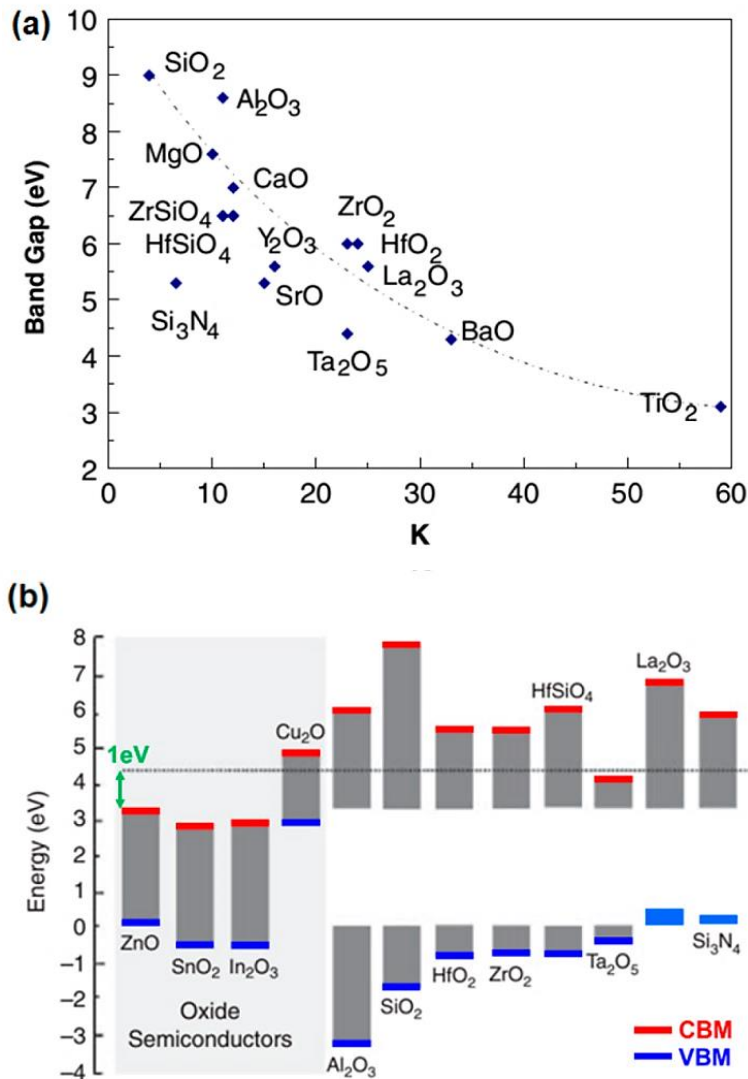
Figure 2.7 (a) Relation between bandgap and dielectric permittivity for metal oxide dielectrics. (b) Calculated band offsets of the dielectrics. The values are normalized to the valence band maximum (VBM) of ZnO. The dotted line indicates the minimum of 1 eV for the conduction band offset (Wang et al., 2018).

The bandgap (E_g) is inversely proportional to the dielectric permittivity in typical inorganic dielectrics (Fig. 2.7a). Hence, dielectric films with a lower E_g should be expected to increase k. However, a large E_g is desirable to suppress charge infusion from the electrodes and decrease charge generation due to thermal/photoexcitation processes. To achieve reliable performance and low leakage current of the energy storage thin films, the band offset of the dielectric valence band and conduction band

should be >1eV. Figure 2.7b shows the energy bands of the calculated conduction band maximum (CBM) and valence band maximum (VBM) offsets of the presented dielectrics.

2.4.1.1 Zirconium oxide (ZrO$_2$)

ZrO$_2$ is an acceptable candidate with real potential to replace conventional SiO$_2$ dielectric in thin-film electronics due to high dielectric permittivity (k~23), large bandgap (~5.8eV), high efficiency, excellent thermal stability in contact with Si substrate (Panda and Tseng, 2013). In general, monoclinic and amorphous ZrO$_2$ films have identical dielectric permittivities (k~23); besides, theoretical calculations indicate that k could be increased to 35-50 for cubic or tetragonal ZrO$_2$ films. The epitaxial growth of ZrO$_2$ films in order to achieve high-k ZrO$_2$ films by stabilizing the tetragonal structure by using selective dc-sputtering reaction at different growth temperatures reported (Zhou et al., 2008). ZrO$_2$ films grown by spin-coating of solution-processed ZrCl$_4$/methoxyethanol and subsequent high-pressure thermal annealing (high-pressure annealing, HPA). It was observed that spin-coated ZrO$_2$ films annealed at 350 °C for 30 min under 10 atm pressure were polycrystalline, smoother, and better insulators than those annealed at 500 °C without HPA. Results of FT-IR, SEM, and spectroscopic ellipsometry demonstrate that the cycle of de-hydroxylation can be improved by using densification-promoting HPA (Kim et al., 2011b).

Synthesis of ZrO$_2$ films by spray combustion on different substrates at temperatures below 350 °C was recently reported (Wang et al., 2016). The precursor formulation contained zirconium oxynitrate (oxidizer) and acetylacetone (fuel) in 2-methoxy ethanol. High-quality, smooth, and amorphous ZrO$_2$ films are obtained by optimizing the oxidizer: fuel ratio, precursor concentration, and substrate temperature. The obtained ZrO$_2$ films (25 nm thick) show a low leakage current density of 1.2×10^{-7} A/cm^2 at 2 MV/cm and high breakdown strength of 9.5 MV/cm. Also, the areal capacitance is 370 nF/cm^2 at 1 kHz (k = 14.3).

2.4.1.2 Hafnium oxide (HfO₂)

HfO_2 is the first and most commonly used gate dielectric substitute for silicon oxide in memory-based electronics. This material is quite inert and shows good tolerance to moisture. It has a dielectric permittivity of k~22 with a bandgap of 5.3-5.7 eV. Until 2007 HfO_2 was not implemented in organic-based devices as a gate dielectric; later in 2007, Tardy et al. introduced sol-gel deposition and anodization for HfO_2 deposition on organic substrates (Tardy et al., 2007).

In order to achieve amorphous HfO_2 films using a sputtering technique, Fortunato's team performed extensive studies and found that Al_2O_3 and SiO_2 were strong co-sputtering options. For instance, 25 °C co-deposited $HfAlO_x$ films are amorphous even after annealing at 500 °C, whereas the 25 °C sputtered 200 nm thick HfO_2 films are nanocrystalline films. Also, the leakage current density at 0.25 MV/cm is significantly lower than 3×10^{-10} A/cm^2 (Pei et al., 2009). Spray pyrolysis was also used in the synthesis of dielectric HfO_2 films. For instance, in a mixture of methanol and ethanol (1:2), a 40 mg/mL $HfCl_4$ solution was sprayed onto a 450 °C SnO_2: Sb-coated glass. They showed that the resulting polycrystalline HfO_2 films have a monoclinic structure and have a wide bandgap (5.7 eV) and a small surface roughness (0.8 nm). Electrical measurements show a high dielectric permittivity (k~18.8), a high breakdown voltage (2.7 MV/cm), and a leakage current density of 5×10^{-7} A/cm^2 at 1 MV/cm (Esro et al., 2015).

2.4.1.3 Lanthanum oxide (La₂O₃)

La_2O_3 exhibits many advantages such as high dielectric permittivity (k~27) with a large bandgap (~6eV), and broad conduction band offset (~2.4eV) with the GaAs substrate. However, it suffers from high moisture absorption and leads to poor device performance. Most of the report suggests that the La_2O_3 shows better dielectric properties when it doped with highly stable high-k oxides such as ZrO_2, HfO_2, Al_2O_3, CeO_2, TiO_2 (Kharton et al., 2000). We considered a few of the La-doped binary oxides as a gate dielectric. Lanthanum zirconium oxide ($La_2Zr_2O_7$) and lanthanum hafnium

oxide $La_2Hf_2O_7$ pyrochlores have a <1% lattice mismatch with silicon that enables them to be grown epitaxially. However, the fluorite-structured phase formed with the pyrochlore phase in epitaxially deposited films. The development of stable fluorite solutions on the crystallization of amorphous powders from precipitation was observed in these systems. The solid solution of the fluorite form in the Hf and Zr systems with La is metastable in the pyrochlore phase shown in Fig 2.8a &b. The phase diagrams are characterized by narrow fields of solid solutions based on monoclinic and tetragonal hafnia and zirconia. The temperatures of all phase transformations in hafnia are higher compared to zirconia-based phases, and larger additions of dopants are needed to stabilize the cubic adjustment. For hafnia-based oxides, oxygen ionic conductivity is significantly lower than in zirconia-based oxides. La_2O_3 solid solubility is less than 1 mol% in monoclinic HfO_2 (Ushakov et al., 2004).
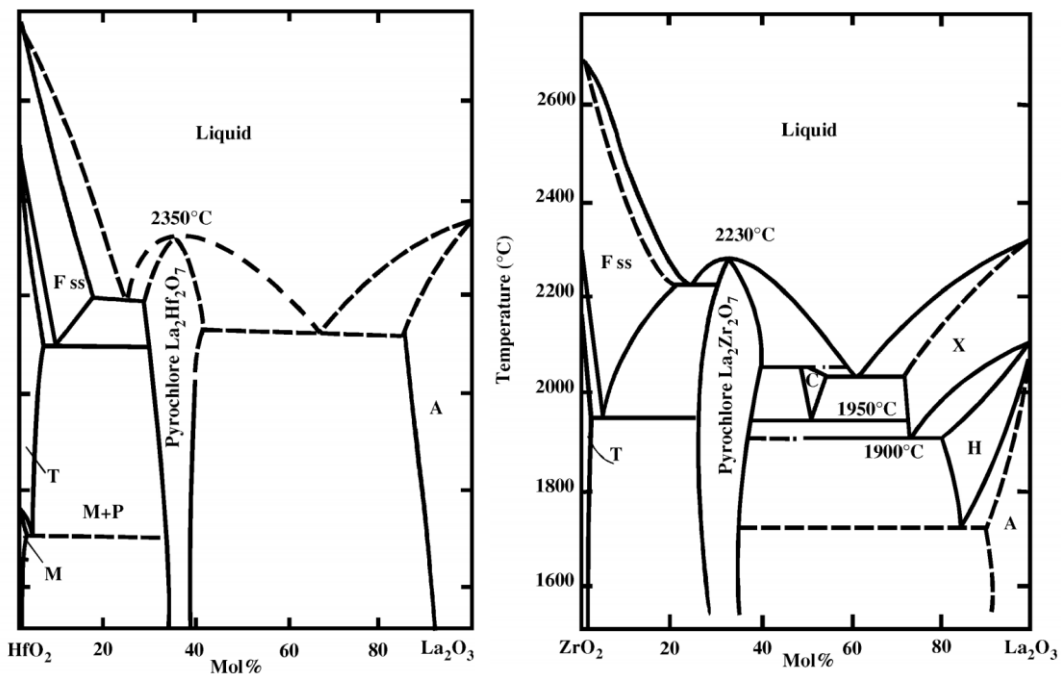
Figure 2.8 Phase diagram of HfO_2–La_2O_3 and ZrO_2–La_2O_3 binary oxide systems show the pyrochlore phase and melting temperatures for $La_2Zr_2O_7$ and $La_2Hf_2O_7$.

Recently, thermal analysis and high-temperature X-ray diffraction (HTXRD) have been used to study the crystallization of precipitated La-doped hafnia and zirconia (doping level 4 to 50%). The crystallization temperature of amorphous hafnium and

zirconium oxides can be significantly increased by alloying with La_2O_3 (Fig. 2.7a &b). The crystallization temperature of $La_2Hf_2O_7$ is higher than 900 °C, making it a perfect choice for advanced dielectrics for the high-temperature devices. Ko et al. recently reported amorphous $Hf-La_2O_3$ films formed by solution-processed spin-coating of a hafnium hydroxide/lanthanum hydroxide precursor solution on Si substrates followed by annealing for one hour at 500 °C (Ko et al., 2014).

2.4.1.4 Titanium oxide (TiO₂)

TiO_2 shows a high dielectric permittivity (k~50-80) and is, therefore, of special interest in the high-k oxide category (Baek et al., 2016). Nevertheless, because of the inherently small bandgap (E_g=3.5 eV), TiO_2 films inevitably suffer from large leakage currents and weak dielectric breakdown fields. Grain boundaries in polycrystalline films are believed to constitute electrical pathways of leakage, resulting in dramatically increased currents of gate leakage. It is advantageous to use TiO_2 as a dielectric because it provides both amorphous films up to 350 °C and can grow epitaxial crystalline film at a higher temperature. Yoon's group reported TiO_2 film growth through the sol-gel process (Yoon et al., 2006). They achieved condensation and film densification using Titanium isopropoxide and methoxy ethanol precursor solution spin-coated and annealed at above ~250 °C (Sung et al., 2015). High leakage current is one of the major disadvantages of TiO_2 dielectric films, which restrict their use in an organic field-effect transistor (OFETs). Several techniques used in inorganic devices to eliminate this leakage current were used to fabricate cryogenic devices use high-k sol-gel derived TiO_2 electron beam resistors. The leakage current is suppressed at liquid helium temperatures, and appropriate FET behaviors are achieved (Khan et al., 2008).

2.4.1.5 Cerium oxide (CeO₂)

CeO_2, with a dielectric permittivity of k~23, has emerged as a successful dielectric layer candidate in inorganic electronics. In its simple stoichiometric form in the fluorite structure, CeO_2 has a stable structure over a wide range of temperatures,

and the composition remains unchanged. Also, CeO_2 has considered a potential gate dielectric material for next-generation technologies in metal-oxide-semiconductor and storage devices (Tarnuzzer et al., 2005). Because CeO_2 has a high oxygen storage capacity, making CeO_2 one of the most crucial exhaust catalysts in the automotive industry. Though, due to the polycrystalline nature, the possibility of leakage is high, which leads to poor device performance. Grain boundaries are typically seen as effective leakage pathways in polycrystalline structures resulting in permanent deterioration of OFETs. Nonetheless, additional treatments (i.e., surface modification with organic groups) are needed to achieve low leakage currents and appropriate growth grain. Several researchers also investigated the suitability of CeO_2-SiO_2 composite films as a possible solution. However, the capacitance is lower, and these films are both amorphous and denser and smoother than pure CeO_2 films (Kim et al., 2007b).

2.4.1.6 Aluminum oxide (Al_2O_3)

Al_2O_3 is the most widely practiced dielectric oxide material (k~8). Atomic layer deposition (ALD) can produce high-quality Al_2O_3 films using a range of organometallic precursors in relatively short cycle times (Groner et al., 2002). ALD films produced on several substrates, including different metals (Au, Co, Cu, Mo, etc.), using $Al(CH_3)_3$ (trimethylaluminum), zinc oxide (ZnO) and water as reactants. Optimal dielectric Al_2O_3 films (almost 12 nm thick) are grown at a temperature of 350 °C and show a leakage current density of approximately 10^{-9} A cm^{-2} at 2 MV cm^{-1}, and dielectric permittivity (k~7). The same team subsequently lowered the growth temperature of Al_2O_3 to 33 °C using a viscous-flow reactor and specifically adjusting the purge cycle. Amorphous Al_2O_3 thin film combustion synthesized by spin-coating an aluminum nitrate and urea water-based precursor solution. In combustion synthesis, the reaction between a fuel (urea) and an oxidizer (metal nitrate) after deposition of the metal oxide (MO) film precursor generates localized and exothermic chemical transformations, facilitating rapid M-O-M lattice condensation and film densification at much lower temperatures than conventional sol−gel processes (Liu et al., 2015). However, due to the relatively low dielectric permittivity of Al_2O_3 (k=8) compared to most other oxide systems,

researchers are focused on the development of composite/stack layers of materials with even higher k values.

2.4.1.7 Perovskites

Recent developments in energy storage systems are associated with high energy storage density, low leakage, and strong temperature stability. Crystalline perovskites possess extremely high dielectric permittivities (>1000) due to space polarization within the crystal lattice (Shen et al., 2010). Nevertheless, amorphous are much more suitable candidates for thin-film transistor (TFT) applications despite lower k values (10−50). Barium titanate ($BaTiO_3$) ceramics is the first ferroelectric perovskite discovered in 1941(Randall et al., 2004). Apart from $BaTiO_3$, strontium titanate ($SrTiO_3$), lead titanate ($PbTiO_3$), calcium titanate ($CaTiO_3$) ceramics are widely used perovskite dielectrics. In 1999, Dimitrakopoulos and his team carried out the first research describing amorphous perovskites as gate dielectrics. They prepared barium strontium titanate (BST) films by sputtering a BST target in an Ar/O_2 gas mixture atmosphere by radio frequency magnetron (Dimitrakopoulos et al., 1999).

Manganese (Mn) doping suppresses the leakage density of sputtered BST films. Due to the increased crystallinity and formation of the perovskite phase, the dielectric permittivity of 3 mol% Mn-doped BST films rises from 24 to 260 as-deposited at 600 °C. Surprisingly, there is no significant rise in leakage current for 3% Mn-doped BST films (Kang et al., 2008). Using spin-coating a titanium isopropoxide and barium acetate 2-methoxyphenyl solution, Wang and co-workers prepared solution-processed $BaTiO_3$ (BT) gate dielectrics and then thermal annealing at 180 °C for 10 min. The resulting 250 nm thick BT films obtained through multiple coating/annealing phases had a dielectric permittivity of 250 with a surface roughness of 0.8 nm (Wang et al., 2013).

However, perovskite dielectrics have much smaller dielectric strength than polymers. Therefore, they could not make significant use of their higher polarizability to store more energy in the material.

2.4.2 Polymer dielectrics

Polymer-based dielectrics exhibit many complementary properties compared to conventional inorganic materials such as being lightweight and low-temperature processability and mechanical flexibility. Additionally, many polymers are amorphous or partially crystalline, and their films provide smooth surfaces (Li et al., 2015). Polymers could be classified into polar and nonpolar polymers based primarily on their mean dipole moments. Individual dipole moments cancel each other due to symmetry in a nonpolar polymer and are therefore responsible for a lower dielectric permittivity.

In polar polymers, however, the dipoles typically do not cancel each other, resulting in individual dipole moments being strengthened and exhibiting a relatively higher dielectric permittivity than nonpolar polymers. The polar nature of polymers relies on both the existence of polar groups and the chain's geometry. The polarity originates because of the difference in electronegativity between the elements of a bond. The more electronegative elements pull the electron cloud to its side, resulting in partial negative charge at the benefit of the other element, which takes on a partially positive charge.

For example, in all-trans β-PVDF, dipoles are in one direction among different forms of poly(vinylidene fluoride) (PVDF), giving rise to polar nature. In particular, due to higher breakdown strengths and dielectric permittivity of as much as k=10, PVDF has a greater energy density, especially in comparison to other polymers such as polyimides, poly(arylene ether nitrile). Examples of some dielectric polar polymers are PVA, PMMA, PVDF based copolymers (Chu et al., 2006). Table 2.1 summarizes the commercially used polymer dielectrics with different dielectric properties.

2.4.2.1 Bi-axially oriented polypropylene (BOPP)

Bi-axially oriented polypropylene (BOPP) is the most important polymer film used in commercial capacitors. The advantageous properties of BOPP are derived from the structure of the polymers chain, which includes no polar groups. In capacitor applications, BOPP has the highest breakdown strength among standard polymer films

shown in Table 2.1. BOPP even has a low dielectric loss and outstanding self-healing capabilities, allowing high-electric field operations. On the other side, at room temperature, BOPP has relatively low permittivity, resulting in a low energy density of 1.2 J/cm^3 (Rabuffi and Picci, 2002). Much research has been done to improve the dielectric properties of PP film by blending with ferroelectric polymers and copolymers.

Table 2.1: Summary of various polymer dielectrics and their dielectric properties

Polymers	Dielectric permittivity at 1 kHz	Loss tangent at 1 kHz	Breakdown strength (kV/cm)	References
Polystyrene (PS)	2.4-2.7	0.008	2000	(Khastgir et al., 1988)
Poly methyl methacrylate (PMMA)	4.5	0.05	2500	(Bergman et al., 1998)
Polyvinyl alcohol (PVA)	12	0.3	1000	(Bettinger and Bao, 2010)
Poly vinylidene fluoride (PVDF)	10	0.04	1500-5000	(Ameduri, 2009)
Polyetheretherketone (PEEK)	4	0.009	450	(Zhao and Liu, 2010)
Low density polyethylene (LDPE)	2.3	0.003	308	(Arbatti et al., 2007)
Poly ethylene terephthalate (PET)	3.6	0.01	2750-3000	(Zhao and Liu, 2010)
Biaxially oriented polypropylene (BOPP)	2.2	0.0002	7500	(Rabuffi and Picci, 2002)
Polycarbonate (PC)	3	0.00015	2520	(Pötschke et al., 2003)
Polyurethane (PU)	4.6	0.02	200	(Li et al., 2015)

2.4.2.2 Polyvinyl alcohol (PVA)

Poly(vinyl alcohol) (PVA) is a water-soluble polymer that can be processed at low temperatures suitable with flexible substrates and shows excellent resistance with most organic solvents. Pristine PVA films have k values between 5 and 8 at $10-10^6$ Hz as obtained by impedance spectroscopy. However, thick PVA films (>1 μm) are essential to ensure low leakage current. Chemical cross-linking is a common strategy to enhance the dielectric strength of polymers. PVA films are photo-cross-linked with ammonium dichromate (AD) as a cross-linking agent (Bettinger and Bao, 2010). After that, a relatively thick dielectric PVA film (1.3 μm) deposited by spin-coating has been used to planarize the substrates of biodegradable poly(L-lactide-co-glycolide) (PLGA) and to ensure low gate-leakage. Even though the capacitance is small (4.56 nF cm^{-2} with a k=6.7), the surface roughness of the cross-linked PVA films on the PLGA substrate is only 0.24 nm, which allows proper film morphology for evaporated small molecule semiconductors. Recent work explored how cross-linkers influence the dielectric properties of PVA films (Benvenho et al., 2013). Thereby, the spin-coated PVA films have been cross-linked for 10 min by UV irradiation followed by annealing in a vacuum oven at 60 °C overnight. The films reveal smooth surfaces with a roughness of 0.25 nm.

2.4.2.3 Polymethyl methacrylate (PMMA)

Polymethyl methacrylate (PMMA), an exceptional transparent (refractive index, n=1.49) thermoplastic polymer with dielectric permittivity of k=4.5, is widely used in many industrial and scientific applications. It also posses a better chemical resistance and mechanical flexibility. For transparent electronic devices, PMMA is combined with other inorganic components, primarily silicon oxide, to make hybrid composite materials with sharp optical clarity, lower weight, physical stability, and ease of processability. Jang's group developed a pentacene thin-film transistor utilizing PMMA as a dielectric gate, demonstrating that PMMA transistors had more exceptional electrical properties than SiO$_2$ transistors (Jang et al., 2015). Kang's group used pentacene as an organic semiconductor and ITO as the gate electrode to compare

polymethylmethacrylate (PMMA) with PVP gate dielectrics. They found better FET output in PMMA-based devices, with field-effect flexibility of (0.045 $cm^2 V^{-1} s^{-1}$ and -27.5 V), whereas superior insulating properties were obtained for PMMA than PVP. The improved flexibility of PMMA was due to smaller grain sizes, which resulted in a more compact distribution of pi-electron orbitals (Kang et al., 2005).

2.4.2.4 Polyvinylidene fluoride (PVDF) and its copolymers

One of the most typically used dielectric materials for high-energy capacitors is PVDF based polymers. These are among the highest dielectric permittivity materials in the polymers category and exhibit strong breakdown strength. PVDF was first synthesized in the year 1940, and in the 1970s, ferroelectric behavior was discovered (Gerhard-Multhaupt, 1987). Using IR spectroscopy, Naegele, and Yoon examined both the direction of molecular dipoles and ferroelectric behavior. IR absorptions at 512 & 446 cm^{-1} were correlated with moments of transition along and perpendicular to the dipole of CF_2 (Naegele and Yoon, 1978). Kepler and Anderson noticed that the axes of PVDF crystalline regions were oriented towards the applied electrical field, based on the X-ray diffraction (XRD) of the sample before and after poling (Kepler and Anderson, 1978).

Several PVDF-based copolymers have been widely used to alter the electrical properties of dielectric composites. These are poly(vinylidene fluoride-co-hexafluoropropylene) P(VDF−HFP), poly(vinylidene fluoride-co-trifluoro ethylene) P(VDF−TrFE), poly(vinylidene fluoride-co-chloride trifluoride ethylene) P(VDF−CTFE). PVDF-HFP is formed by introducing a hexafluoropropylene (HFP) group in the matrix of PVDF. A variety of interesting properties arise from different HFP content in P(VDF−HFP). Low HFP content (~5-15 mol% HFP) is referred to as flexible PVDF, which is thermoplastic and semi-crystalline, whereas higher content (>19-20 mol%) renders it amorphous and elastomeric property. Nonetheless, 22 mol% HFP provides the best choice between low glass transition temperature and completely amorphous polymer (Ameduri, 2009). P(VDF−HFP) has a relatively lower crystallinity than that of PVDF due to the existence of large CF_3 groups. The ferroelectric

characteristics of P(VDF−HFP) polymers are highly reliant on the preparation conditions (Sousa et al., 2014).

So far, two class of dielectrics have been reviewed to fabricate thin-film capacitor (i) use of high-k inorganic materials and (ii) use of easily processable polymer dielectrics. Both deliver some advantages and disadvantages. In particular, while high-k metal oxides are perfect candidates for the film capacitor with high dielectric permittivity, but most of them are required high-temperature annealing methods and shows a high dielectric loss. On the other hand, easily processable polymers usually have a low dielectric loss and less leakage current. However, they suffer from low dielectric permittivity with low operating temperatures. In the following section, the utilization of both inorganic and polymer dielectric in a composite form is discussed.

2.4.3 Polymer nanocomposite dielectrics

Polymer nanocomposite materials have relatively high electric breakdown strength compared to conventional high-k oxides. Most notably, they offer many processing benefits, including mechanical flexibility and the ability to be formed into various shapes to power electronic devices with reduced weight to volume ratio. Combining low-k polymers with high-k metal oxides is proved to be an effective technique for increasing dielectric permittivity of the nanocomposites (Arbatti et al., 2007).

The composite strategy focuses on the idea that a high energy storage capacity can result from the high permittivity of high-k oxides and excellent dielectric strength of polymers. In order to maintain the energy (W) stored in a capacitor constantly with a provided dielectric material, it is necessary to reduce the thickness (d) of the dielectric film to counteract the reduction in the volume of the capacitor (Δv) which can be represented by the Eq. 2.6.

$$W = \frac{1}{2}CV^2 = \frac{1}{2}\varepsilon_0\varepsilon_r V^2 \left(\frac{\Delta v}{d^2}\right) \tag{2.6}$$

where C is the capacitance of the parallel plate capacitor with an applied voltage V.

The only way to prevent the conflict mentioned above is to replace the microparticles with nanometer-sized fillers to prepare dielectric nanocomposite. The benefits of nanocomposite dielectrics involve low filler loading, nanometer sizes, and high internal surface areas. The low nanofiller loads permit the formation of a composite structure without losing some of the intrinsic polymeric properties, including density, flexibility, and easy processing. The following sections summarize the recent progress in the design of dielectric composite/polymer nanocomposites, their dielectric properties, polymer-nanofiller interactions, and theoretical models to predict the dielectric permittivity of the nanocomposite.

Many research groups have dedicated themselves to developing dielectric materials that offer excellent electrical performance and mechanical flexibility and incur low fabrication costs. Polymer matrix embedded with high-k dielectric nanoparticles (NP) have been considered as promising insulating materials with an improved dielectric property for energy storage devices. The constituent NP composition, the concentration of NP in the matrix, and surface modification of NPs are crucial control parameters to enhance the permittivity of well-known insulating polymers, such as PS, PMMA, and polyvinylidene fluoride copolymers. One of the first studies investigating insulators of polymer-nanoparticles emerged in 1988 based on PS-TiO_2 nanoparticles as a composite dielectric material (Khastgir et al., 1988). However, this first attempt ended in an inhomogeneous system in the composite material with porosity issues.

A polymer-ceramic composite using a P(VDF-TrFE) as the polymer matrix and $Pb(Mg_xNb_y)O_3$-$PbTiO_3$ as the ceramic filler reported by Bai et al. They found that the dielectric permittivity increased with the weight fraction of ceramic filler. At higher filler loading, filler tends to agglomerate, and dielectric composite shows a high dielectric loss (Bai et al., 2000). Marks group (2007) reported a method for disrupting agglomeration of the nanoparticles by in-situ polymerization utilizing metallocene catalysts supported by ferroelectric oxide nanoparticles. By coating the nanoparticles with methylalumoxane (MAO), accompanied by in-situ propylene polymerization,

BaTiO$_3$ and TiO$_2$ nanoparticles were homogeneously dispersed within a processable, high-strength polypropylene matrix (Guo et al., 2007).

Researchers also attempted to improve the dispersion stability of TiO$_2$ nanoparticles in PVP with added surfactants. The surfactant, as anticipated, helps TiO$_2$ dispersion in the polymer matrix; however, there was still some aggregation which increased leakage currents and degraded the efficiency of the device compared to the pure polymer (Lee et al., 2007). Another technique to reduce the leakage current by dispersing high-k TiO$_2$ nanoparticles in a Nylon-6 polymer matrix using a solution-based process was reported (Kim et al., 2007a).

To enhance the dispersion of nanoparticles in different polymers by treating Al$_2$O$_3$ particles with a trimethoxy silane and then dispersed in a PVP matrix. The electrical and mechanical stability, as well as the surface roughness, have been substantially improved in these functional nanocomposite dielectrics. Specifically, the dielectric permittivity increases linearly from 4.9 for pure PVP to 7.2 for a nanocomposite with 24 vol% Al$_2$O$_3$ (Noh et al., 2008). The size effect of filler on the dielectric properties of BaTiO$_3$/PVDF nanocomposites was examined (Mao et al., 2010). The dielectric permittivity increased from 52 to 95 at 60 vol%. A transition from cubic to the tetragonal phase of BaTiO$_3$ was correlated to the rise in dielectric permittivity. It is well established that the tetragonal phase of BaTiO$_3$ exhibits comparatively higher dielectric permittivity than the cubic phase due to the non-symmetry of the tetragonal form. Therefore, the polymer nanocomposites dielectric permittivity was indeed improved.

2.4.4 Effect of interfaces in the polymer nanocomposites

The incorporation of various types of nanoparticles, varying from non-conducting to conducting nanomaterials, directly affects the ultimate properties of the resulting dielectric nanocomposites. A variety of parameters, such as polymer chain mobility, crystallinity, and Coulombic potential, have been reported to govern nanoparticles' interaction with polymer matrices (Ho and Greenbaum, 2018).

In order to understand the effect of interface on the dielectric behavior of polymer nanocomposites, two specific models are hypothesized, namely Lewis's model and Tanaka's model.

2.4.4.1 Lewis's model

The inclusion of nanofillers to the polymer matrix results in the formation of multiple nanometric interfaces. The surface of at least part of the nanofillers can eventually be charged based on the difference in Fermi levels and the chemical potential of the nanoparticles and the polymer matrix (Lewis et al., 1996). The polymer matrix, in turn, reacts by creating counter-charges near the surface of the nanofillers. Consider the presence of a positively charged particle inside the polymer matrix, as shown in Fig 2.9a. Here, the surface of the nanoparticle is shown to be planar for simplicity.
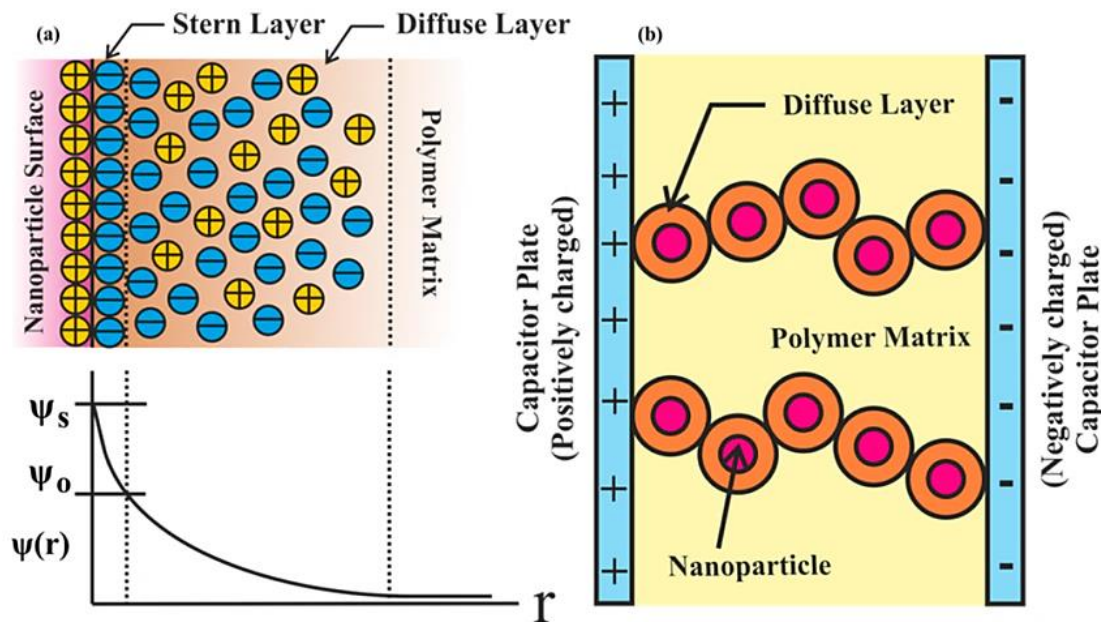
Figure 2.9 (a) Diffuse electrical double layer formed by a positively charged particle in a polymer matrix comprising mobile ions, with the resulting electrical potential distribution $\psi(r)$. (b) Conduction via diffuse double layers in a polymer nanocomposite system.

The charged nanoparticle allows the reallocation of charges in the matrix due to the Coulomb attraction, which leads to the formation of an electrical double layer comprising of a Stern layer and a Gouy-Chapman diffused layer. The Stern or Helmholtz double layer is developed on the surface of the nanoparticle due to the adsorption of the counterions. The diffuse layer is created around the Stern layer by the distribution of positive and negative ions.

The capacitance model was developed by Gouy and Chapman and Stern and Geary (1924). They proposed the existence of a diffuse layer in the electrolyte owing to the accumulation of ions on the electrode surface shown in Fig 2.9b. This layer decides the dielectric properties of polymer nanocomposites and becomes more prominent near the filler percolation threshold.

2.4.4.2 Tanaka's model

Diameter of nanoparticle: 20 to 50 nm
Thickness of layers: 10 to 30 nm
Inter-particle distance in polymer matrix
(Surface to surface): 40 to 100 nm
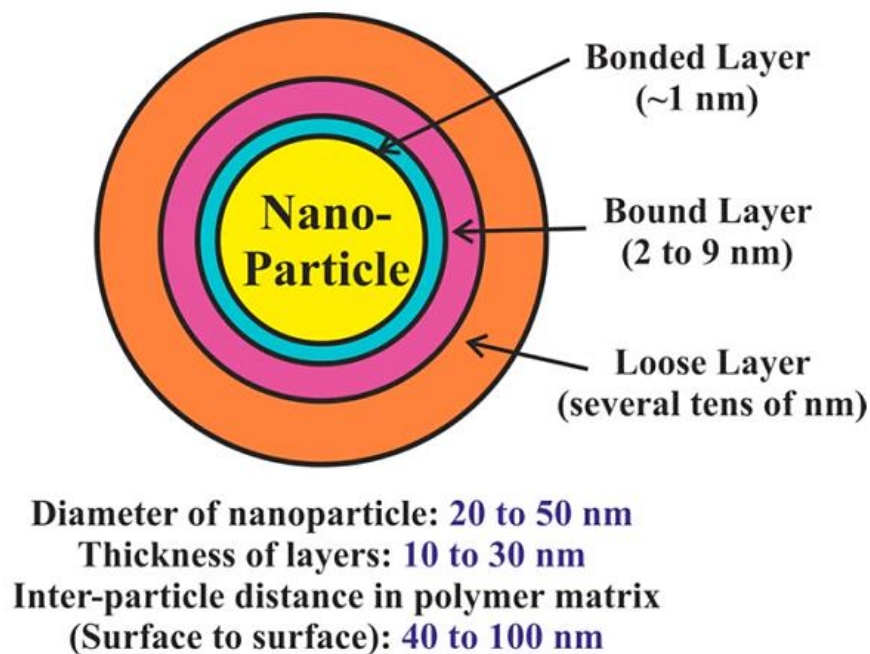
Figure 2.10 Tanaka's theoretical multicore model for polymer-nanoparticle interfaces.

With the addition of spherical nanoparticles in the polymer matrix, Tanaka et al. proposed a theoretical model for the formation of interfaces either by physical,

chemical or electrical means (Tanaka et al., 2005). The interface of nanoparticles is assumed to consist of three layers: bonded layers, bound layers, and loose layers, as shown in Fig. 2.10. The first layer or bonded layer refers to the transition layer with a thickness of 1 nm and is strongly bonded to both organic and inorganic layers. Strong bonding is associated with either hydrogen bonds, or ion or covalent bonds or van der Waals force.

In the interfacial region, the polymer chains are firmly bound and interact with the bonded layer and perhaps even the surface of the inorganic particles. Though its thickness is between 2-9 nm, it is strongly dependent on the interaction between the polymer and nanoparticles. The loose layer is coupled to the bound layer with a thickness of several tens of nm. In this region, the polymer matrix has different chain conformation, crystallinity, mobility, free volume than the bulk polymer matrix. Tanaka's model explores the different ways in which the dielectric properties of polymer nanocomposites can be tailored. The dipole orientation of the polar radicals in the bound layer is adversely affected. The loose layer, on the other hand, reduces the free volume. Both effects lead to a decrease in dielectric permittivity. The choice of an effective coupling agent is, therefore, an essential factor in achieving a high energy density.

2.4.5 Theoretical models to predict the dielectric permittivity of the polymer nanocomposite

The effective dielectric permittivity of a polymer nanocomposite depends on the dielectric permittivities of the fillers and the polymer matrix, along with the different fillers loading and interactions between them. Different models have been developed to determine the effective dielectric permittivity of nanocomposites. Such models are developed based on certain assumptions, which in turn provide insight into the different properties of polymer nanocomposites.

2.4.5.1 Lichtenker's Model

It is a logarithmic combination equation and is most effective in measuring the polymer nanocomposite's effective permittivity. Equation 2.7 describes Lichtenker's formula (Feng et al., 2018a).

$$\varepsilon_{\text{eff}} = \varphi_f \varepsilon_f^{\alpha} + \varphi_p \varepsilon_p^{\alpha} \tag{2.7}$$

where ε_{eff} is the effective dielectric permittivity of the nanocomposites, $\varepsilon_{p,}$ and ε_f are the dielectric permittivity of the polymer matrix and insulating filler, respectively. φ_f and φ_p are the volume fractions of fillers and polymer, respectively. Here, α varies from -1 to 1. Thus, the equation sets the upper and lower limits of the dielectric permittivity of the mixture.

2.4.5.2 Maxwell−Garnett Model

Because of its linearity, the Maxwell-Garnett method is relatively simpler to model. However, this model can be applied at low nanofiller loadings, i.e., below their percolation limit (Skryabin et al., 1997). The model assumes that the inter-filler distance of randomly oriented fillers is larger than their standard sizes. Moreover, the resistivity of the matrix or filler in nanocomposites is not constrained. The theoretical effective dielectric permittivity (ε_{eff}) of nanocomposites filled with nanoparticles is given in Eq. 2.8.

$$\varepsilon_{\text{eff}} = \varepsilon_p \left[1 + \frac{3\varphi_f(\varepsilon_f - \varepsilon_p)}{\varphi_m(\varepsilon_f - \varepsilon_p) + 3\varepsilon_p} \right] \tag{2.8}$$

where φ is, the volume fraction and its subscripts f and p indicate filler and polymer matrix, respectively. Apart from the well-known models discussed above, there are various other models valid under particular conditions. The applicability of different models depends on the nature of fillers as well as the polymer matrix.

Now, the next section will cover solution-based processes for the fabrication of dielectrics that can be utilized in the energy storage devices.

2.5 Solution processed high-k dielectric films

High-k oxides films are being produced using conventional costly vacuum-based methods, such as physical vapor deposition (PVD), chemical vapor deposition (CVD) (Mehandru et al., 2003), atomic layer deposition (ALD) (Youm et al., 2003), and Electron beam evaporation (Triyoso et al., 2007). These methods demand long processing times in high-vacuum environments for perfect film deposition. Typically for film densification, post-deposition treatment at relatively high temperatures is also necessary. In this context, the solution-processable dielectrics are more advantageous for fabricating electronic devices because they are cost-effective and can be processed in large volumes. The solution-based process provides a substantial reduction in manufacturing costs by removing vacuum deposition systems and replacing them with printable precursor materials.
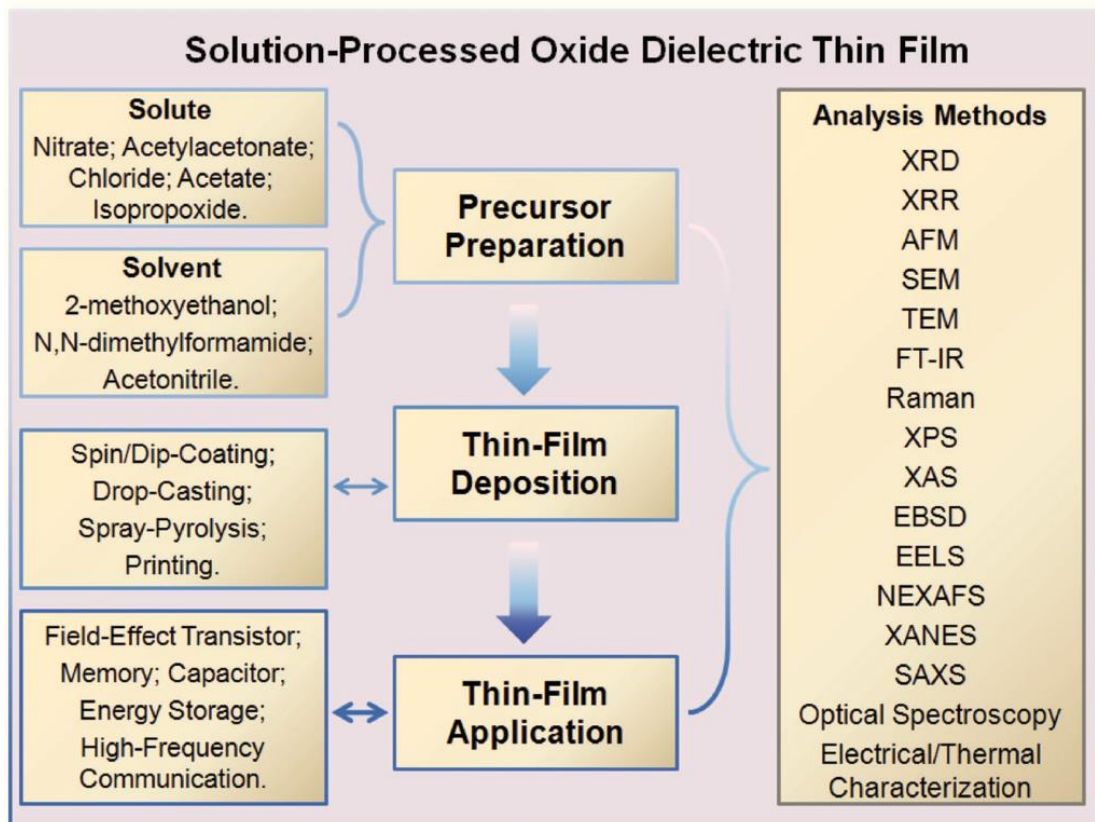
Figure 2.11 Different stages required for the fabrication of solution-processed derived oxide thin films.

There are several ways to make high-k oxide films utilizing solution techniques, such as spin/dip/spray/bar coating, drop-casting, and different printing methods. Each technique has its benefits and drawbacks, including operational ease, precursor preparation, throughput efficiency, and position accuracy (Schneller et al., 2013). The selection of metal salt and solvent is crucial to achieving structurally dense oxide films at low temperatures. Figure 2.11 shows that commonly used precursor metal salts for oxide film fabrication primarily include chlorides, nitrates, acetates, and acetylacetonate (Pasquarelli et al., 2011).

2.5.1 Spin coating

The spin coating technique has been widely used to fabricate oxide dielectric due to low cost and ease of processing (Norrman et al., 2005). The main advantages include better reproducibility and ease of integration with conventional micro-fabrication techniques. During the spin coating process, drops of a precursor solution are deposited on hydrophilic substrates, which are then accelerated to high angular velocities (hundreds to thousands of rpm) to spin off excess solution, resulting in thin and uniform film (Fig. 2.12a). Solvent evaporation aids solid-like gel film formation for dramatically increased viscosity. The thickness (d) of the resulting gel film is defined primarily by the viscosity (η) of the precursor and the angular speed in rpm (ω), $d = \eta\omega^{-1/2}$. Spin coating simplicity is more suitable for nanoparticle-based solution, sol-gel route, and hybrid-type approaches, providing a quick deposition of oxide thin films (Fig. 2.12b).

However, spin coating is a batch process, somewhat limited in scalability, not suitable for large scale production. Moreover, in most of the case, a precursor solution ($\approx 85\%$) is wasted during the deposition step. Despite the simplicity of the solution-based process, high annealing temperature (>400 °C) is necessary to develop a pinhole-free and dense film, which is a prerequisite for a dielectric to block the capacitor leakage current. Therefore, high-temperature annealing is not acceptable with polymer substrates, which restricts the versatile use of polymer in device applications.

Recently developed chemical approaches and post-treatment methodologies have permitted the investigation of several low-temperature techniques. The carbon-free water-induced (WI) path, chemical combustion (CB) reaction, and UV/plasma activation assisted were identified as promising strategies to fabricate oxide thin films. One approach is solution combustion.
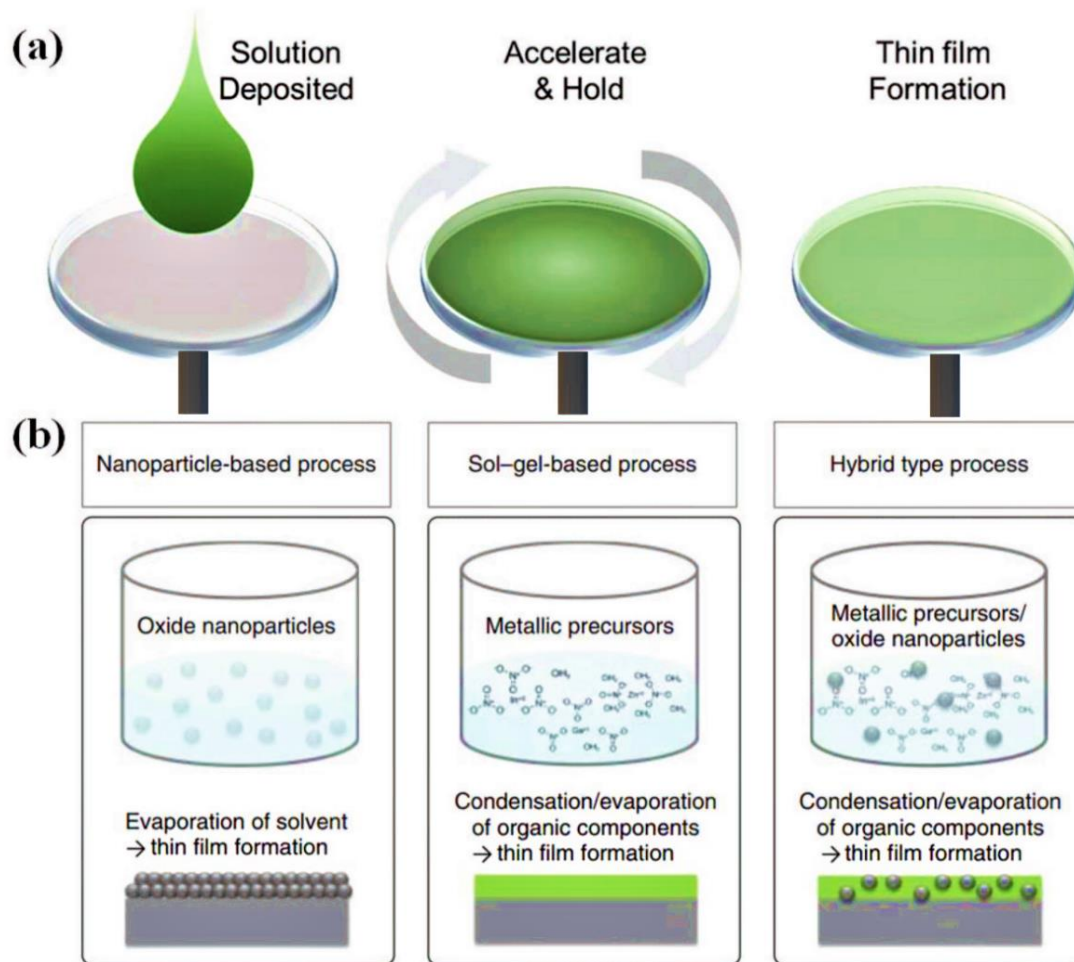
Figure 2.12 a) Spin coating to fabricate thin films b) Various approaches to form oxide thin films by spin coating (Liu et al., 2018).

2.5.2 Solution Combustion

A simple method to reduce processing temperature within the as-deposited films is the exothermic solution combustion method. Solution combustion is one such technique where redox chemistry involving fuel and the oxidizer are utilized. The exothermic reaction between these constituents results in the heat output at low reaction

initiation temperature. The principle of combustion for the fabrication of an oxide thin film transistor was first suggested by the Marks group (Kim et al., 2011a). By using nitrate as an oxidizer and acetylacetone/urea as a fuel, the localized exothermic reaction and induced energy within the gel film facilitate the decomposition of residual impurities and the effective formation of the metal oxide lattice, eliminating the need for high thermal energy (Wang et al., 2016). Another variant in the solution processing is the usage of colloidal solution of nanoparticles of the desired material. The solvent evaporated deposits of colloidal solution results in the formation of the film due to the sintering of nanoparticles under the supplied thermal energy. However, the process has an additional challenge regarding the morphological development of the film. The evaporation of the solvent guides the movement of nanoparticles within the drop; this may lead to an undesired coffee-ring effect (Deegan et al., 1997).

2.6 Sonochemical synthesis of metal oxides

Sonochemistry derives from the extreme transient conditions caused by high-intensity ultrasound, which produce distinctive hot spots capable of reaching temperatures above 5000 K, pressures equaling 1000 atm, and heating and cooling rates exceeding 10^{10} K s^{-1} (Suslick, 1990). Such conditions are distinct from several other conventional synthesis techniques such as photochemistry, wet chemical method, hydrothermal synthesis, or flame pyrolysis. High-energy chemical reactions arise when a substance is irradiated by high-intensity ultrasound. High-intensity ultrasound is responsible for numerous physical and chemical results that are beneficial to nanomaterial preparation or modification. The diverse action mechanisms allow it as a powerful tool applicable to a variety of subjects of current interest, including graphene, polymers, catalysts, metal and metal oxide, crystallization, and anisotropic materials (Xu et al., 2013).

The first effort to utilize ultrasound to increase chemical reaction rates was attempted (Richards and Loomis, 1927). Since then, the use of ultrasound in synthesis has proven to be a considerable technique in various fields of engineering, materials science, and chemistry. A variety of nanostructured materials with regulated morphologies, shapes, and formulations have been effectively prepared by applying

high-intensity ultrasound with specific combinations of reaction conditions and precursor compositions. Sonochemical approaches exhibit positive attributes such as accelerated polymerization, lower reaction temperatures, and a high molecular weight of polymers. Sonochemistry often induces and accelerates chemical reactions that decrease reaction time, increase production rates, and induce reactions that are not achievable using conventional methods. Sonochemical methods dictate a specific way of producing different types of polymer nanocomposites, not only for the dispersion of fillers in the matrix but also for polymerization reactions (Doktycz and Suslick, 1990). The extreme transient conditions developed during the sonochemical reaction result in the creation of specific materials. It also allows synthesis on the benchtop in a room-temperature liquid that might otherwise require high temperatures, high pressures, or long reaction times.

Sonochemistry is widely used for the preparation of nanostructured noble metals when non-volatile precursors are dissolved in reactive solvents (usually water or alcohol). In these situations, sonolysis of the solvent vapor creates strong reducers that have many advantages over conventional reduction techniques: no additional reducing agents are needed, the reduction rate is typically very high, and very small nanoclusters can be generated in this way when suitable stabilizers are available (Xu et al., 2013). A large number of chemical routes, including controlled chemical reduction, solvothermal synthesis, photochemical reduction, and radiolytic reduction, can be used to prepare nanostructured metal oxides. Sonochemical preparation also provides an easy route to the synthesis of metal oxide nanoparticles (Fe_3O_4, CuO, ZnO, TiO_2) (Kumar et al., 2000). A systematic study on the effect of ultrasound on the production of metal oxide nanoparticles suggests that solvent/surfactant properties largely determine particle size: particle size is inversely related to alcohol concentration and alkyl chains (Grieser, 1997).

Sonochemistry can also improve sol-gel synthesis, a versatile strategy for the preparation of nanoscale metal oxides. The use of ultrasound during the sol-gel process can accelerate hydrolysis and produce metal oxides with narrower size distributions, higher surface area, and improved phase purity. For example, TiO_2 (titanium oxide), zinc oxide (ZnO), cerium oxide (CeO_2), vanadium oxide (V_2O_5), and indium oxide

(In$_2$O$_3$) were all prepared by ultrasonic irradiation of their respective precursor solutions (Qian et al., 2003). A range of nanostructured materials with controlled morphologies, structures, and compositions can be prepared by the application of high-intensity ultrasound with specific modifications of reaction conditions and precursor compositions.

Several research articles in the field of dielectric polymer composites published from different countries during 1953-2020.
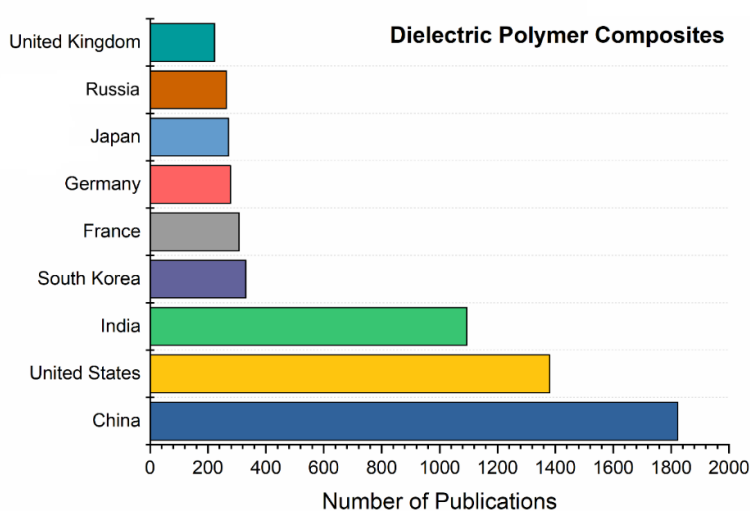
Many research articles published in the area of dielectric polymer composites by university wise from 1953-2020. Scopus data accessed on 20th January 2020.
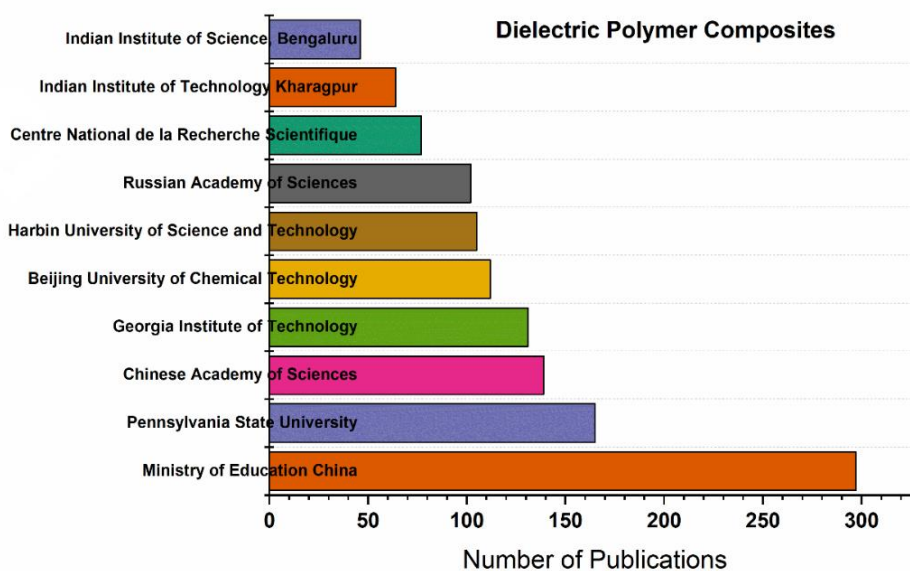
2.7 Challenges for improving energy storage density of the polymer composite dielectrics

Although metal oxides (MOs) provide numerous advantages in the fabrication of high-permittivity polymer composites, the achievement of ultrahigh-energy-density nanocomposites poses several challenges. One of the typical problems is that it needs a very high-volume fraction of MOs (>50 vol%), which induces a critical increase in Young's modulus of composites with the addition of many irregularities such as voids, pores, and other indirect structural defects, resulting in a decreased dielectric breakdown strength of these polymer-based nanocomposites. The agglomeration of the MOs results in lower electrical field-derived electronic conduction and undesirable porosity with excessive dielectric loss and dielectric failure. Surface-modified MOs using a coupling agent, hydroxylation, surfactants, and other organic molecules have been effectively used to address the agglomeration issues. However, these techniques still have several limitations, as the modifiers do not actively participate in enhancing the property. There is an urgent need not only to develop high energy density dielectric composites without agglomeration of MOs but also to control composite morphologies. The new processes must substantially increase the energy storage density of dielectrics to reducing the size, weight, and cost of electronic devices.

The interface between MOs and polymers, one of the most crucial parameters for improving the energy storage density of composites, still requires understanding. There is a need for an approach to understanding the polymer-inorganic interface behavior under the applied electric field to fabricate high-performance dielectric composite films. The following are the key points to be addressed from the literature review, (i) better dispersion of MOs nanoparticles in the polymer matrix to obtain low dielectric loss and high breakdown strength, (ii) low-temperature solution techniques to fabricate high-energy flexible polymer composites, (iii) fabricating dielectric composite in single-stage/or by in-situ formation of MOs in polymer solution via the concept of dielectric ink (v) computational modeling to understand the interface behavior to control the stability of the dielectric characteristics, this being crucial for electronic applications.

2.8 Scope and objectives of the work

2.8.1 Scope

Metal oxide dielectrics were widely utilized in electrostatic capacitors because of their excellent physical and chemical properties. However, its usage is limited by aggressive miniaturization of microelectronic devices and low breakdown strength and high dielectric loss. High leakage current and undesirable power dissipation may have occurred in the extremely thin-film oxide. The thicker dielectric film reduces the overall energy storage density of the capacitors. Thus, a new combination of dielectric material/composites with physically thin but high energy storage density with high dielectric permittivity is needed. Some high dielectric permittivity metal oxides such as HfO_2, ZrO_2, Al_2O_3, La_2O_3, TiO_2, Ta_2O_5, Y_2O_3, and polymers such as PVDF, PMMA, PTFE, and LDPE were reported in the literature (Dang et al., 2013). Lanthanum and zirconium-based and polymer-based dielectrics have been investigated because they have high dielectric permittivity, relatively large bandgap, high breakdown strength, high conduction offset, low interface trap densities, small lattice mismatch with Si, and high both thermal and chemical stability. The combination of metal oxide and polymers offers high-performance dielectric composites depending on the type and nature of polymer matrices and fillers. However, there are more details left to emerge the feasibility of these dielectrics.

Nevertheless, there is still lack of information on the a) low-temperature and straightforward strategies for the fabrication of lanthanum and zirconium-based dielectrics b) formulation of high-k colloidal dielectric ink which can be directly printable on polymer substrate c) utilization of polymer-inorganic patchy particles as functional dielectrics d) interface effect on the dielectric properties e) design of metal oxide-based dielectrics with Janus structures. An intensive study on the research gaps mentioned above is required to fully discover the possibility of metal oxide-based polymer composite dielectrics in thin-film capacitors or other energy storage devices. The following specific objectives are formulated within the scope of the research work.

2.8.2 Objectives

- To synthesize and characterize Lanthanum doped Cerium Oxide nanopowder and Lanthanum Zirconium Oxide dielectric ink using a low-temperature sonochemical approach for thin-film capacitors and to study their dielectric properties.
- To fabricate Lanthanum Zirconium Oxide (LZO) reinforced PMMA nanocomposites for improved energy storage density.
- To formulate composite dielectric ink of PVDF-HFP/LZO and optimize LZO content for desirable dielectric properties of PVDF-HFP/LZO composite films to make thin-film capacitors.
- To design and fabricate PS-Fe_3O_4 patchy microspheres and to understand the dielectric behaviour at the polymer-inorganic interface through computational modeling and simulations.
- To fabricate a new functional Janus structure of La_2O_3-ZrO_2 dumbbell shape and to explore their dielectric responses.

CHAPTER 3

SONOCHEMICAL SYNTHESIS OF LANTHANUM DOPED CERIUM OXIDE NANOPOWDER AND LANTHANUM ZIRCONIUM OXIDE DIELECTRIC INK

3.1 INTRODUCTION

The primary challenges in the field of high-k metal oxides are developing reproducible, easily scalable, and economical processes for the synthesis of stable nanomaterials. Various factors that control the shape, size, and crystallinity of the high-k metal oxides produced include precursor salt, temperature, time, pH, the degree of mixing. The energy needed for the chemical reactions or physical transformations may be supplied directly through thermal and pressure energies or indirectly through microwaves or ultrasonic waves. The commonly employed conventional methods for the synthesis of high-k metal oxides (MOs) are hydrothermal, sol-gel, high-temperature solid-state, molten salt route, spray pyrolysis, and supercritical solvothermal (Bai et al., 2000). However, most of the methods may require high reaction temperatures due to calcination step involved, and few may need high pressures. Hence, there is a need to develop simple, faster methods that can be operated at low temperatures and pressures to produce stable high-k MOs.

The sonochemical method is one of the simple, fast, and energy-efficient ways to synthesize high-k MOs over conventional methods (Pinjari and Pandit, 2011). In the sonochemical method, shock waves and local turbulence are produced due to continuous formation, growth, and implosive collapse of bubbles known as acoustic cavitation in liquids at the microscopic level during the ultrasonic irradiation of liquids. According to hot-spot theory (Doktycz and Suslick, 1990), during the collapse of transient cavitation bubbles, hot spots, i.e., the core of the bubbles with localized hot temperature ($\sim 1000's$ of K) and high pressures ($\sim 100's$ of bars) exist for very short timescales and vanish. Each microbubble acts as a small microreactor which produces

different reactive species and heat during its collapse. Therefore, enhanced mixing, heat, and mass transfer rates can be obtained by coupling ultrasound with the liquids or liquid-solid (slurry) systems. It makes the sonochemical method a viable and attractive technique for synthesizing high-k MOs through wet chemical methods (Kahlaoui et al., 2013). The sonochemical method provides the facile, greener, and an inherently safer way to create supercritical conditions of high temperatures and pressures microscopically in liquids, which cannot be easily achieved by other conventional methods.

The conventional method used to synthesize the lanthanum cerium oxide (LCO) and lanthanum zirconium oxide (LZO) solution comprise a molecular dispersion method and a nanoparticles dispersion method. In the molecular dispersion method, inorganic precursors are initially dispersed into a solvent (dispersant) through hydrolysis and thermal decomposition to obtain the LCO or LZO precursor solution (Woods et al., 2017). The precursor solution is then coated on the substrate with a subsequent thermal treatment under a reducing atmosphere for the formation of thin LCO or LZO films that protects the substrate from oxidation. In the nanoparticle dispersion, nanoparticles of LCO or LZO are synthesized first and then dispersed in solvent through suitable means and stabilization to obtain a precursor solution. This LCO or LZO precursor solution is then coated on the substrates with a thermal treatment to form a thin LZO film. The conventional methods used for synthesizing the LCO and LZO is a tedious process and requires a high temperature that leads to the wrinkled film, production of corrosion and toxic gases, and difficulty in achieving uniform deposition of the precursor solution.

Hence, efficient and straightforward methods to prepare LCO and LZO dielectric materials are required, which can be used directly to manufacture a thin-film capacitor. In this chapter, a simple sonochemical method for the synthesis of La-doped CeO_2 nanopowder and LZO dielectric ink at a relatively low temperature (70 ℃) without calcination is discussed.

3.2 EXPERIMENTAL METHOD

3.2.1. Materials used

Lanthanum Oxide (La$_2$O$_3$, 99.999%), Cerium Oxide (CeO$_2$, 99.999%), ethanol (C$_2$H$_5$OH, 99%) and polyethylene glycol (PEG 8000 kDa), Lanthanum chloride (La(NO$_3$)$_3$, 99.999%), Nitric acid (HNO$_3$, 99.99% trace metal basis) Zirconium acetylacetonates (Zr(C$_5$H$_7$O$_2$)$_4$, >97%) were purchased from Sigma-Aldrich. All the chemicals were analytical grade and used without further purification. Deionized and double distilled water was used throughout the experiment.

3.2.2 Synthesis of lanthanum doped cerium oxide nanopowder

For the preparation of lanthanum doped cerium oxide (La$_2$Ce$_2$O$_7$), 0.0075 mol La$_2$O$_3$ and 0.029 mol CeO$_2$ powders were dissolved separately in 5 ml of concentrated nitric acid using a magnetic stirrer. Both solutions were mixed with 20 ml of distilled water using a homogenizer. A small amount (2 wt%) of polyethylene glycol (PEG) (surfactant) was added to it, and then the solution was subjected to sonication for one hour. A 20 kHz frequency sonicator with a 500 W ultrasonic generator and 13.2 mm diameter probe was used to create acoustic cavitation in the liquid medium. The sonicator was operated in a pulsed mode (ON/OFF ratio of 5s/3s) at a 40% power amplitude. The reaction temperature of the solution was 70 °C. As-synthesized products were centrifuged, washed with ethanol/water mixture, and dried at 80 °C for 8 h in the hot-air oven.

3.2.3 Synthesis of lanthanum zirconium oxide dielectric ink

Lanthanum zirconium oxide (La$_2$Zr$_2$O$_7$) dielectric ink was prepared by the sonochemical approach. 1 g of lanthanum nitrate in a 5 ml concentrated nitric acid to obtain the lanthanum solution. 1 g of zirconium acetylacetonates was dissolved in a mixture of ethanol-water to obtain the zirconium solution. The lanthanum-based solution was added dropwise to the zirconium-based solution to obtain an LZO precursor solution. LZO precursor solution was sonicated at a 40% amplitude of 500 W using a 20 kHz frequency probe sonicator to obtain LZO dielectric ink. Next, LZO dielectric ink was coated on Indium tin oxide (ITO) coated glass substrate by spin

coating and annealed to form a thin transparent LZO film. Here the LZO dielectric ink prepared at low temperature is used directly for the fabrication of the thin-film capacitor. The steps involved in the fabrication of LZO ink and thin-film is are shown in Fig. 3.1.
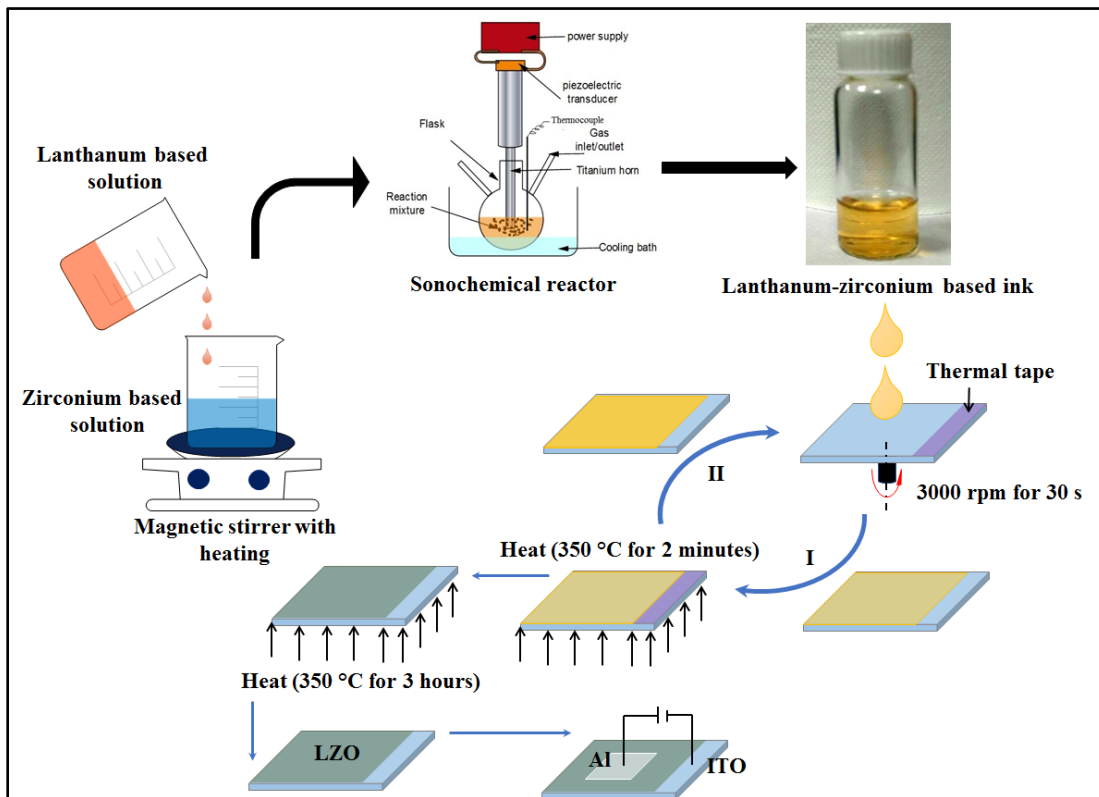
Figure 3.1 Schematic of LZO dielectric ink preparation and thin-film capacitor fabrication.

3.2.4 Characterization

The nanopowders of both undoped and La-doped CeO_2 were characterized by various techniques. The XRD pattern was recorded by Bruker D8 Advance X-ray powder diffractometer using Cu Kα radiation (40 kV, 40 mA) (wavelength λ=1.5406 Å). Raman spectra were collected using Bruker RFS-100/S Raman spectrometer with Fourier transform. A 1064 nm YAG laser was used as the excitation source, and its power was kept at 150 mW. The photoluminescence (PL) characteristics were investigated using the 325 nm line from He-Cd laser excitation. Selected area electron diffraction (SAED) patterns, particle size distribution, and lattice images of the

synthesized nanopowders were obtained using the JEOL 2010F TEM (HR-TEM) capable of operating up to 200 kV. The composition of nanopowder was determined by energy-dispersive X-ray analysis (EDX) attached to JEOL 2010F TEM. The dried nanopowder was pressed uniaxially into disc-shaped pellets of 10 mm diameter with 2 mm thickness using the isostatic pressure of 200 MPa to measure dielectric properties. The pressed samples were sintered at 100 °C for 2 h. Dielectric permittivity and loss were measured at different frequencies in the range of 1 kHz to 1 MHz, using an impedance analyzer (IM3536, Hioki, Japan). The fabricated LZO capacitor is characterized using the Phoenix temperature-dependent IV/CV tool (make: Karl Suss, model: PM8). The characteristics of the capacitor do include capacitance (C) as a function of frequency (F) and capacitance (C) as a function of applied voltage (V).

3.3 RESULTS AND DISCUSSION

3.3.1 Crystallinity, chemical structure, and morphology of La-doped CeO$_2$

3.3.1.1 X-ray diffraction analysis

XRD patterns of the undoped CeO$_2$, La-doped CeO$_2$, and standard stick pattern of pure CeO$_2$ are shown in Fig. 3.2a. The obtained XRD pattern matches well with the standard cubic fluorite phase (Fm-3m225) of CeO$_2$. The diffraction peaks of all samples located at 28.2°, 32.6°, 46.8°, and 55.6° can be well indexed to the (111), (200), (220) and (311) planes (JCPDS File 043-1002). No characteristic peaks of La$_2$O$_3$ were observed. The lattice parameter (constant) of a crystalline powder is a key factor for the confirmation of doping. The true value of the lattice parameter can be obtained by removing the systematic errors of both undoped and doped CeO$_2$ through the construction of Nelson-Riley (NR) plots. NR plots provide a better way to eradicate the systematic errors involved in the measurement of the lattice parameter. The lattice parameter of both undoped and La-doped CeO$_2$ measured in the present experiments is in good agreement with the theoretical values reported by Vanpoucke et al. (Vanpoucke et al., 2014) from the ab-initio density functional theory calculations. By comparing the XRD patterns of undoped and La-doped CeO$_2$, a significant change in peak shift and peak intensity was observed. Lanthanum (La^{3+}) has a higher ionic radius compared to

Cerium (Ce^{4+}). Doping of Lanthanum (La^{3+}) in CeO_2 fluorite structure leads to the expansion of crystal lattice of CeO_2 from 5.41Å to 5.59 Å.
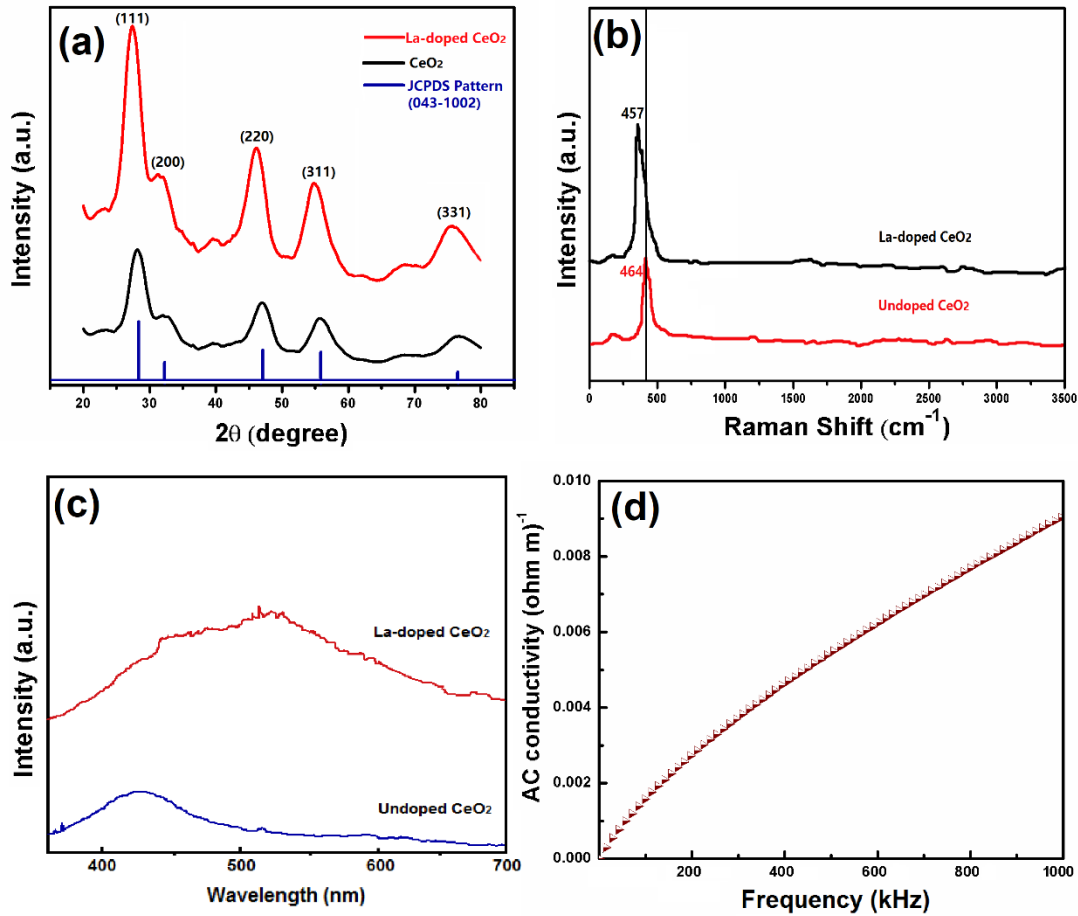
Figure 3.2 (a) XRD spectra with standard stick pattern of CeO_2 (b) Raman spectra (c) Photoluminescence spectra of undoped and La-doped CeO_2 (d) Frequency-dependent AC conductivity of the La-doped CeO_2 measured at room temperature.

Lattice expansion can be attributed to a combination of the effects of the increasing number of oxygen vacancies due to La doping and the larger ionic radius of La^{3+} versus Ce^{4+} (Philip et al., 2006). From Bragg's law of X-ray diffraction and the lattice parameter, we have the relation for the cubic system $\frac{n\lambda}{2\sin\theta} = \frac{a}{\sqrt{h^2+k^2+l^2}}$ (where, n = positive integer, λ = wavelength of the incident wave, (h k l) = Miller indices, a=lattice parameter). The lattice parameter is inversely proportional to diffraction angle θ. A clear shift in all the peaks towards the lower diffraction angle (Fig. 3.2a) was observed

because of lattice expansion in La-doped CeO$_2$, which confirms uniform doping of La in CeO$_2$. By doping Lanthanum in CeO$_2$, the La^{3+} element is introduced to the parent (CeO$_2$) crystal structure, and the mean atomic scattering of parent CeO$_2$ is changed. In XRD, the strength of the atomic scattering from a given element is dependent on its atomic radius. Larger the atomic radius of a dopant, higher will be the atomic scattering and results in increased relative intensity. The higher relative intensity of the XRD peaks was observed in the case of La-doped CeO$_2$ compared to undoped CeO$_2$. It is because of the substitution of Lanthanum (La^{3+}) whose ionic radius is larger than Ce in CeO$_2$.

3.3.1.2 Raman Spectra and photoluminescence emission spectra

Figure 3.2b shows the visible Raman spectra of undoped CeO$_2$ and La-doped CeO$_2$. In the case of undoped CeO$_2$, only one Raman band at 464 cm^{-1} was noted, which corresponds to the F$_{2g}$ Raman band from the space group Fm3m of cubic fluorite structure (Shannon, 1976). The intensity of the Raman band was found to be increased in the case of La-doped CeO$_2$. High-intensity broadband is due to the creation of a large number of oxygen vacancies because of La^{3+} doping in the CeO$_2$ fluorite structure. Further, it was found that the Raman band of La-doped CeO$_2$ shifted towards the lower frequency due to La^{3+} doping (464 cm^{-1} to 457 cm^{-1}). The main reason for this shift might be due to the lattice expansion of CeO$_2$ because of the larger ionic dopant, La^{3+}. The presence of surface-bound water leads to the poor dielectric properties of the material. Raman spectra can also provide the evidence if surface-bound water present in the sample. The broad multimode band around 3200-3450 cm^{-1} is attributed to the O-H stretching of surface-bound water (Pastorczak et al., 2009). However, there was no band in the region of 3200-3450 cm^{-1}, so there is no surface-bound water present in La-doped CeO$_2$.

Photoluminescence (PL) spectra of undoped and La-doped CeO$_2$ recorded at room temperature are shown in Fig. 3.2c. PL emission is strongly dependent on the number of oxygen vacancies present in the CeO$_2$. Due to the addition of La^{3+} in CeO$_2$, the number of oxygen vacancies increases, and the emissions are attributed to the charge transfer from O$_2$ to Ce^{4+}, which is O (2P^6) $\rightarrow$ Ce (4f^0) electron transition or the charge

transfer from oxygen vacancies. The undoped CeO_2 showed two significant peaks at 445nm and 510 nm. For La-doped CeO_2, the emission intensity was higher at 510 nm due to a large number of O_2 vacancies present. Therefore, it can be understood from PL emission spectra that both undoped and La-doped CeO_2 samples that the oxygen vacancy mediated emission from undoped CeO_2 is enhanced due to La doping. In addition to XRD and Raman spectra, PL spectra also confirm the successful doping of La in CeO_2 by the sonochemical method.
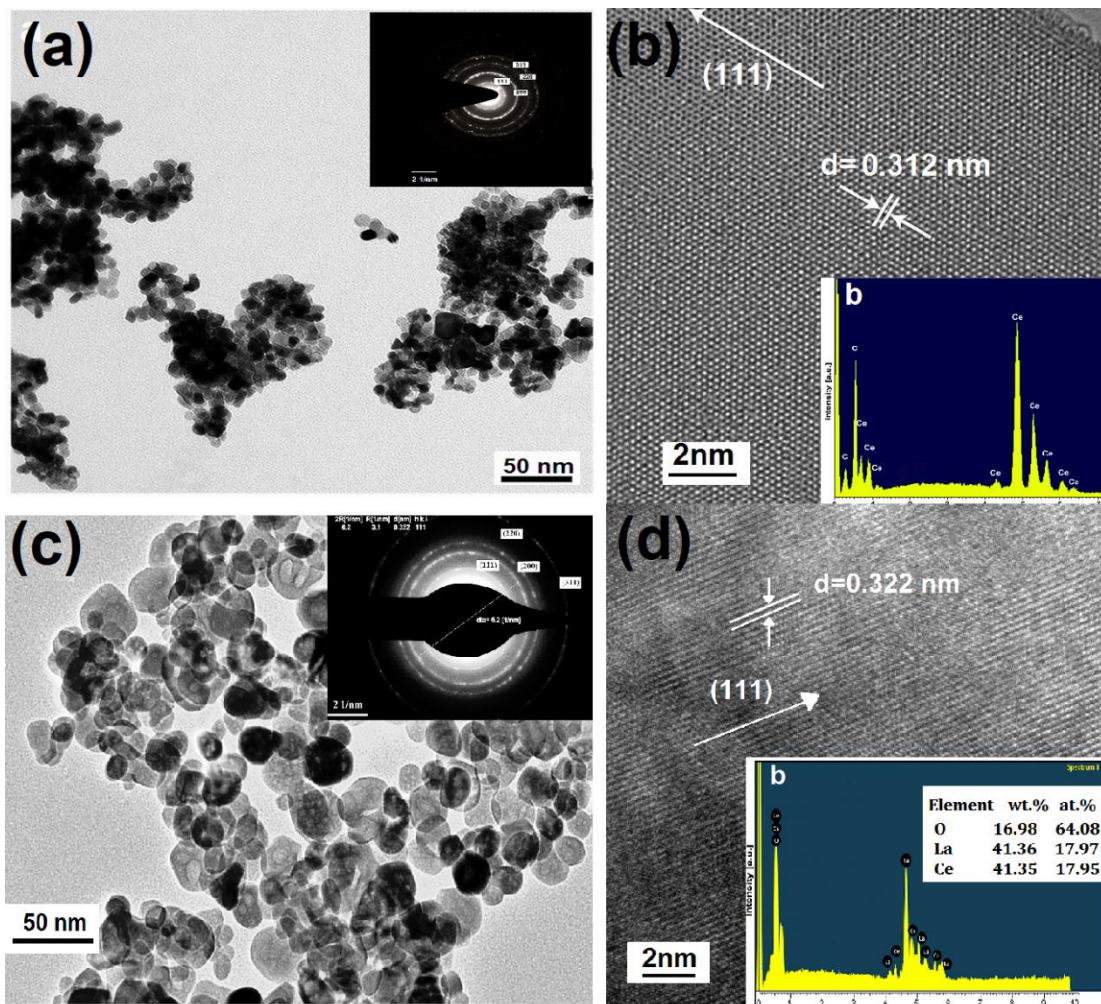
Figure 3.3 (a) TEM image of undoped CeO_2, inset shows the SAED pattern is the diffraction pattern obtained in the reverse space of the lattice planes (b) HRTEM image shows the lattice image of undoped CeO_2 with a d-spacing value of 0.312 nm, inset shows the presence of Ce and O elements (c) TEM image of La-doped CeO_2; inset shows the SAED pattern (d) HRTEM image shows the lattice image of La-doped CeO_2

with the d-spacing of 0.322 nm and it confirms the CeO_2 lattice expansion, inset confirms the presence of La, Ce and O elements in $La_2Ce_2O_7$ atomic ratio.

3.3.1.3 Transmission electron microscopy analysis

The TEM analysis on the undoped CeO_2 and La-doped CeO_2 nanopowder revealed the information about phase evolution and morphology. From Fig. 3.3a, it can be observed that undoped CeO_2 mainly composed of monodispersed particles, which were in size range of 20-50 nm. Supercritical conditions of high temperature and pressure that are produced locally with short lifetimes in a liquid by acoustic cavitation lead to nanopowder formation with a unique size range. The inset in Fig. 3.3a shows the selected area electron diffraction (SAED) pattern of the undoped CeO_2 with the rings made up of individual bright spots. It indicates that the sample consists of nanocrystalline material. In the case of La-doped CeO_2 (Fig. 3.3c), it can be seen from the TEM image that the shape of particles is irregular with an average particle size of well below 50 nm. From Fig. 3.3c inset, the first four rings in the SAED pattern match well with the (111), (200), (220) and (311) planes of the La-doped CeO_2 (JCPDS File 043-1002). d-spacing of the (111) plane was determined by considering the radius of the first ring ($3.1\ nm^{-1}$) and the inverse of that provides d-spacing of the (111) plane, i.e., 0.322 nm, which is in concert with the d-spacing value obtained from XRD analysis.

High-resolution transmission electron microscopy (HRTEM) images were taken at a 2 nm scale for both undoped CeO_2; moreover, La-doped CeO_2 to obtain the internal structure and lattice fringes. Fig. 3.3b clearly, reveals the lattice fringes image of d-spacing 0.312 nm for undoped CeO_2, which corresponds to the distance between (111) facet of the cubic CeO_2. Figure 3.3c shows the lattice image of La-doped CeO_2 with the d-spacing value of 0.322 nm for (111) planes, which is slightly higher than undoped CeO_2 as expected. The higher d-spacing value is because of lattice expansion caused by the doping of La^{3+}. The actual Lanthanum and Cerium contents in the synthesized nanopowder were determined quantitatively by EDX analysis. EDX image of La-doped CeO_2 (Fig. 3.3d inset) shows the atomic percent of each element, and the chemical composition was found to be $La_{0.5}Ce_{0.5}O_{1.75}$, which is in close agreement with

the stoichiometric composition $La_xCe_{(1-x)}O_{(2-\frac{x}{2})}$ (with x = 0.5). It further confirms that the doping was successful. The d-spacing values obtained from all three techniques, namely, XRD, SAED, and HRTEM, are in concert for both La-doped CeO_2 (0.322 nm) and undoped CeO_2 (0.312 nm). The lattice parameters obtained from the NR function and SAED pattern for La-doped CeO_2 also agree well. A lattice expansion from 5.41 Å for undoped CeO_2 to 5.59 Å for La-doped CeO_2 was observed, and it indicates the successful doping of La in CeO_2 fluorite structure. The activation energy required for the doping of La in CeO_2 was supplied by the hot spots created during acoustic cavitation. The acoustic cavitation in liquid-solid slurries also induces high-velocity inter-particle collisions, and the impact of such collisions is sufficient to melt most metals (Pinjari and Pandit, 2011).

3.3.1.4 Dielectric properties

For the dielectric measurements, namely dielectric permittivity (ε_r) and dielectric loss (tan δ), the high dense La-doped CeO_2 ceramic pellet was prepared and sintered at 100 °C for 2 h. Frequency-dependent ε_r values of La-doped CeO_2 in the range from 10 Hz to 1 MHz shown in Fig. 3.4a. It can be observed that high ε_r values at the low frequencies because of interfacial or space charge polarization. At higher frequencies, ε_r value decreases with increasing frequency and reaches a constant value. Interfacial or space charge polarization in La-doped CeO_2 is high due to the higher number of oxygen vacancies and structural in-homogeneity because of the large surface-to-volume ratio of nanoparticles. When the dielectric material is subjected to the external electric field, the space charges present in the material can move and trapped through the defects and vacancies at the interfaces leading to the formation of dipole moments.

Maxwell-Wagner dielectric dispersion theory says that the space charge polarization is dominant at low frequencies, and orientational polarization can be seen at higher frequencies (Arbatti et al., 2007). However, the dielectric permittivity decreases exponentially, and at higher frequencies, the dipoles fail to cope with rapid electric field variations. Therefore, a constant value was obtained for the dielectric

permittivity at higher frequencies. The dielectric loss (tan δ) behavior in a frequency range from 10 Hz to 1MHz is shown in Fig. 3.4b. When AC voltage is applied across a dielectric, the molecular dipoles change their direction many times, depending on the frequency of the applied electric field. This rapid change leads to molecular friction, and some amount of energy is lost as heat (dielectric loss). The dielectric loss will be more at higher frequencies, and the tan δ values were found to increase with increasing frequency due to space charge polarization. The value of tan δ is found to be <0.2 at 1 kHz and reaches ~0.4 at 1 MHz.

The AC conductivity of the prepared La-doped CeO_2 the sample was obtained at different frequencies from 1 kHz to 1 MHz and is shown in Fig. 3.2d. At a higher frequency region, AC conductivity value increases with increasing frequency since the immigration of electrons increased with an increase in frequency. It is due to electronic hopping, creating energetic free electrons in the polarized region. The dielectric properties of synthesized La-doped CeO_2 show that it can be used as a high-k dielectric in thin-film capacitors and transistors.
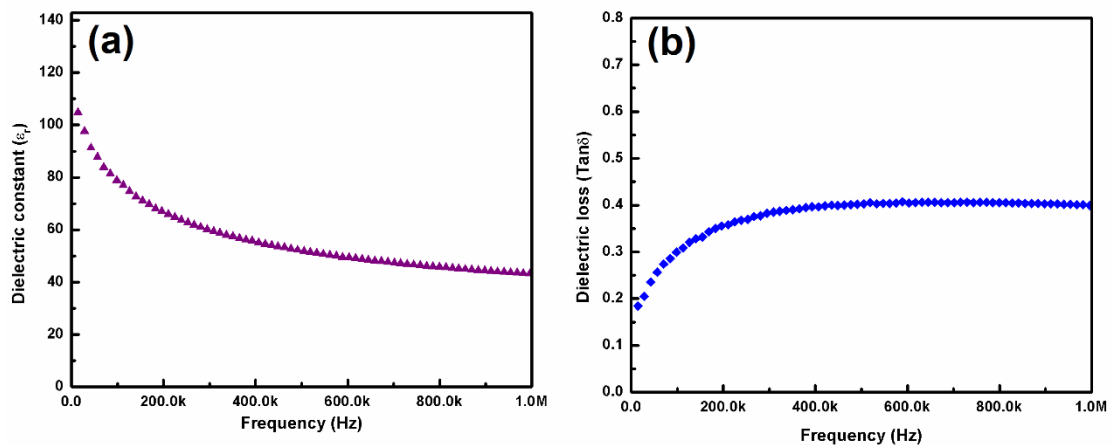
Figure 3.4 Frequency-dependent (a) Dielectric permittivity ε_r values of La-doped CeO_2, in the range from 10 Hz to 1 MHz (b) Dielectric loss (tan δ) of La-doped CeO_2, dielectric data were measured at room temperature.

3.3.2 Thermal behavior, chemical structure, size distribution and morphology of LZO dielectric ink

3.3.2.1 Thermogravimetry analysis

Thermal stability of Lanthanum nitrate, Zirconium acetylacetonates, and LZO ink was studied by TGA, and the respective thermograms are shown in Fig. 3.5. Thermal decomposition of $La(NO_3)_3$ begins with a small mass loss around 100 °C, likely from loss of excess (unbound) water, and proceeds through two significant mass-loss events starting around 180 and 400 °C, attributable to the loss of bound water and nitrates, respectively (Fig. 3.5a). The final mass-loss event starting around 500 °C can be attributed to the expulsion of residual water and nitrates during the final condensation and densification of the oxide. The mass-loss profile of $Zr(C_5H_7O_2)_4$ is more gradual and appears as two significant mass loss events from 90 to 200 °C and 220 to 400 °C. These events likely correspond to gradual water and acetyl group loss, respectively. The mass loss profile of the LZO precursor appears to be an approximate average of the two precursor salts. It shows a gradual mass decrease from 100 to 160 °C (water loss), a mass-loss event around 220 °C (nitrate loss), and a more pronounced, gradual mass loss over several hundred degrees (further nitrate loss, condensation, and densification). Conversion of the LZO precursor to the corresponding oxide is completed by 500 °C (Cloet et al., 2009), which occurs at a lower temperature than for either the La or Zr salts individually. The TGA curve of LZO follows closely that of Zr-precursor salt. The weight loss of LZO is negligible after 500 °C; it confirms that the nitrates and acetates were removed from the precursor, and pure LZO is formed after 500 °C. Although thermal decomposition of the LZO ink is not necessarily representative of the decomposition pathways in thin films, the bulk mass-loss events offer insight into film formation phenomena.

3.3.2.2 X-ray diffraction and particle size distribution analysis

Figure 3.5b shows the powder X-ray diffraction pattern of the as-synthesized $La_2Zr_2O_7$ samples. Powder heat-treated for 4 h at 600 °C resulted in a fully crystalline single-phase material, $La_2Zr_2O_7$. The pyrochlore superstructure reflections from the

planes (222), (400), (440), (622) were evident in the XRD spectra of LZO powders calcined at 600 °C. They coincide with the standard data of $La_2Zr_2O_7$ (ICSD-15475) (Bai et al., 2000), indicating the pure cubic pyrochlore structure with the space group Fd3m and the lattice parameters a = 10.793 nm. The characteristic peaks of the fluorite phase of LZO were not found in the XRD pattern. It confirms that the LZO powder is made of a single pyrochlore phase. Figure 3.5c shows the thin film XRD pattern of fabricated LZO thin film annealed at 350 °C. There are no sharp crystalline peaks in the pattern, which reveals that the fabricated LZO film was in an amorphous state. It can be noted that the film was still in the amorphous state even after annealing at 350 °C for 3 h.
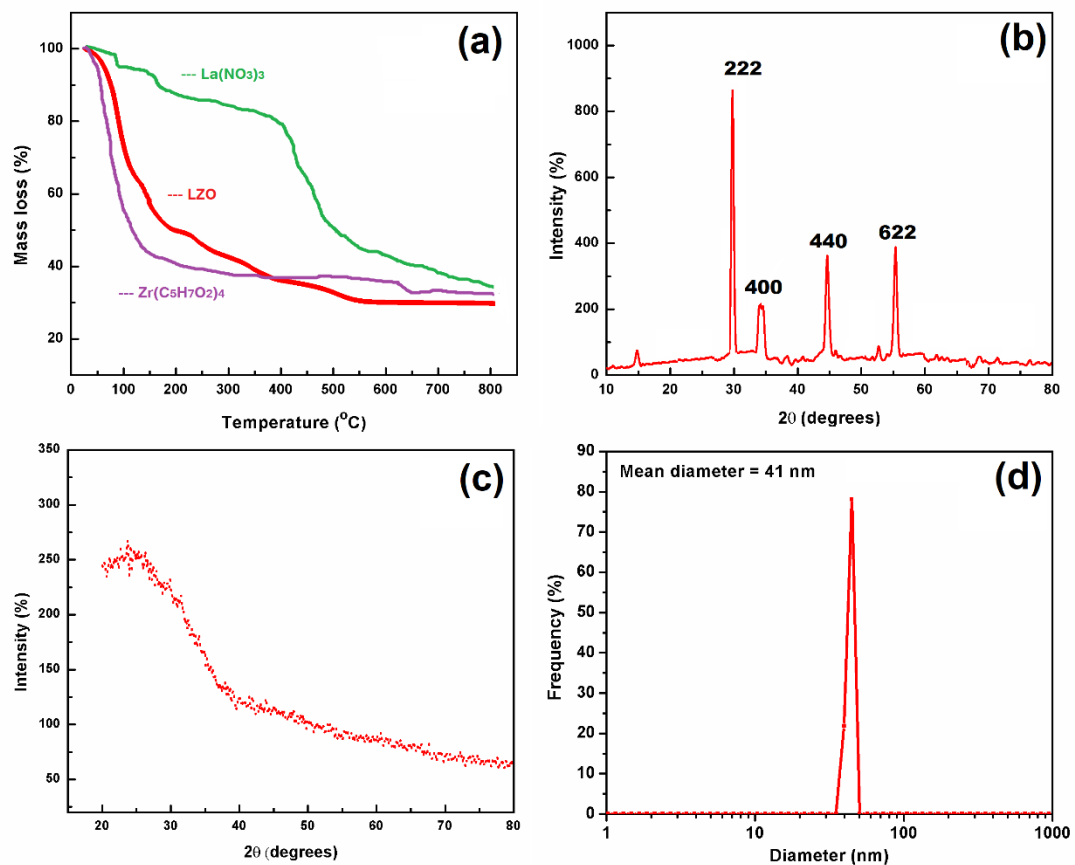
Figure 3.5 (a) TGA thermograph of LZO, lanthanum nitrate, and zirconium acetylacetonates (b) XRD pattern LZO powder obtained by drying of LZO dielectric ink at 90 °C for 3 h in the hot-air oven (c) Thin-film XRD of spin-coated LZO dielectric film (d) Particle size distribution of LZO dielectric ink contains monodispersed particles with a mean diameter of 41 nm.

Thin-film XRD indicates that the crystallization temperature of the LZO film is higher than 350 °C. As a gate dielectric, an amorphous film is preferred over a poly-crystalline film because grain boundaries can induce a leakage current through the dielectric. Particle size analysis was done using a zeta size analyzer (Horiba Zeta-sizer). This instrument determines the size, high-resolution size distributions, and particle concentration. Unique optics can analyze polydisperse assemblages of particles in liquids and resolve separate size modes in complex samples. The LZO particles are in the range of 35-50 nm, and the average particle size is 41 nm, as shown in Fig. 3.5d. This result significantly shows that the prepared LZO ink contains colloidal nanoparticle dispersion.

3.3.2.2 Surface roughness, film thickness, and capacitance measurement
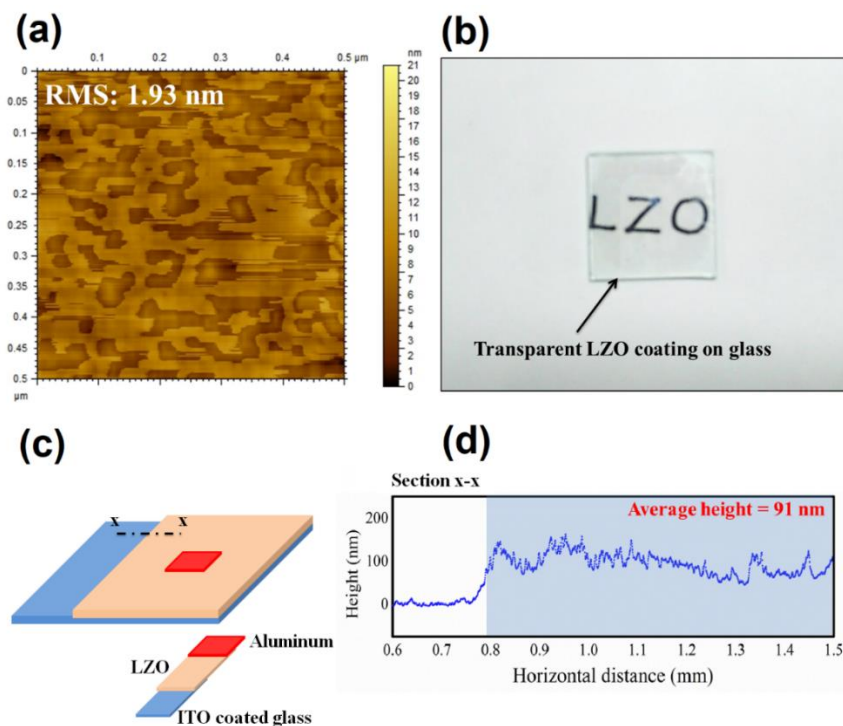
Figure 3.6 (a) Surface roughness image of LZO thin-film obtained by AFM (b) Fabricated transparent image of LZO thin-film spin-coated on ITO glass (c) Schematic of the thin-film capacitor made of LZO dielectric layer with top and bottom electrode (d) Thickness of the fabricated LZO thin-film measured by a profilometer. The thickness of LZO dielectric film is measured using the profilometer and roughness of the film determined using Atomic Force Microscopy (AFM).

Figure 3.6c shows the schematic of the thin-film capacitor made of the LZO dielectric layer with aluminum top and ITO bottom electrode to complete the circuit. The aluminum layer was deposited by the thermal evaporation technique with the controlled thickness. Figure 3.6d represents the thickness profile of the LZO film coated on the ITO glass substrate. The thickness of the fabricated LZO film found to be 91 nm measured using a profilometer. The surface roughness of the LZO film is determined to be 1.93 nm, shown in Fig. 3.6a. The overall surface of the LZO film is smooth and homogeneous, over an area of 2.5 μm^2. Transparent LZO spin-coated on ITO glass is shown in Fig. 3.6b. Capacitance is a constant value of the capacitor, which is determined by the LZO dielectric layer. The capacitance of a capacitor is plotted against a function of frequency shown in Fig 3.7a. The capacitance decreases with the increase in frequency show the typical behavior of the thin-film capacitor. In Fig. 3.7b, the capacitance is plotted against a function of applied voltage, where the capacitance (C) of 4.5 nF/cm^2 at 1 kHz is stable for different applied voltage (V).
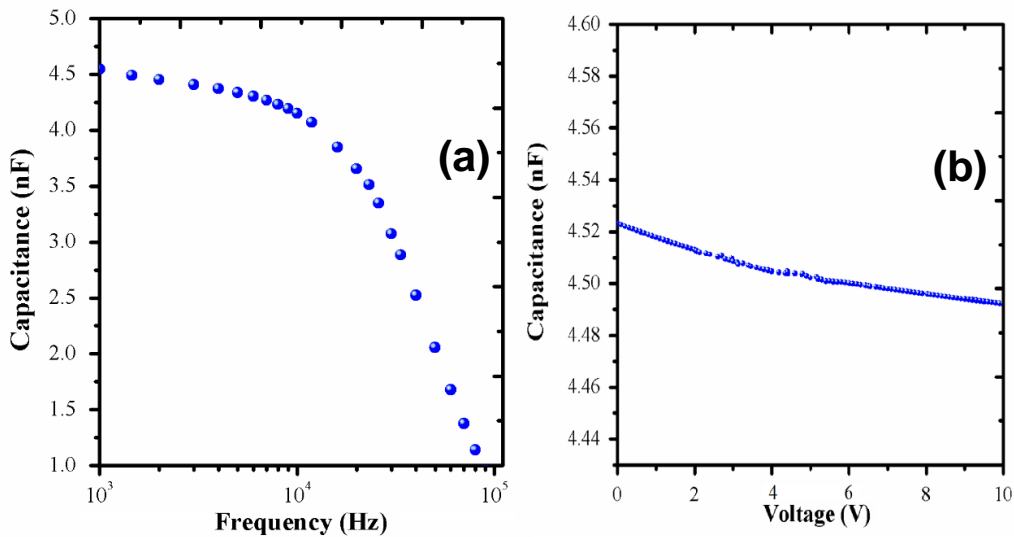
Figure 3.7 (a) Capacitance vs. frequency response b) Capacitance vs. voltage response of the thin-film capacitor made of LZO dielectric layer prepared using LZO dielectric ink.

3.4 SUMMARY

LCO nanopowder was synthesized by a sonochemical approach at a relatively lower temperature (70 °C). The supercritical condition created due to the sonochemical effect in the liquid medium was sufficient for doping of La^{3+} inside CeO_2 fluorite structure, without any additional heat treatment like calcination. Raman spectroscopy and PL emission spectra confirmed the doping of lanthanum inside the fluorite structure of CeO_2. No secondary phases like La_2O_3 and $La_2(CO_3)_3$ were present in the synthesized nanopowder, as confirmed by XRD analysis. TEM analysis revealed that particles were in a size range of 20-50 nm. La-doped CeO_2 possesses a very high dielectric permittivity of 106 at 1 kHz with a very less dielectric loss of 0.2.

Lanthanum Zirconium Oxide (LZO) dielectric ink was prepared. The nanodispersion of LZO was confirmed by particle size analysis. Nano-dispersion/ dielectric ink showed particles with an average size of 41 nm. Dielectric ink was directly used for the fabrication of the thin-film capacitor. Various characterization techniques were used to examine the size, purity, thickness of the thin film, and capacitance measurement. A sonochemical route is a promising approach for the preparation of dielectric ink in a single-step method.

CHAPTER 4

FABRICATION OF PMMA/LZO AND PVDF-HFP/LZO DIELECTRIC COMPOSITES FOR HIGH ENERGY STORAGE DENSITY APPLICATIONS

4.1 INTRODUCTION TO PMMA BASED COMPOSITES

Polymer nanocomposites are being used overwhelmingly in high-energy storage density devices and open up many research opportunities in recent years. The energy storage density of a polymer composite depends mainly on the dielectric permittivity and loss factor. Various approaches such as sol-gel, chemical vapor deposition (CVD), template synthesis, and melt mixing are being used to fabricate the polymer composites with high-energy storage density by improving their dielectric permittivity (Ruiz-Hitzky et al., 2011). In PMMA based composites, a high (> 30 vol%) filler loading significantly enhances the dielectric permittivity of the PMMA but also makes the composite film brittle. Therefore, they suffer from high dielectric loss. The core-shell high-k PMMA@$BaTiO_3$ and polystyrene @$SrTiO_3$ nanocomposites for energy storage applications have been reported (Yang et al., 2012). The nanocomposite of PMMA/hyperbranched aromatic polyamide (HBP)@$BaTiO_3$ by blending the core-shell HBP@$BaTiO_3$/$CaCu_3Ti_4O_{12}$ nanoparticles with PMMA was reported by Xie et al. (2013). However, high hysteresis loss and leakage current make it challenging to use $BaTiO_3$, $SrTiO_3$, and $CaCu_3Ti_4O_{12}$ in the polymer matrix. These ceramics need further surface modification or functionalization to use in energy storage devices with a low dielectric loss.

On the other hand, while considering the inorganic dielectric as a filler, the Lanthanum Zirconium oxide (LZO-$La_2Zr_2O_7$) is a promising amorphous high-k dielectric material with less leakage current and high dielectric permittivity. Combining high-k dielectric LZO with PMMA provides a new opportunity for high-k polymer nanocomposite materials in transparent, flexible electronics. Although LZO inorganic

fillers provide various advantages in fabricating high-k polymer nanocomposites, they also offer many challenges in the realization of high-performance polymer nanocomposites. Typical challenges include achieving homogeneous dispersion of LZO fillers in polymer and tailoring interface between polymer and filler, which play a crucial role in obtaining desirable electrical characteristics. In order to get a high dielectric permittivity, a high-volume fraction of fillers is usually needed, which causes difficulty in getting uniform dispersion (Wang et al., 2015). However, the homogeneous dispersion of LZO fillers in PMMA and the strong interfacial adhesion between fillers with PMMA matrix can be achieved with a proper fabrication method. In short, the preparation process for polymer composites is crucial because it affects their dielectric properties. The process type and conditions for its operation must be determined by the material's physical, chemical, rheological, and thermal characteristics.

PMMA-LZO composite dielectric film is fabricated with a minimum filler quantity and better dispersion of LZO fillers in PMMA, considering all the issues mentioned above. Uniform dispersion of LZO filler in the PMMA matrix obtained by sonication. The PMMA-LZO dielectric solution was directly spin-coated on the Indium tin oxide/base silicon dioxide (ITO/SiO$_2$) substrate under optimized spin coating conditions to obtain a desired thickness of the coating. The dielectric permittivity and energy storage density of LZO-PMMA nanocomposite films were improved significantly with a low dielectric loss compared to neat PMMA.

4.2 EXPERIMENTAL METHOD

4.2.1 Preparation of PMMA-LZO composite solution

2 g of PMMA (Synthesis grade with average molecular weight ~15 kDa by GPC from Sigma-Aldrich) powder was dissolved in 50 ml of toluene using a magnetic stirrer for 20 min. LZO solution was prepared by dissolving 2 g of LZO powder in 20 ml of distilled water (Sigma-Aldrich)/10 ml of acetic acid (CH$_3$COOH, 99.8%, Sigma-Aldrich)/10 ml of triethanolamine (N(CH$_2$CH$_2$OH)$_3$, 99.9%, Merck) system. LZO

solution was taken in 2, 5, 10, and 15 vol% and mixed with PMMA solution using a probe-type sonicator. 20 kHz frequency generator (500 W) that was operated on a pulsed mode (4 s ON/ 2 s OFF) at a 40% power amplitude (200 W) for 30 min. The maximum temperature of the solution reached during sonication was 60 °C. A well-dispersed PMMA-LZO solution was directly spin-coated on ITO/SiO$_2$ without any further processing.

4.2.2 PMMA-LZO dielectric film fabrication

The ITO/SiO$_2$ (25×25×0.7) mm^3 square glass with a surface resistivity of 10 ohms/sq. Cleaned with acetone and kept in the ozone chamber for 30 s. PMMA-LZO solution containing a different composition of LZO was spin-coated on ITO/SiO$_2$ substrate using a vacuum-free spin coater (Navson-NT1200). The spin coater was operated with an initial speed of 1000 rpm for 10 s, and then the speed was increased to 3000 rpm for 30 s with an acceleration time of 5 s. The as-spun film was dried under the UV chamber for 30 min. The copper layer was deposited on the PMMA-LZO film to make a film capacitor. The dielectric properties of PMMA-LZO film were studied using an impedance analyzer (IM3536, Hioki, Japan) to determine the dielectric permittivity, loss tangent in the frequency range of 1 Hz-1 MHz. All impedance measurements were carried out at room temperature. Energy storage density and breakdown strength were determined by the ferroelectric workstation (Radiant, Inc.). The x-ray diffraction pattern was recorded by Bruker D8 Advance X-ray powder diffractometer using Cu-Kα radiation (40 kV, 40 mA) (wavelength λ=1.5406 Å). Film thickness and surface morphology were measured using SEM (JEOL JSM 6400). Schematics of PMMA-LZO dielectric film coated on ITO/SiO$_2$ substrate and a cross-sectional view of ITO/PMMA-LZO/Copper film capacitor are shown in Fig. 4.1. Copper was deposited on LZO-PMMA coated ITO/SiO$_2$ substrate as a top electrode to analyze the dielectric properties of the LZO-PMMA film. PMMA-LZO transparent flexible film with the copper masked layer is shown in the inset of Fig. 4.1.
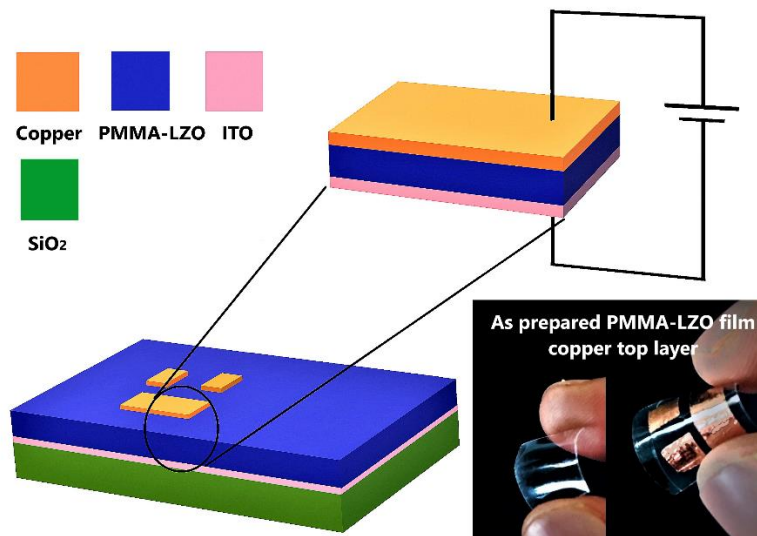
Figure 4.1 Schematics of PMMA-LZO dielectric film coated on ITO/SiO$_2$ substrate and a cross-sectional view of ITO/PMMA-LZO/Copper capacitor film. Copper was deposited as a top electrode by thermal evaporation for the analysis of the dielectric properties of the LZO-PMMA films. The inset shows as-prepared PMMA-LZO dielectric film peeled off from the ITO-coated glass substrate (left side) and copper deposited PMMA-LZO dielectric film (right side).

4.3 RESULTS AND DISCUSSION

4.3.1 X-Ray Diffraction Pattern

PMMA is an amorphous transparent thermoplastic polymer. Since it has no crystalline phase, there are no scattering sites for diffraction. Hence, there were no sharp peaks observed in the XRD pattern of neat PMMA, as shown in Fig. 4.2. However, a low-intensity peak at a 2θ value of 23° was observed due to ordered packing of polymer chains. At 2 vol% LZO loading, there was no crystallinity noticed in PMMA composite. However, when the LZO content increases gradually from 5% to 15 vol% in PMMA, the XRD patterns of the respective samples show the crystal peaks corresponding to La$_2$Zr$_2$O$_7$ with major diffraction peaks identified as a pyrochlore structure (ICSD-15475). The different planes of neat LZO were marked in Fig. 4.2. As LZO finds specific scattering sites at particular diffraction angle 2θ (30°), intensive peaks were

recognized in samples with higher LZO content, as shown in Fig. 4.2. At 15 vol% LZO content in PMMA, peaks at 30-32° and 45-48° appear similar to that of neat LZO. Though the intensity is low, the characteristic peaks of LZO as per standard ICDD pattern appeared in all composite samples. Therefore, the XRD results confirm that the prepared composite material is still amorphous with 2 vol% LZO content. However, the crystalline peaks of LZO start appearing from 5 vol%. PMMA-LZO (15 vol%) showed an apparent crystalline behavior, as evident from the dominant LZO peak intensities.
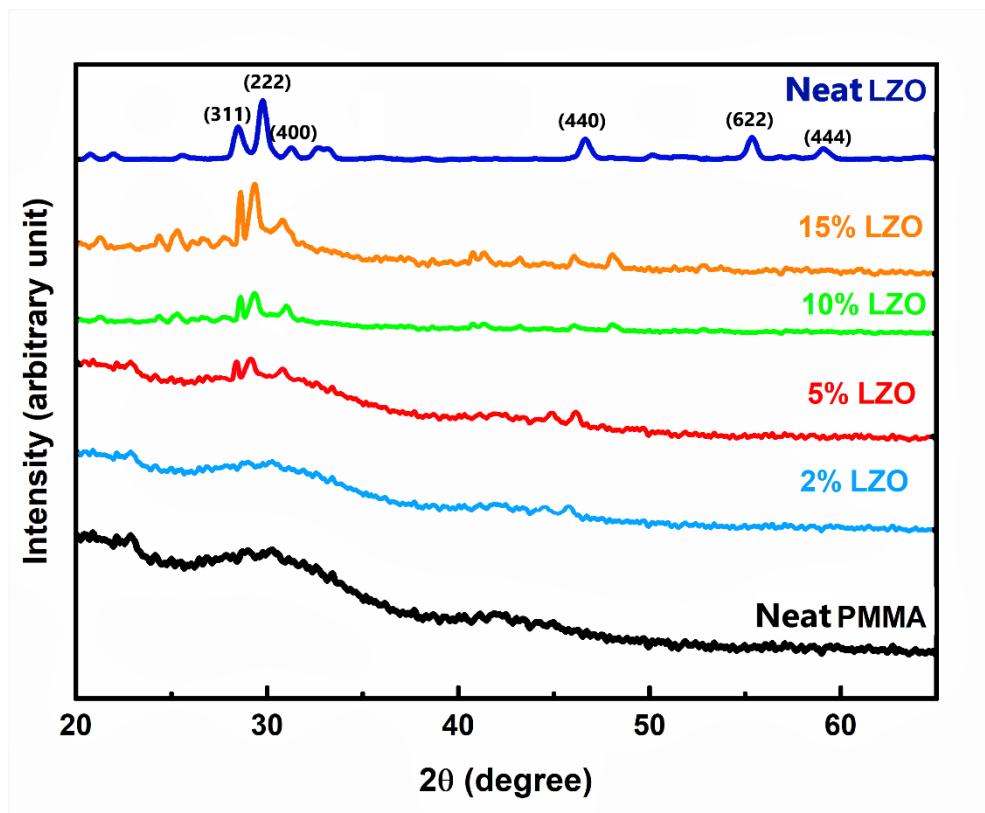
Figure 4.2 XRD pattern of neat PMMA, neat LZO, and PMMA-LZO composite film with different LZO filler loadings.

4.3.2 Surface morphology and film thickness

The morphology of PMMA-LZO composite films with different LZO content is presented in Fig. 4.3. SEM images of all samples are presented in Fig. 4.3 (a-e) at the same magnification for comparison. At lower LZO contents (Fig. 4.3a&b), though the LZO particles were fairly distributed in the PMMA matrix, the surface was not entirely

covered. The average distance between the LZO particles in PMMA matrix at lower LZO loadings is ~1 µm. LZO particles were still evenly distributed in a PMMA matrix at higher LZO contents (Fig. 4.3c&d), and the interparticle distance becomes smaller than 1 µm. However, particle agglomeration was noticed at 15 vol% LZO loading.
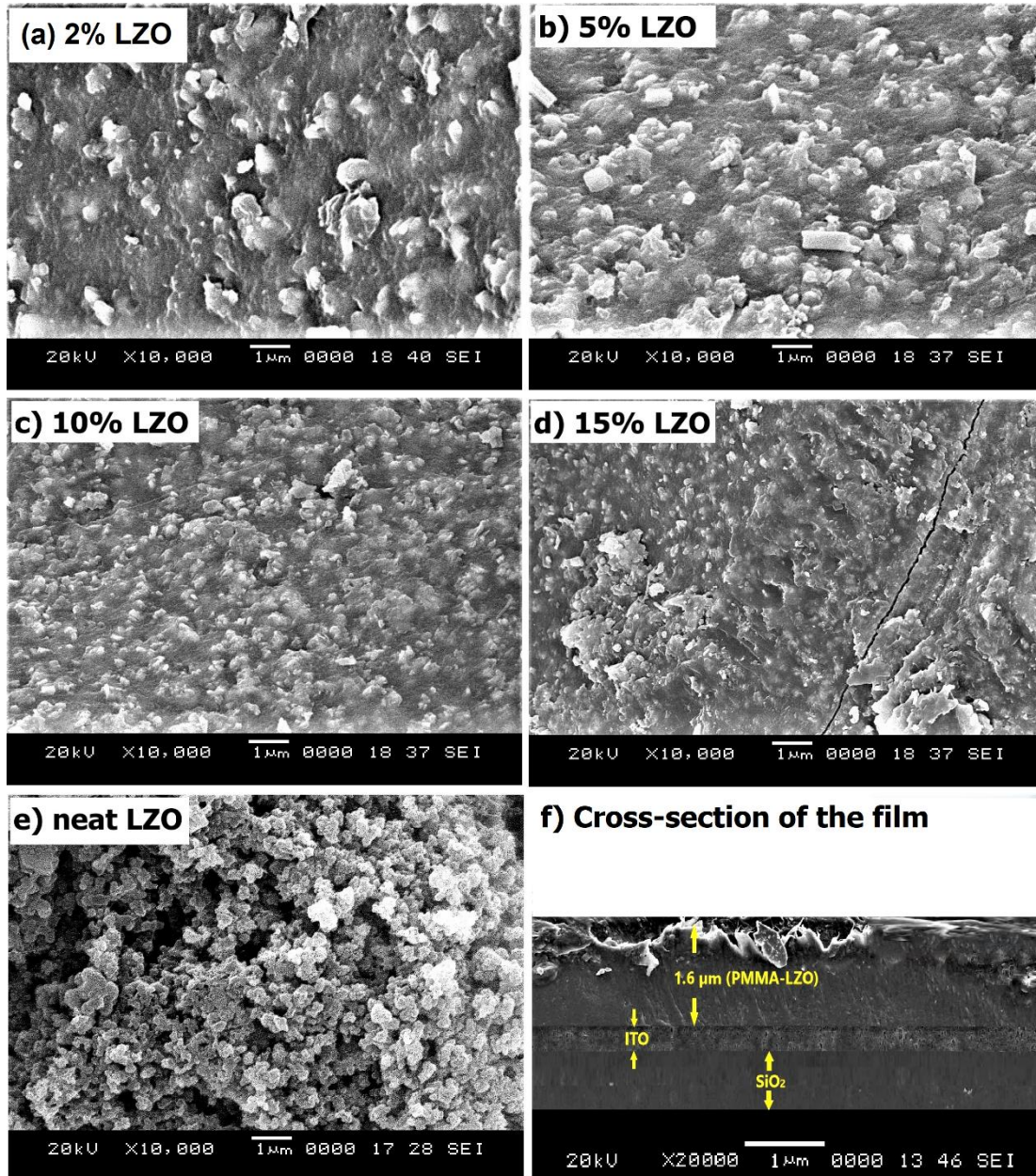
Figure 4.3 SEM images of PMMA-LZO composite films with different LZO filler loadings taken at 1µm scale (a) 2 vol% LZO (b) 5 vol% LZO (c) 10 vol% LZO (d) 15 vol% LZO (e) neat LZO (f) Cross-sectional SEM image of PMMA-LZO composite film coated on ITO/SiO$_2$ substrate.

Figure 4.3e shows neat LZO particles sintered whose sizes are below 1 µm. Agglomerated particles lead to the charge trapping and creation of a local electric field under an applied voltage. When frequency increases, the trapped charge at the agglomerated site starts losing its energy as heat. High dielectric loss in 15 vol% LZO filled PMMA film was observed. The bottom line is that it is preferred to have a uniform distribution with fewer particles of LZO fillers in PMMA rather than having more particles with the agglomerated state in order to achieve better dielectric properties. Three distinct layers of PMMA-LZO, ITO, and SiO_2 can be seen in the composite film's cross-sectional SEM image (Fig. 4.3f). The thickness of the composite film was measured as 1.6 µm.

4.3.3 Dielectric properties of LZO-PMMA films

LZO filler content in polymer composite plays a crucial role in enhancing the dielectric properties of a polymer matrix. An increase in filler loading indeed increases the dielectric permittivity of the composite but suffers from dielectric loss. However, higher filler loading also leads to the brittleness of the film. The brittle film is not advisable to use in thin-film capacitors or transistors. The filler loading was chosen as minimum as possible to avoid high dielectric loss and focused on achieving uniform distribution of LZO particles with the aid of ultrasound. Uniform dispersion of LZO in the polymer is facilitated when the solvent dissolves the polymer at low temperature with minimum time. During sonication, LZO particles dispersed well in the PMMA matrix within 30 min.

Dielectric permittivity of neat PMMA, neat LZO, and PMMA-LZO composite films with different LZO contents are presented as a function of frequency in Fig. 4.4a. The dielectric permittivity changes as a function of polarizable molecules or atoms present in a material. PMMA has lower dielectric permittivity since there are no valence electrons in PMMA. The molecular polarizability of the C-C bond in PMMA is very low compared to other inorganic bonding. The dielectric permittivity of a material is a critical parameter to store more charges on the capacitor plate. The dielectric permittivity of composite increases as the content of LZO increases due to the interfacial polarization. Maxwell–Wagner–Sillars (MWS) model explains the

phenomenon of interfacial polarization (Dang et al., 2012). When the LZO particles are in the PMMA matrix, the dielectric mismatch between a polymer and inorganic rises to high dipole moment in the composite. Enhanced dipole moment leads to rapid interfacial polarization. Due to this effect, the charge holding capacity of the composite film increases.

.
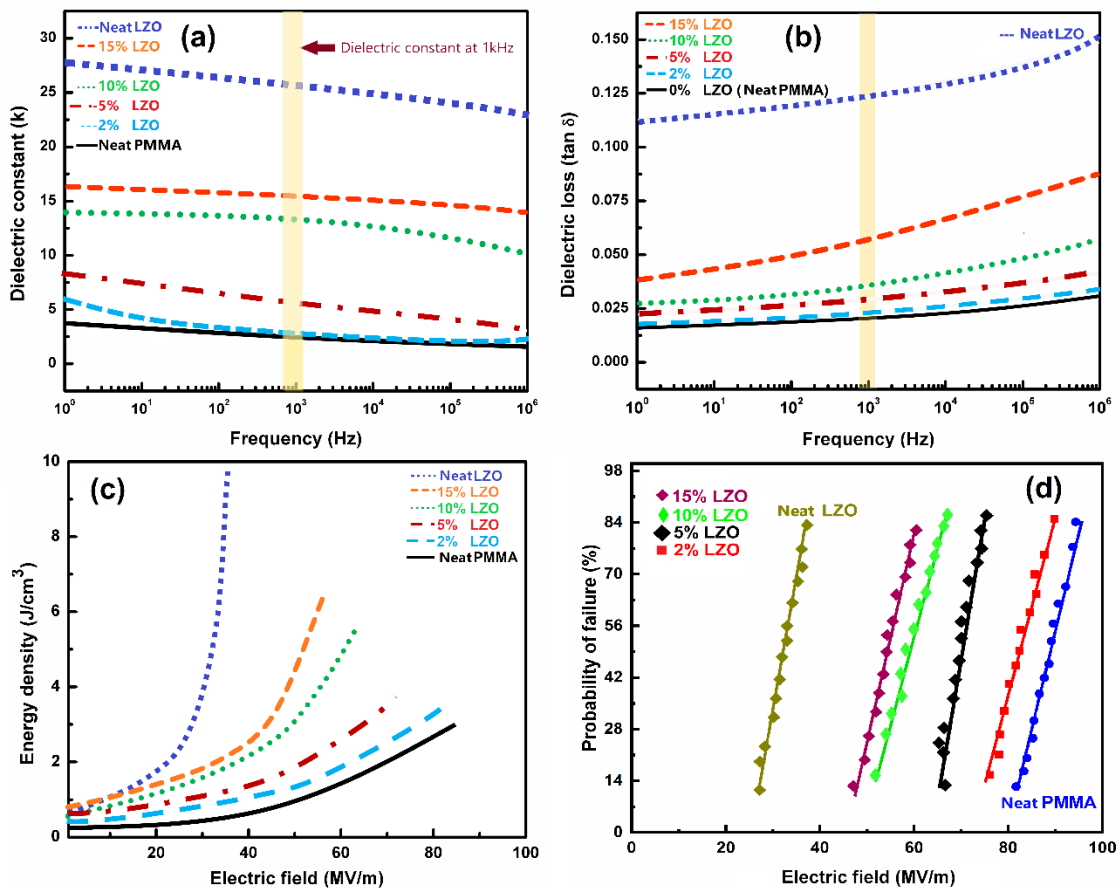
Figure 4.4 (a) Dielectric permittivity vs. frequency (b) Dielectric loss (tan δ) vs. frequency in the range of 10-10 MHz (c) Energy storage density vs. electric field (d) Breakdown strength is calculated using a probability of failure vs. electric field for neat PMMA, neat LZO, and PMMA-LZO composite films with different LZO filler loading.

The dielectric loss (tan δ) also was recorded for neat PMMA, neat LZO, and PMMA-LZO composite films as a function of the frequency from 1 Hz to 1 MHZ (Fig. 4.4b). As the LZO content increases, the dielectric loss of PMMA also increases. The dielectric loss for neat PMMA, 2%, 5%, and 10 vol% LZO filled PMMA lies below

0.027 at 1 kHz. However, for the 15 vol% LZO, dielectric loss increased to 0.0582, which is almost three times larger than that of neat PMMA. The interaction between LZO particles becomes significant at higher concentrations of LZO because the distance between fillers in the PMMA matrix is extremely close, especially for nanosized fillers. Because of the high concentration of LZO nanoparticles, the local electric field generation accounts for the dielectric loss. Jaysundere and Smith's realistic mixing rule can describe the dielectric loss in polymer nanocomposite (Jayasundere and Smith, 1993). According to their rule, the electric field formation with dielectric particles embedded in a continuous PMMA matrix always depends on the polarization of inorganic particles and their distance. By increasing the filler concentration, particles come closer to each other and lead to rapid electric field formation, which accounts for the dielectric loss in the form of heat. An increased dielectric loss at all frequencies for the composite samples with increasing LZO loading because of electrical conduction and dipolar polarization was observed

Dielectric permittivity, dielectric loss, breakdown strength, and energy storage density of PMMA-LZO composite films with different LZO filler loading are presented in Table 4.1. The dielectric breakdown strength of PMMA decreased from 85.3 to 54 MV/m at 15 vol% LZO loading. Also, the dielectric loss increased almost three folds larger than that of neat PMMA. As 15% LZO loading leads to agglomeration and crack in PMMA-LZO films, the PMMA matrix loses its flexibility, which results in a high dielectric loss. Increased LZO content accounts for the nanoparticle percolation and high electric field gradient between neighboring LZO particles due to which the host PMMA chains fail to respond to the abrupt decrease in breakdown strength. These results suggest that the optimal LZO volume fraction for the maximum energy density must be 10 vol%.

Table 4.1: Summary of dielectric properties such as dielectric permittivity, energy storage density, and breakdown strength of PMMA-LZO composite dielectric films with different LZO filler loadings.

LZO content in PMMA-LZO composite films (vol%)	Dielectric permittivity (k) at 1 kHz	Dielectric loss (tan δ)	Energy storage density (J/cm^3)	Breakdown strength (MV/m)
0 (Neat PMMA)	3.1	0.0183	2.91	85.3
2	5.7	0.0186	3.3	80
5	8.9	0.025	3.86	71
10	13.4	0.0271	5.94	63.6
15	15.3	0.0582	6.53	54
100 (Neat LZO)	26	0.120	9.92	31.8

4.3.4 Energy storage density and breakdown strength

PMMA-LZO film capacitors store energy in the form of an electric field. When voltage is applied across, the capacitor carries current until the potential attains the voltage rating of the capacitor. If the applied potential is higher, it may result in damage to the capacitor. The breakdown strength of the polymer composite should be high enough to withstand the applied voltage. The stored energy is directly proportional to the square of the voltage across the capacitor. PS-b-PMMA copolymer was developed to improve energy storage and breakdown strength (Samant et al., 2016). A copolymer having different monomer in backbone changes the configuration of the polar molecules results in the improved dielectric properties. The energy storage density of neat PMMA and neat LZO was measured as 2.91 J/cm^3 at 85.3 MV/m and 9.92 J/cm^3 at 31.8 MV/m electric field, respectively, as shown in Fig. 4.4c. The storage density of PMMA is improved up to 6.53 J/cm^3 at 15 vol% LZO loading. However, at 15 vol% LZO, since particle agglomeration begins, and the cracks and void defects present in the film result in high dielectric loss and reduced dielectric field strength. Nevertheless, 10 vol% LZO-PPMA film provides an improved storage density of 5.94 J/cm^3 while the dielectric loss was comparatively lower. The electric field strength of 10 vol% LZO-

PMMA is 63.6 MV/m, but it decreased to 54 MV/m at 15 vol% LZO content. Since the local electric field formation is high in inorganic fillers due to the conductive path, the electric field strength is always low for inorganic high-k dielectrics compared to polymers.

The breakdown strength of a dielectric film has a critical role in energy storage devices. The probability of failure of LZO-PMMA composite films as a function of breakdown strength is plotted in Fig. 4.4d. 15 vol% LZO-PMMA showed a low breakdown strength of 50 MV/m, while a neat PMMA showed 85.3 MV/m. The breakdown strength of PMMA decreases with LZO filler content due to uneven electric field distribution as the number of LZO particles increases. The inherent difference in conductivity and permittivity between LZO filler and PMMA matrix results in the space charge formation opposite to the applied electric field. As the LZO filler loading increases from 2 to 15 vol%, energy storage density increases significantly compared to that of neat PMMA. However, PMMA-LZO film suffers from dielectric loss and reduced breakdown strength.

The phenomenon was ascribed not only to the low electrical breakdown of LZO fillers themselves but also to the possible path of percolation in the PMMA matrix through the LZO islands that can be seen from SEM images (Fig. 4.3c&d). The breakdown strength of the composites is strongly affected by interfacial areas, agglomerations, and voids. These aspects result in an inhomogeneous breakdown of the electrical field strength in the polymer matrix and lead to a reduction in the effective storage strength of the PMMA-LZO nanocomposites. Polymer chains start conducting electricity due to the formation of a tangential electric tree with an increase in applied voltage. The failure might be associated with an avalanche discharge process originating with the promotion of few valence electrons into a conduction band. Breakdown happens when the formation of a threshold electric field due to the intense and disruptive flow of charges, which generates an irreversible modification in polymeric chains and materials can melt locally.

4.3.5 Effect of LZO filler loading in PMMA on dielectric properties at 1 kHz
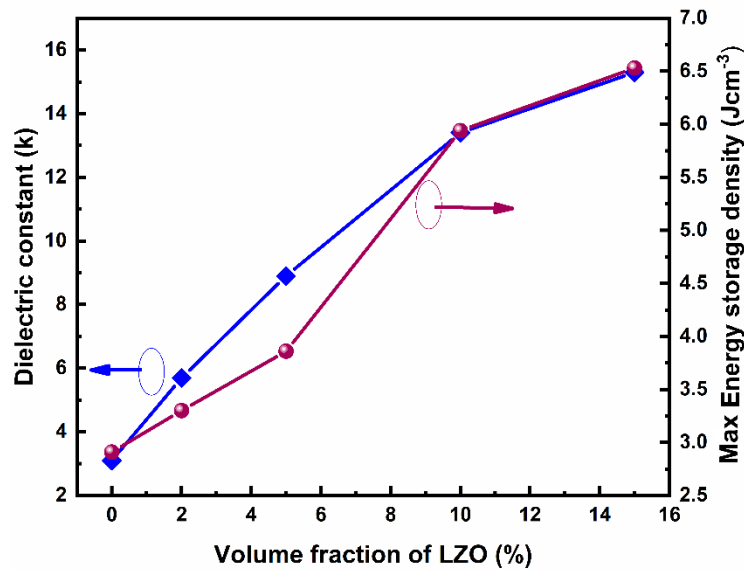
Figure 4.5 Dielectric permittivity at 1 kHz and max energy storage density of the PMMA-LZO films as a function of volume fraction of LZO in PMMA-LZO composite films.

For practical applications, it is essential to achieve high energy density with high-efficiency, as dielectric losses often contribute to heating and degenerating material performance and reliability. The role of the LZO content (2–15 vol%) on the dielectric properties (dielectric permittivity, dielectric loss, energy storage density, and breakdown strength) of the composite film was investigated to determine the optimum LZO loading. It was found that the dielectric permittivity and energy storage density of composites increases with LZO content, as shown in Fig. 4.5. Even though both energy storage density and dielectric permittivity were followed a rapid increase with LZO content, 10 vol% LZO was found to be optimum loading considering the stability of the film.

Table 4.2 reports the comparison of dielectric properties of a PMMA-LZO composite film prepared in this work with various other composite films reported in the literature. It can be noted that PMMA-LZO film properties are comparable with that of other composite films. However, the dielectric loss of other composite films was 2-3 times higher than that of PMMA-LZO film (present work) except PS-b-PMMA. However, PS-b-PMMA copolymer film shows less energy storage density compared to

other films. The energy storage density of 5.94 J/cm^3 was achieved with a dielectric loss of 0.0271 in 10 vol% PMMA-LZO. The high dielectric loss deteriorates the films and accounts for the poor device performance. Keeping the dielectric loss as low as possible with energy storage density above 4 J/cm^3 is technically preferred in transparent electronic devices. Thus, the present work demonstrated the transparent PMMA-LZO composite with moderate energy storage density and low dielectric loss. A properly optimized filler fraction and the nanoparticle-polymer interface are essential for achieving desirable high dielectric properties and thus high energy storage capacity.

Table 4.2: Comparison of dielectric properties of PMMA-LZO (10 vol%) composite film with other composite films reported by other research groups.

Material	Dielectric permittivity	Dielectric loss	Energy storage density (J/cm^3)	Breakdown strength (MV/m)	Reference
PMMA-LZO (10 vol%)	13.4	0.0271	5.94	63.6	Present work
PMMA/P(VDF-HFP)-BST	15	0.05	10.3	378	(Feng et al., 2018b)
PVDF-HFP)-Hydantoin BaTiO$_3$	21	0.04	8.13	325	(Luo et al., 2015)
PS-b-PMMA	2.75	0.02	4.6	289	(Samant et al., 2016)
PMMA-SiO$_2$@MgO	7	0.14	-----	167	(Xie et al., 2013)
PMMA@BT	45	0.06	-----	----	(Huang and Jiang, 2015)

4.3 INTRODUCTION TO PVDF BASED COMPOSITES

Dielectric composites that provide a high dielectric permittivity (k) and dielectric breakdown strength without an excessive dielectric loss is necessary for high energy-storage capacitors. Because of its inherent high energy density, PVDF (polyvinylidene fluoride) based polymers are the preferred choice for capacitive devices. PVDF-based copolymers were often used to improve nanocomposites' electrical characteristics (Yang et al., 2013). Among all PVDF based copolymers, PVDF-HFP exhibits high breakdown strength and high energy storage density. However, PVDF-HFP suffers from a lower dielectric permittivity compared to other PVDF copolymers. Recently, the fabrication of PVDF-BST (Hu et al., 2015), PVDF-CTFE/BaTiO$_3$ (Suematsu et al., 2016), PVDF-HFP/GO, PVDF-HFP/TiO$_2$ (Kim et al., 2006) have been reported to improve the dielectric properties. However, the main drawback of the above reported dielectric composites is that the high-volume fraction (>40-50 vol%) of the filler is needed to achieve high dielectric permittivity with energy storage density. However, the high vol% of fillers tend to increase the particle packaging density, leading to a breakdown path via aggregated fillers (Cheng et al., 2002).

Therefore, there is a need for an alternative approach to overcome these issues in the fabrication of high-performance dielectric composite films. In this chapter, a low temperature (70 °C) formulation of PVDF-HFP/LZO composite ink using the sonochemical approach followed by dielectric thin-film deposition via spin coating technique is presented. The concept of composite ink enables us to avoid several processing steps and the agglomeration of colloidal LZO particles. The optimum volume fraction of LZO colloidal particles in the PVDF-HFP solution is achieved through computational simulations. The composite dielectric ink contains uniformly dispersed LZO colloidal particles in the PVDF-HFP polymeric solution prepared at low temperature, which can be directly printable on a substrate to build a thin-film capacitor. The sonochemical approach allows greener and inherently safer to create microscopically supercritical conditions of high temperatures and pressures in liquids that are not easily achievable by other conventional methods such as hydrothermal, sol-

gel, solution combustion and microemulsion. This exciting approach not only benefits better dispersibility of LZO in a polymer medium but also affords a high energy density composite ink at a high electric field. The effect of LZO content on dielectric properties was thoroughly investigated. The electric field distribution, polarization, and energy storage density of PVDF-HFP/LZO thin-film were calculated using FEM based COMSOL Multiphysics. The results obtained from the experiments and computational simulations are compared.

4.4 MODELING AND SIMULATION

4.4.1 Model set-up

The software COMSOL Multiphysics was used to study the electric field formation, polarization, and energy storage phenomena in a thin-film capacitor made up of PVDF-HFP/LZO dielectric layer. The different volume fractions (5, 10, 15, 20, 30 vol%) of LZO was considered in the PVDF-HFP solution. For each vol% of LZO, the energy storage density and breakdown strength of the dielectric layer was determined. A geometry was built in the desired space dimensions, to study a thin-film capacitor model, and after that, material properties such as dielectric permittivity, and AC conductivity was provided. The electrostatics under AC/DC module calculates the displacement of an electric field and polarization in a thin-film capacitor under given conditions where the distribution of electric charge is prescribed. The physical interface solves the Gauss's law (Vold, 1993) and Maxwell constituent equations (Dziaugys et al., 2015) to determine the electric field formation using the electric potential as the dependent variable. Two fundamental boundaries, such as outer and interior, were applied. An exterior boundary is an outer boundary of the modelling domain, and an interior boundary is an interface which divides two domains in the geometry. Details of model set-up, geometry, meshing, and solver were discussed in the supplementary information file. The arrangement of a thin-film capacitor is illustrated in Fig. 4.6, where the direction of current and the resulting electric field is shown. At the lower plate, electrons will accumulate and thus becomes negatively charged. It will form an electric field between the plates directed from positive towards negative.
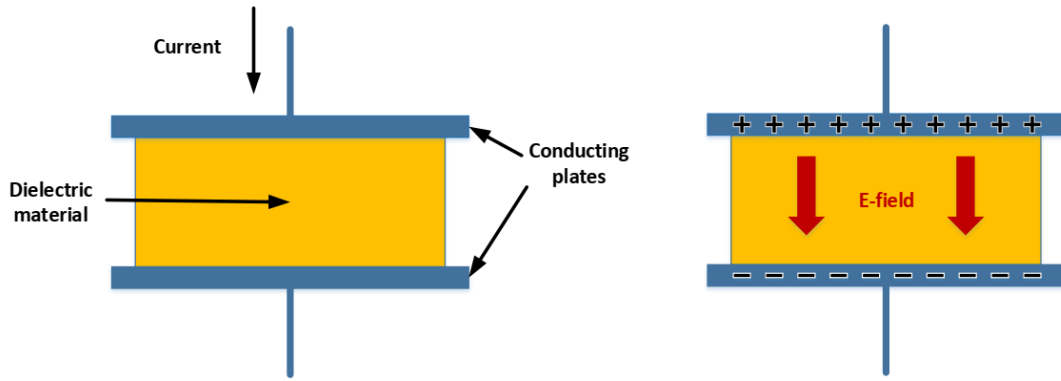
Figure 4.6 Schematic of a parallel-plate capacitor of two conductive plates separated by a dielectric, the direction of current, electric field formation, and accumulation of charges on the plates are shown.

4.4.2 Model equations

There are three model equations in the study of the interaction of electric charges and currents. Gauss's law (Eq. 4.1) in free space defining the interaction between the divergence of the electric field and the charge density. Ohm's law (Eq. 4.2) specifying that the current density is proportional to the electric field by the factor and the continuity equation (Eq. 4.3). The equations are given as follows

$$\nabla \cdot E = \frac{\rho}{\varepsilon_0} \tag{4.1}$$

$$J = \sigma E \tag{4.2}$$

$$\nabla \cdot J = -\frac{\partial \rho}{\partial t} \tag{4.3}$$

where E is the electric field vector in V/m, ρ is the total charge density in C/m^3, ε_0 is the constant of free space 8.85×10^{-12} in F/m, J is the electric current density vector in A/m^2 and, σ is a proportionality factor called conductivity of a medium in S/m.

The charges can be shifted from their original position if the PVDF-HFP/LZO dielectric is placed in an electric field. It leads to induce dipole moments that allow the dipoles to

align in the same direction. Different types of polarization occur in PVDF-HFP/LZO dielectrics, including atomic electronic, dipolar (orientational), and interfacial polarization. Such mechanisms eventually lead to accumulations of charges within the PVDF-HFP/LZO dielectric defined by a volume charge density as in Eq. 4.4 (Maxwell constituent equation)

$$\nabla \cdot P = \frac{\overrightarrow{dp}}{dv} \tag{4.4}$$

$\nabla \cdot P$ is the divergence of polarization, dp is the differential electric dipole moment, dv is the differential volume. The entire surface of each electrode is at the same potential. Capacitor plates have equal and opposite voltages that the boundary on the box is at zero potential.

4.4.3 Boundary conditions

The electric shielding boundary node is said to model a thin conductive layer and reduces the number of mesh components by approximating a thin layer. The thickness of the layer, relative permittivity, and AC conductivity is given to the node. The following Eq. 4.5 at this moment be applied at the boundary

$$n \cdot (J_1 - J_2) = -\nabla_t (d\sigma + j\omega\varepsilon_{rs})\nabla_t \varphi \tag{4.5}$$

$$n \cdot J = 0 \tag{4.6}$$

where n is the normal vector, ∇_t is the tangential gradient, d is the thickness of the conductive layer, σ is the conductivity of the layer, ε_{rs} is the relative permittivity of the layer, $j\omega$ is the displacement current, φ is the electric potential.

Eq. 4.6 defines that there are no electric current flows through the PVDF-HFP/LZO dielectric layer. Once the boundary conditions are selected, a meshing sequence is applied. It enables the discretization of the geometry into small units. A solver provided in COMSOL solves the model by using the finite element method. The model output is discussed in the results and discussion section.

4.5 EXPERIMENTAL METHOD

4.5.1 Preparation of composite ink

PVDF-HFP pellets were dissolved in 50 ml of N, N-Dimethylformamide (DMF) using a magnetic stirrer for 20 min. LZO solution was prepared by dissolving 3g of LZO powder in 10 ml of distilled water (Sigma-Aldrich)/5 ml of acetic acid (CH_3COOH, 99.8%, Merck)/5 ml of triethanolamine ($N(CH_2CH_2OH)_3$, 99.9%, Merck) system. Triethanolamine and acetic acid are water-based solutions that may help to minimize the formation of non-specific complexes. LZO powder dispersed in these solvents and subjected to sonication for 15 min to form LZO colloidal solution. High-intensity ultrasonication helps to form a nano colloidal solution from LZO powder. LZO solution was taken in 15 vol% and mixed with PVDF-HFP solution by vigorous stirring for 15 min. After complete dissolution, the solution was subjected to sonication using a probe-type sonicator (SONICS Vibra cell with a 500W ultrasonic processor and 13.2 mm diameter probe). 20 kHz frequency with a 500-watt ultrasonic generator was used. The sonicator was operated at a pulsed mode (ON/OFF ratio of 4s/2s) at a 40% power amplitude for 30 min. The maximum temperature of the solution reached during sonication was 70 °C. After 30 minutes, the product solution is collected in a container and directly spin-coated to form thin-film. The composite ink found to be a milky white with no suspended particles. It gives clear evidence of the stability of the solution derived from the sonochemical technique.

4.5.2. Thin-film deposition

A well-dispersed LZO/PVDF-HFP solution was directly spin-coated on ITO/SiO_2 without any further processing. The composite ink is spin-coated (3000 rpm for 30 s with 10 s ramp-up timing) on to the ITO coated glass (resistance: 15Ω, make: Luminescence Technology Corp.), which acts as the bottom gate electrode for the capacitor. The spin-coated film then annealed at 100 °C for 1 min and then the second layer is deposited with same spin coating parameters which were then followed by a post-annealing at 70 °C for 2 h on a hot plate and cooled down to room temperature just

by turning off the hot plate. Neat LZO film is fabricated by spin-coating LZO colloidal solution (3500 rpm for 30 s with 15 s ramp up timing) on to the ITO coated glass. The spin-coated film then annealed at 200 °C for 1 min and then the second layer is deposited with the same spin coating parameters, which were then followed by a post-annealing at 100 °C for 2 h on a hot plate and cooled down to room temperature. Further top contacts were made using thermally evaporated copper (Cu, purity - 99.9999%, Alfa Aesar pure) pads (area: 1 mm × 2 mm). A schematic of composite ink preparation and device fabrication is shown in Fig. 4.7.
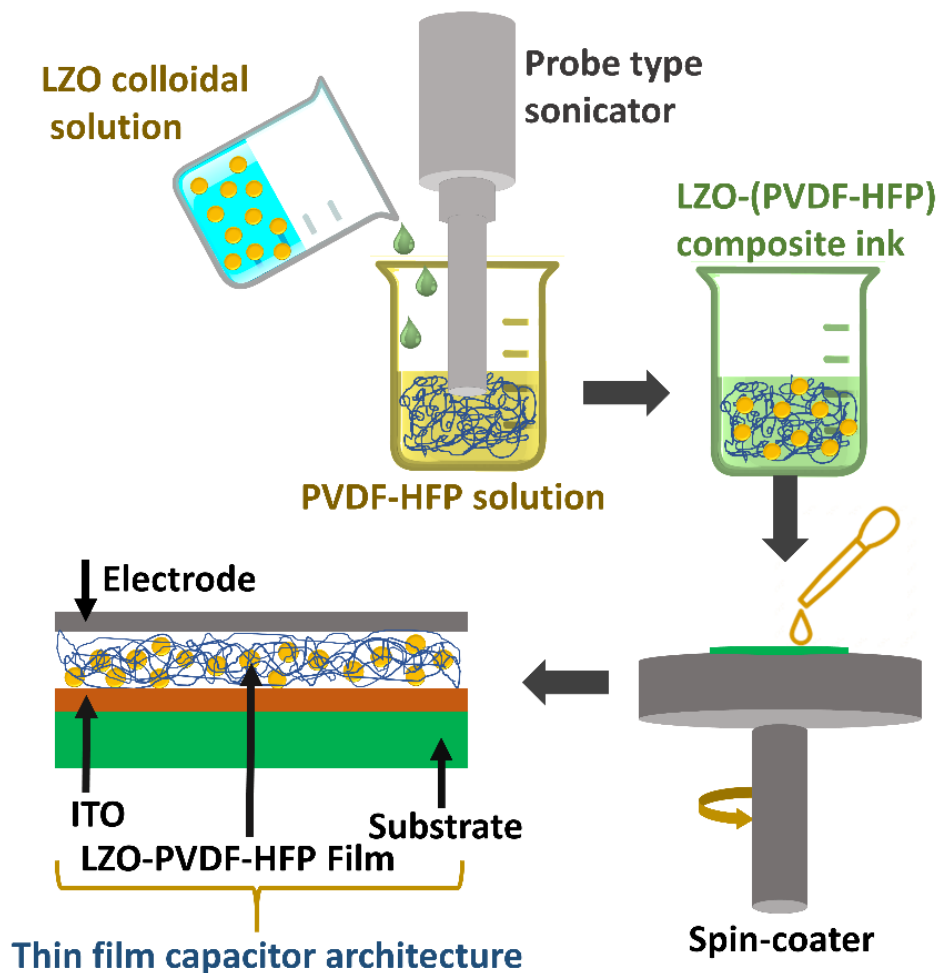

Figure 4.7 Schematic of steps involved in PVDF-HFP/LZO composite ink preparation and thin-film fabrication process.

4.5.3 Characterization

PVDF-HFP/LZO film capacitor was subjected to the impedance analysis (IM3536, Hioki, Japan) to determine the dielectric permittivity, loss tangent at different frequencies in the range of 10 Hz to 1 MHz. All impedance measurements were made at room temperature using bias voltage -1 to +1. Energy storage density and breakdown strength were determined by the ferroelectric workstation (Radiant, Inc.). XRD pattern was recorded by Bruker D8 Advance X-ray powder diffractometer using Cu-Kα radiation (40 kV, 40 mA) (wavelength λ=1.5406 Å). Film thickness and surface morphology were measured using SEM (JEOL JSM 6400). Cryo-Electron Microscopy was used to capture PVDF-HFP/LZO composite ink in freeze-fracture mode. Cryo-electron microscopy facility has a 200 kV Talos-Arctica electron microscope (FEI/Thermo Scientific) equipped with Gatan K2 Summit Direct Electron Detector. Computational modeling was carried out in COMSOL Multiphysics using the finite element method (FEM).

4.6 RESULTS AND DISCUSSION

4.6.1 Crystallinity, morphology, and chemical structure analysis

X-ray diffraction (XRD) patterns of PVDF-HFP, LZO, PVDF-HFP/15 vol% LZO are presented in Fig. 4.8a without smoothening of the plot. Hereafter, PVDF-HFP/15vol% LZO is named PVDF-HFP/LZO15. The peak at 18.4° and 20.8° corresponds to alpha (α) and beta (β) phase, respectively, a broad peak at 26.6° and 38.8° corresponds to the gamma (γ) phase of PVDF-HFP. XRD of PVDF-HFP shows the typical semi-crystalline nature. Since LZO is not calcined at high temperature, we did not observe sharp crystalline peaks. However, the broad peaks at 12.3°, 28.2°, 33.2°, 47.6°, and 56.6° confirm the LZO cubic pyrochlore phase (ICSD-15475). XRD pattern of PVDF-HFP/LZO15 displays the combined peaks of LZO and PVDF-HFP, which indicates the presence of both LZO particles and PVDF-HFP in the composite film.
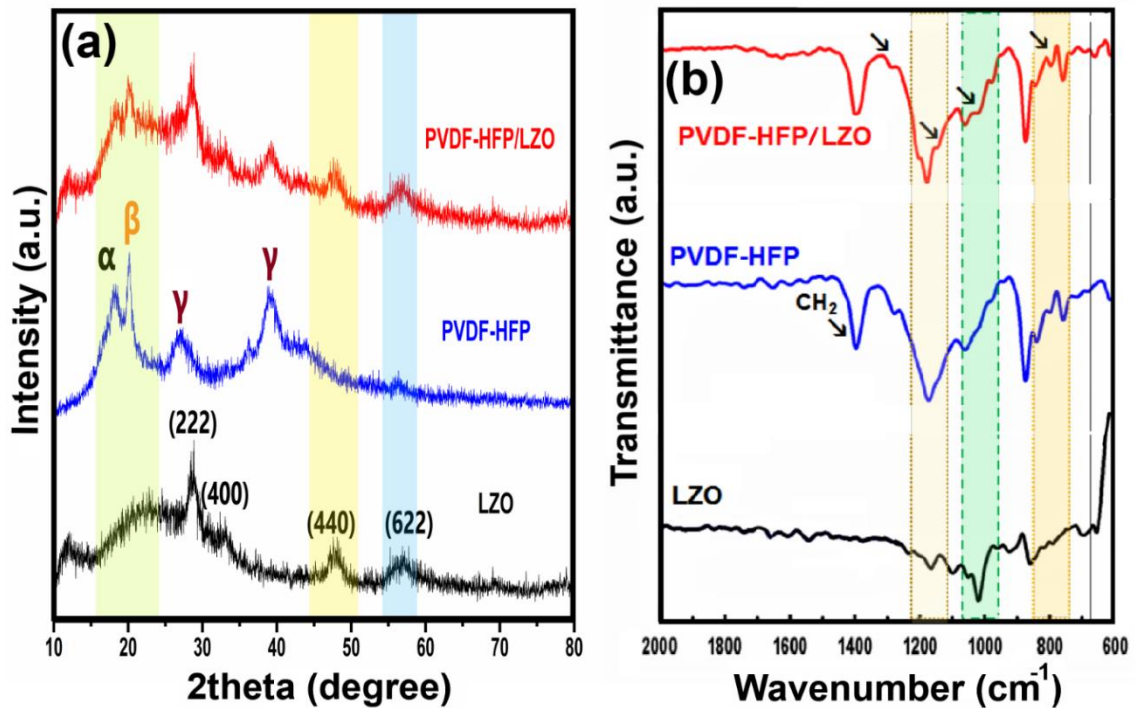
Figure 4.8 (a) XRD pattern and (b) FTIR spectra of LZO, PVDF-HFP, and PVDF-HFP/LZO15 composites.

Fourier-transform infrared spectroscopy (FTIR) analysis is performed in the range of 600-2000 cm^{-1}, as shown in Fig. 4.8b. FTIR spectra of PVDF-HFP and PVDF-HFP/LZO15 composite exhibit the typical absorption peaks of α- phase, β-phase, and γ-phase of PVDF-HFP at around 615 cm^{-1}, 730 cm^{-1} and 890 cm^{-1}, which indicate that the crystalline type of the composites is almost the same as the PVDF. The bending of C-C-C is observed at 1070 cm^{-1}, while the peak of CH_2 appears at 1400 cm^{-1}. Meanwhile, no peak of hydrogen bonds can be detected in neat PVDF-HFP. In the spectra of PVDF-HFP/LZO15 composites, the absorption peaks range from 1000 cm^{-1} to 1200 cm^{-1} are attributed to the hydroxyl stretching vibration, which suggests that the strong hydrogen bonds are formed between the hydroxyl groups of LZO fillers and fluoride atoms of PVDF-HFP. The reduction of hydroxyl vibration energy suggests the formation of more stable hydrogen bonds.
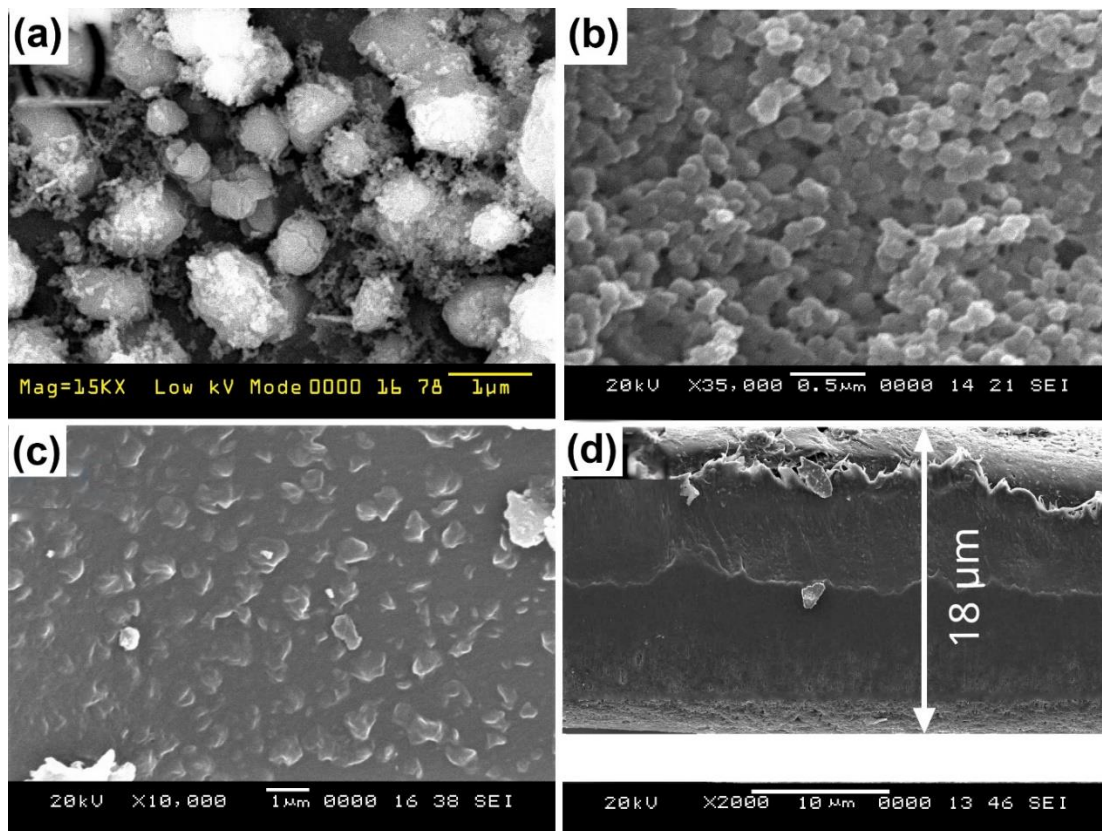
Figure 4.9 (a) Cryo-electron microscopy image of PVDF-HFP/LZO composite ink prepared by the sonochemical approach. SEM images of (b) Neat LZO colloidal particles (c) PVDF-HFP/LZO15 composite film deposited via spin coating annealed at 70 °C (d) Cross-sectional view of the composite film and thickness of the film is-18 µm after two layers of spin-coating.

The cryo-EM image soon after preparing PVDF-HFP/LZO15 composite ink (the liquid form of the sample) in freeze-fracture mode was ~~is~~ captured. The spherical structures could be PVDF-HFP polymer spheres surrounded by LZO colloidal particles in the nanometre-scale, as shown in Fig. 4.9a. SEM images of LZO particles were in nanoscale and spin-coated PVDF-HFP/LZO15 composite film shown in Fig. 4.9b&c, respectively. 15 vol% of LZO particles are distributed uniformly in the PVDF-HFP matrix after annealing at 70 °C for 2 h. LZO dielectric ink containing LZO colloidal particles are mixed with PVDF-HFP polymer solution using ultrasonication. The thickness of the composite film after two layers of spin-coating is 18 µm calculated using an SEM cross-sectional view of the film, as shown in Fig. 4.9d.

Table 4.3: Dielectric properties of fabricated films obtained by the impedance analysis used as input in simulations to compute the energy storage density and breakdown strength of LZO/PVDF-HFP composite films with different LZO content.

Material	Dielectric permittivity (ε_r)	Breakdown strength (E_b)
LZO	26	6.2 MV/m
PVDF-HFP	11	659 MV/m
15LZO/PVDF-HFP	21	545 MV/m

4.6.2 Dielectric Properties

In general, the energy storage density of dielectric capacitors is determined by the integral from Eq. 4.7:

$$U = \int_{D_{max}}^{0} E \, dD \qquad (4.7)$$

where E is the electric field, and D is the electric displacement, and for linear dielectrics, the energy storage density can be defined from the Eq. 4.8:

$$U = \frac{1}{2} \varepsilon_0 \varepsilon_r E_b^2 \qquad (4.8)$$

where U is the energy storage density, ε_0 is the dielectric permittivity of free space, ε_r is the dielectric permittivity of the composite, and E_b is the breakdown strength. The energy storage density of a composite is determined by the field that can be applied to the capacitor, which is constrained by the film's dielectric breakdown (E_b) strength. Thus, to increase the energy density of the capacitor, it is critically important to develop low-loss electroactive materials with high dielectric permittivity and high breakdown strength. From previous studies (Dang et al., 2013); (Chen et al., 2018), with the addition of a high-k filler to the polymer matrix despite the increase in the dielectric permittivity of the polymer composites, there is also a reduction in the breakdown strength which results in a lower energy density compared to the neat polymer matrix.

Hence, our primary goal is to find the optimum volume fraction of LZO in PVDF-HFP from computational modeling to achieve high energy storage density without compromising much in breakdown strength. Table 4.3 shows the material parameters obtained by the impedance analysis, which are used as inputs in simulations to calculate energy storage density and breakdown strength of LZO/PVDF-HFP composite film. The computed energy storage density for LZO/PVDF-HFP dielectric capacitor with different volume fraction (5, 10, 15, 20, 30 vol%) of LZO colloidal particles is shown in Fig. 4.10a. The energy storage density of the composite film increases from 8.9 to 19.0 J/cm^3 with a corresponding change in LZO vol% from 5 to 20% as excepted due to the high energy density of LZO (20.6 J/cm^3). PVDF-HFP/LZO30 film shows a storage density of 14.8 J/cm^3 at 233 MV/m because of lower breakdown strength.

However, these composite films fabricated with different vol% of LZO breaks at a particular applied electric field called breakdown strength. Computational modeling is carried out along with energy storage density using the Weibull distribution function to study the breakdown strength phenomena. The breakdown strength of composite films increases initially at lower LZO content in PVDF-HFP but ultimately drops to lower values at very high LZO contents shown in Fig. 4.10b. Initially, the breakdown strength increases from 680 MV/m at 5 vol% to 710 MV/m at 10 vol% due to stronger interaction of LZO particle surface with PVDF-HFP chains and redistribution of an electric field within the polymer matrix (Rahimabady et al., 2013b). However, it drops from 420 MV/m to 233 MV/m when the volume fraction of LZO changes from 20 to 30 vol%. A possible reason for decrease (at 30% LZO) could be the formation of percolation path, unusual distribution of electric field among LZO particles, and the creation of air voids in composites. In our model, only the number of LZO particles distributed in the given area of the PVDF-HFP matrix was considered. However, from the previous work done by Kim et al. (2009) developed a model to calculate the dielectric permittivity and breakdown strength using statistical particle packing simulations and effective medium theory. They discussed the important roles of nanoparticle percolation and porosity of the nanocomposites on the dielectric properties. From their observation "the effective permittivity is decreased with increasing nanoparticle volume fraction (>40%), due to an increase in porosity and air

voids of the spin-coated nanocomposite films*",* this might be the possible reason for the abrupt decrease in the breakdown strength of the 30LZO/PVDF-HFP composite film.

The computational modeling shows that PVDF-HFP/LZO15 has better energy storage density (16.5 J/cm^3) with a breakdown strength of 530 MV/m. To validate the computational results, 10%, 15%, and 20 vol% LZO in PVDF-HFP composite film, neat LZO film, and neat PVDF-HFP film was fabricated. Further, dielectric permittivity, dielectric loss, energy storage density, and breakdown strength were obtained. The frequency-dependent dielectric permittivity and dielectric loss of the composite film were measured at room temperature. Dielectric permittivity (k) of LZO is found to be 26 and for neat PVDF-HFP ~11 at 1 kHz. PVDF-HFP/LZO15 film exhibits k~21 almost double as compared to that of neat PVDF-HFP, whereas 10% and 20 vol% film show k~15 and k~22, respectively shown in Fig. 4.11a.
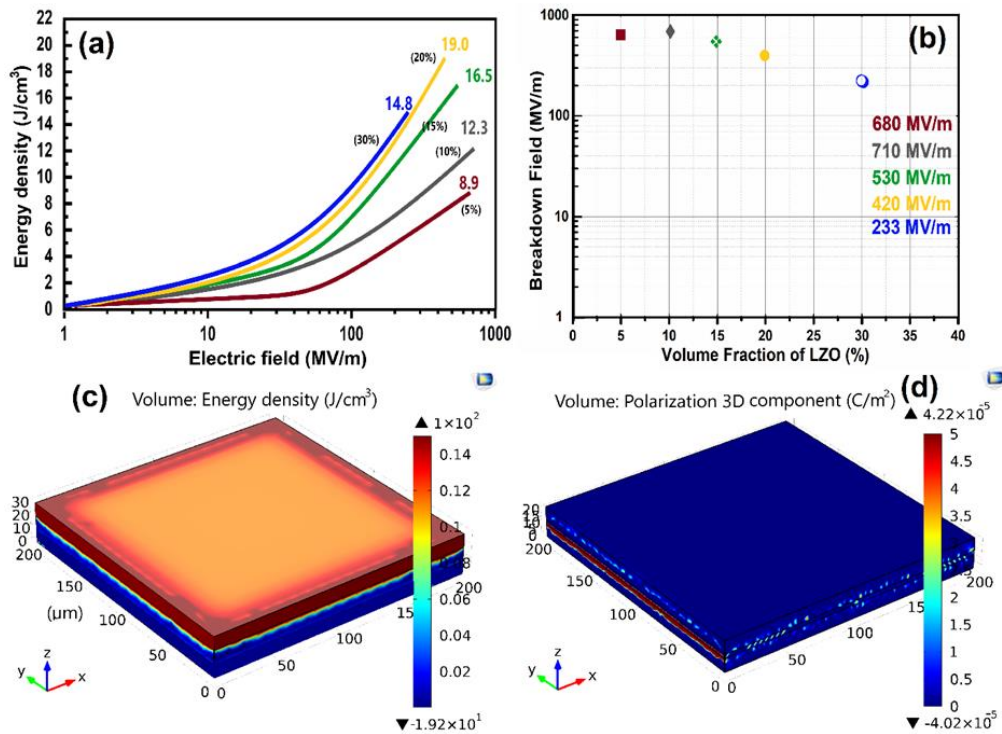

Figure 4.10 Computational model results: (a) Energy density of PVDF-HFP/LZO composite films with the different volume fraction of LZO (5-30%) as a function of the applied electric field (b) Breakdown strength of the composite films with different LZO

contents (c) Energy storage density and (d) Polarization of a PVDF-HFP/LZO thin-film capacitor 3D model.

The possible reason for this high dielectric permittivity is the accumulation of charges at the interface between the PVDF-HFP and LZO dielectric medium. Such charge accumulation at the interfaces causes interfacial polarization. The interfacial polarization, also known as the Maxwell–Wagner–Sillars (MWS) effect, is responsible for a significant increase in low-frequency permittivity (Nan et al., 2010). The substantial increase in the intensity of the local electric field contributes to the migration and accumulation of charge carriers at filler-matrix interfaces. These charges are generated by either the surface plasma resonance or the charge injection from the external electrodes, depending on the relaxation time of the two phases. Hence, the MWS effect is more significant in polymer composite dielectrics. The MWS polarization arises once the current, including the dipole reorientation component, passes across materials with electrical inhomogeneity. The bonded charges accumulate at the interfaces of two distinct dielectric mediums. In the measured range of 10 Hz-10 MHz, the dielectric permittivity gradually declines at a higher frequency for all the three samples due to a decrease in dipolar orientation polarization.

The dielectric loss (tan δ) of LZO is 0.328, which is much higher than the PVDF-HFP/LZO15 composite film (tan δ~0.12) shown in Fig. 4.11b. Tan δ of neat PVDF-HFP is around 0.028 and reached up to 0.12 when 15 vol% of LZO is incorporated. 20 vol% film shows nearly 0.15. An increase in the dielectric loss above 20 kHz frequency range is attributed to interfacial polarization of the PVDF-HFP/LZO dielectric interface and reorientation of dipoles of the crystalline phase in PVDF. The polar interaction between the positive space charges in LZO with the electronegative fluorine in the CF_3 group of PVDF-HFP. This particular interaction is frequency-dependent and cannot shift in the polarity at a higher frequency range; hence, the increased dielectric loss of PVDF-HFP/LZO film was observed. High-k value of PVDF-HFP/LZO composite by increasing LZO content could be achieved. However, the increase in filler content makes film brittle and decreases the breakdown strength of PVDF-HFP film.

A simple model is proposed (Tian et al., 2015)) based on the space-charge effect in PVDF-based MFM capacitors and inorganic oxide-based capacitors. According to the model, the space-charge mechanism can be considered as an interfacial effect and treated electrostatically when mobile charges trapped by defect sites are released and occupies more positive space charges in the high-k oxide films such as $LaTiO_3$, $La_2Zr_2O_7$, $BaTiO_3$. Due to the Fermi level difference between LZO and PVDF-HFP, LZO occupies positive charges, while negative charges accumulated at the polymer due to the presence of electronegative fluorine in P(VDF-HFP). The characteristic dielectric breakdown strength (E_b) of the PVDF-HFP/LZO composites is analyzed using a two-parameter Weibull distribution function (Eq. 4.9)

$$P(E) = 1 - exp(-(E/E_b)^\beta) \qquad (4.9)$$

where $P(E)$ is the cumulative probability of dielectric failure, E is experimental breakdown strength, E_b is a scale parameter defines the breakdown strength at 63.2% probability for the film to breakdown, and β is the Weibull modulus related with the linear regressive fit of the distribution (Shen et al., 2016). E_b of LZO and neat PVDF-HFP are measured to be 6.2 and 659 MV/m, respectively. E_b of PVDF-HFP/LZO15 composite film is 545 MV/m, is shown in Fig. 4.11c. The computational model found that E_b of 15 vol% of LZO composite film is 530 MV/m is a good agreement with experimental data. The high E_b of these films implies that the movement of electrons is restricted, and the free charges available at the interface move difficulty in the PVDF-HFP and PVDF-HFP/LZO composite when an electric field is applied.

To explain the energy storage mechanism in the composite film, the electric field formation in the PVDF-HFP matrix is essential as per the Eq. 4.7. the electric field with no LZO content and with a different volume fraction of LZO (5, 10, 15, 20, 30 vol%) in the PVDF-HFP matrix by electrostatic capacitor model shown in Fig. 4.12 (a-f). Electric field distribution is almost even with negative and positive terminal ends when there is no LZO in PVDF-HFP. As 5 vol% of LZO is introduced into the matrix, the free electrons from LZO accelerated by the applied electric field will be attracted/scattered due to Coulomb force and show higher electric filed about 0.19 MV/m. Additionally, if the volume fraction of the LZO reaches a certain high level, conductive pathways could be formed as the interfacial regions around the adjacent

83

LZO particles overlap. Also, the LZO particles lose their energy as they collide each other resulting in a rapid rise in the electric field up to 0.3 MV/m at 30 vol%.

In order to visualize the energy storage density and polarization phenomena, PVDF-HFP/LZO thin-film capacitor is built with a top and bottom electrode. The computational result exhibits the electric charge storage on the capacitor plates shown in Fig. 4.10d. When current passes through the capacitor circuit, charges separate themselves leading to create an electric field between the plates. Apparently, the top electrode becomes positively charged (red color), and the bottom electrode negatively charged (blue color) indicated in color gradients shown in Fig. 4.10c. Charge separation based on the polarity can also be observed in a dielectric layer from the color gradient. The average value of energy density from the simulation is 16.5 J/cm^3, comparable to the experimental value of 15.8 J/cm^3 shown in Fig. 4.11d. The energy storage density of neat PVDF-HFP is improved from 7.7 J/cm^3 to 15.8 J/cm^3 nearly by two times when 15 vol% of LZO is incorporated. 10% LZO shows a better breakdown strength of 653 MV/m with 11.7 J/cm^3 energy storage density. However, the energy storage density of 15% LZO composite film exhibits a much higher value of 15.8 J/cm^3 at breakdown strength of 545 MV/m because of an increase in dielectric permittivity to the rapid polarization formation among LZO particles. Thus, 15% LZO/PVDF-HFP composite film is optimized in terms of energy storage density.

Both experiments and simulations results suggest that 15% of LZO content is optimal. Energy storage density and breakdown strength of the 10%, 15%, and 20% LZO/PVDF-HFP films are shown in Fig. 4.11c&d. Our result could be compared with previous work of PVDF/BaTiO$_3$ composites with a high energy density of 13 J/cm^3 at 500 MV/m for reported by Zhang et al. (2015). For P(VDF-HFP)-BT@TiO$_2$ core-shell nanocomposites, the highest reported value of energy density is 12.2 J/cm^3 at 340 MV/m. The reason for improved energy storage could be the combination of increased dielectric polarization and high breakdown strength. The polarization density in the Eq. 4.4 in the electrostatic model was computed to understand the polarization behavior in a thin-film capacitor. Dipole moments in the dielectric layer could be equally distributed, so the same and uniform polarization is witnessed around the dielectric layer. Besides, the large interfacial areas in the composite between the PVDF-HFP and

the LZO particle could also facilitate the exchange coupling effect (confirmed from FITR spectra Fig. 4.8b) via dipolar interface layer, offering higher polarization levels, dielectric response, and breakdown strength. However, the negative activation energy indicates that a large number of electrons are possibly present at the interface of the PVDF-HFP/LZO composites, which results in intense interfacial polarization.
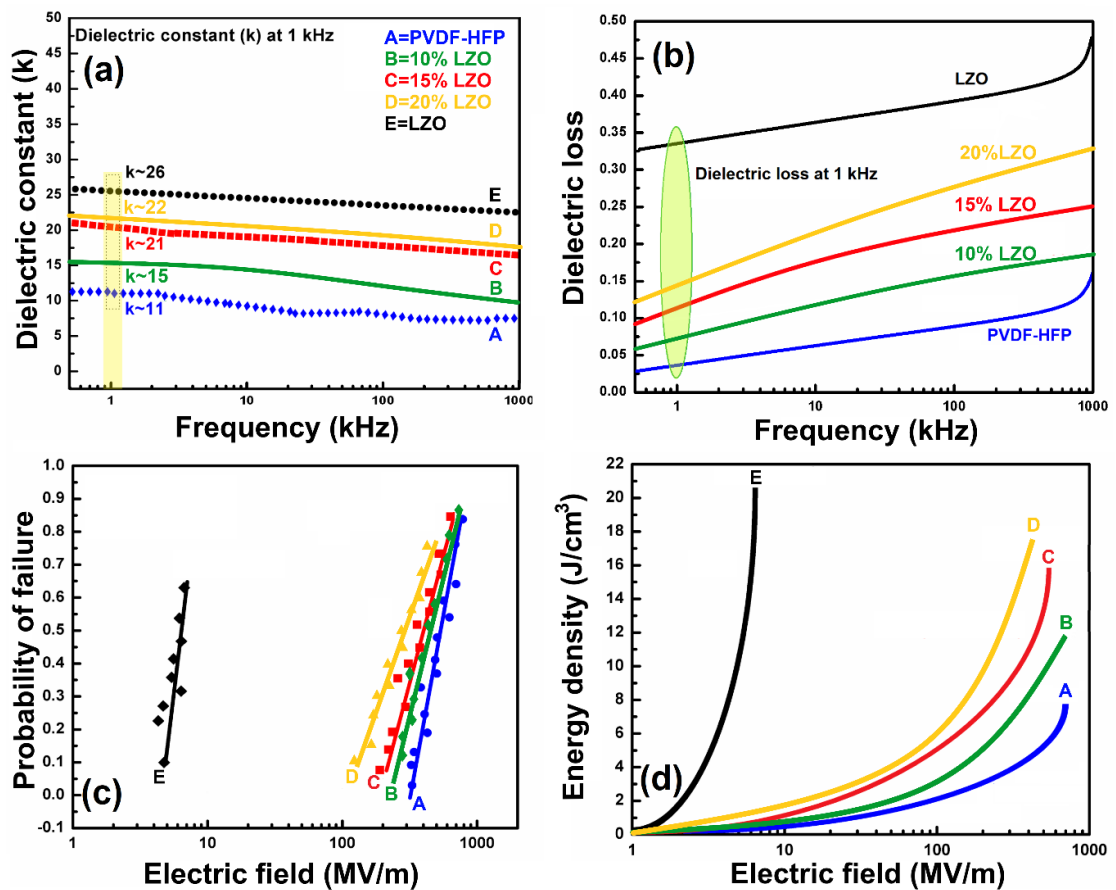
Figure 4.11 Frequency-dependent (a) Dielectric permittivity and (b) Dielectric loss of the composite film measured in the range of 10Hz-1MHz at room temperature (c) Breakdown strength is calculated using a probability of failure vs. the electric field (d) Energy storage density vs. electric field of LZO, PVDF-HFP, and 10%, 15%, and 20% LZO/PVDF-HFP composite films.
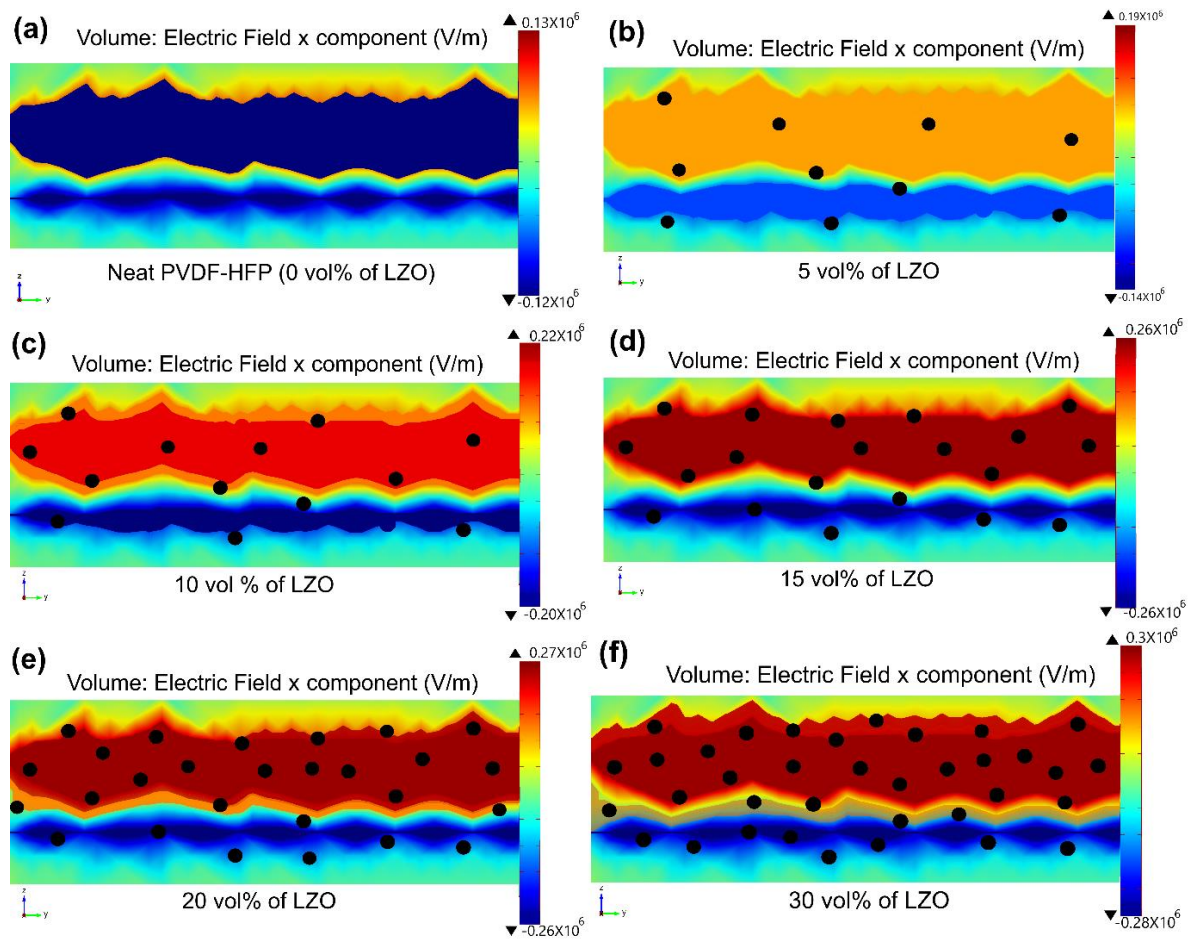
Figure 4.12 Electric field formation in (a) PVDF-HFP matrix without LZO particles (b) 5 vol% of LZO (c) 10 vol% of LZO (d) 15 vol% of LZO (e) 20 vol% of LZO (f) 30 vol% of LZO in PVDF-HFP matrix. The top portion of the layer is connected to the positive terminal, and the bottom one is grounded.

The improvement of dielectric properties in PVDF-HFP/LZO composites is attributed to the enhancement of interfacial polarization, large interface area, and uniform distribution of LZO particles. Recently, the ultra-high dielectric permittivity for $La_{1.5}Sr_{0.5}NiO_4$/PVDF composites was obtained due to interfacial polarization arising from a large interfacial area of nano-size filler and shorter interparticle distance (Meeporn and Thongbai, 2020).

The experimental results with model predicted values of LZO/PVDF-HFP composite films for energy storage density and breakdown strength were compared. It is considered 15% LZO/PVDF-HFP composite film is optimal concerning energy storage density, dielectric loss, and breakdown strength. From Table 4.4, it can be observed that LZO/PVDF-HFP composite film properties are comparable with that of model-predicted values.

Table 4.4: Comparison of model-predicted values and experimental results of PVDF-HFP composite films with different LZO content

LZO content (%)	Energy storage density (J/cm^3)		Breakdown strength (MV/m)	
	Model predicted	Experimental	Model predicted	Experimental
5	8.9	---	680	---
10	12.3	11.7	710	653
15	16.5	15.8	530	545
20	19.0	17.9	420	398
30	14.8	---	233	---

4.7 SUMMARY

PVDF-HFP/LZO based composite dielectric ink was prepared by the sonochemical approach at low temperature, and both computational modeling and experiments assessed the dielectric performance of the composites. The interfacial interaction between LZO particles and the PVDF-HFP polymer phase is improved in solution-processed composite ink, which is highly favorable to achieve better dielectric properties. The effect of LZO content on the dielectric properties of the polymer composite film was studied. The model results confirmed a significant improvement in dielectric constant and energy storage density and an acceptable drop in breakdown

strength with increasing LZO content. Limited experimental data validated the results of the computational model. PVDF-HFP/LZO15 was found to be having a better energy storage density of 16.5 J/cm^3 at 530 MV/m with low dielectric loss. Computational modeling helps us avoid waste of material and optimize the filler content in composites to achieve the most desirable dielectric properties of the composites. The present findings suggest that the modeling approach can be used to model thin-film capacitors with polymer composite as a dielectric layer to estimate the energy density. Also, one can design a thin-film capacitor of interest with a different combination of inorganic/polymer composite dielectrics for functional electronic devices using computational modeling. The dielectric performance of PVDF-HFP/LZO composites suggests that capacitors fabricated from the composite ink of PVDF-HFP/LZO could be operated at high voltages.

CHAPTER 5

FABRICATION OF PATCHY PARTICLES AND DUMBBELL SHAPED JANUS STRUCTURES

5. 1 INTRODUCTION

Anisotropic particles like patchy, Janus, and composite particles have gained attention in the field of material science due to their unique morphologies and potential applications. Every patchy and Janus particle's essential characteristic is anisotropy with chemically or morphologically different structures in nature. Accessibility of at least two unique materials in a single unit would allow various physical or chemical functionalities (Walther et al., 2009). Combinations of getting patchy/Janus particles include either organic or inorganic or hybrid organic-inorganic compounds. It is shown that as the size of patchy particles decreases to the nanoscale, large interfacial areas between core and patches would facilitate the effect of exchange coupling via the dipolar interface layer, providing higher polarization levels, dielectric response, and breakdown strength. (Pawar and Kretzschmar, 2009) classified patchy particle fabrication as follows in their review article: (a) templating, (b) colloidal assembly, (c) glancing-angle deposition, (d) particle lithography, (e) nanosphere lithography, (f) electrospray using a biphasic nozzle, (g) anisotropic self-assembly of polymer-grafted spherical nanoparticles (Zhang et al., 2014). Another exciting technique, called the Pickering emulsion route, was recently introduced to prepare patchy particles (Luo et al., 2019).

Zang and Glotzer introduced the word patchy particle in 2004. They proposed a simplified model capable of simulating patchy particles with a different shape and size. This model presents the relationship between interaction among particles, particle shape, and the self-assembly of target structures with few numbers of particles. Their findings indicated how accurately patch arrangements associated with patch

"identification" or "selectivity" that can be used to regulate the relative position of particles within a structure and thus influence the overall configuration of particle structures. Theoretical models for patchy particles with a pair of potential, particles with differentiable patches and core particles, protein interactions, and anisotropic interactions between particles were reported (Zhang and Glotzer, 2004). Patchy and Janus particles can be utilized as artificial atoms for building a new material not only by combining their shape and size but also taking advantage of their electromagnetic interactions. A recent study on emulsion polymerization of styrene in the presence of nanogel as a stabilizer to form patchy microspheres is reported. They showed that one could tailor the patch positions by varying the pH of the polymer solution (Lotierzo et al., 2018).

Although the approaches used in the models differ, the aim is to understand the interactions between particles, phase transitions, and predicting the structural phase diagrams for patchy particles. The above discussion is an advancement in modeling and fabrication of anisotropic patchy particles with specific geometries and topologies. Peng et al., (2019) reported a new way to detect local polarization properties in ferroelectric nanocomposites at the matrix/filler interface using Kelvin probe force microscopy. They found that the dielectric permittivity of the interfacial region within the measured voltage range is ~17% greater than that of the matrix. Improved dielectric permittivity of the interfacial region implies that the polarization under the identical applied electrical fields is strong, i.e., the electric field can lead to greater induced dipole moment in the interface than in the matrix. The unusual performance of dielectric nanocomposites is believed to originate from the interfacial region between the core (polymer) and patches (nanoparticles). In principle, their dielectric behavior differs from that of the nanofiller inclusions or the polymer matrix in interfacial regions, as it could be attributed to additional interfacial polarization.

The use of patchy and Janus particles as dielectric materials remains challenging due to a lack of understanding of patch-core interaction and interface behavior of chemically two different metal oxides in an applied electric field, respectively. Therefore, there has been no considerable progress in correlating the local electric field

and polarization in the interfacial region with the unusual performance of bulk materials in patchy and Janus dielectric materials. Information on polarization and electric field formation in patchy and Janus particles are needed to design high-performance dielectric materials for functional electronic devices.

This chapter discusses the effect of the interface or the contact points of the PS-Fe_3O_4 particles and La_2O_3-ZrO_2 Janus particles on the dielectric properties, mainly polarization and electric field formation. Dielectric responses of PS-Fe_3O_4 patchy microspheres such as polarization and electric field formation in an applied electric field are reported. From the Maxwell constituent equation (Eq. 5.1), the dielectric permittivity of a material (ε_r) can be calculated with a function of dielectric polarization (P) and electric field (E).

$$\varepsilon_r = 1 + \frac{P}{\varepsilon_o E} \tag{5.1}$$

where ε_o is the permittivity of vacuum, dielectric permittivity (ε_r) values of PS-Fe_3O_4 patchy microspheres were calculated from Eq. 5.1. Dielectric response data of neat PS and Fe_3O_4 obtained from the impedance analyzer were used in the 2D electrostatic computational model and simulations. The dielectric permittivity values of PS Fe_3O_4 patchy microspheres obtained by the impedance analysis and simulations of the computational model were compared. The models are used to analyze the dielectric behavior of neat Fe_3O_4 and neat PS spheres. A new charge build-up mechanism at the patchy interface based on experimental outcomes and computational simulations is proposed. The advantage of using patchy particles is that the inorganic patches would not cover the entire surface of the polymer (core). Therefore, no control over the distribution of the electrical field around the surface is required. Although the permittivity mismatch occurs in patchy particles, the interface accumulates and distributes the charge through the patches. Computer simulations predict that patchy particles with well-defined interactions can self-assemble into ordered and disordered phases to improve dielectric properties (Chen et al., 2004). Another advantage of preparing films using patchy spheres is that the dispersion issues can be overcome compared to when composites are prepared commonly by dispersing nanoparticles in the polymer.

5.2 EXPERIMENTAL METHOD

5.2.1 Materials

Ferric chloride (FeCl$_3$, 99.999%), Ferrous chloride (FeCl$_2$, 99.999%), Ammonium hydroxide (NH$_4$OH, analytical grade), Oleic acid, (99% GC grade). Azobisisobutyronitrile (AIBN, 98%, Free radical initiator), Styrene (Monomer grade with 99.9% purity). All chemicals were purchased from Sigma-Aldrich and used without any further purification.

5.2.2 Synthesis of Fe$_3$O$_4$ coated polystyrene patchy microspheres

PS-Fe$_3$O$_4$ patchy microspheres were synthesized based on the work reported by Kim et al., (2013) with a process modification. They carried out polymerization for 12 h, but we used ultrasonication to reduce the polymerization duration to 2 h. In this method, Fe$_3$O$_4$ particles with a range of 400-500 nm stabilize the styrene-in-water emulsion droplets by sturdy surface assimilation at the liquid-liquid interface. The formation of PS-Fe$_3$O$_4$ patchy spheres via the Pickering emulsion route is shown in Fig. 5.1. Pickering emulsions have higher stabilities against coalescence than the standard surfactant-stabilized emulsions due to the adsorbed particles behaving like a mechanical barrier. 80 mL of deionized water and 2g of Fe$_3$O$_4$ particles (~20 % vol/vol to the styrene) was mixed and sonicated for 15 min to form Fe$_3$O$_4$ dispersion. 10 mL of styrene was added to the Fe$_3$O$_4$ dispersion and agitated in a homogenizer until the styrene layer was well dispersed in the aqueous phase as emulsified droplets. The resulting emulsion poured into a 250 mL, 3-neck round-bottomed flask that was bubbled with nitrogen for 30 min. An aqueous AIBN (0.1 g of AIBN/5 mL of deionized water) was added to an emulsion and sonicated for 2 h. The sonicated product was dried in an oven for 4 h. Again, the product was kept overnight in a freezer at -28 °C and freeze-dried at -80 °C for two days to get PS-Fe$_3$O$_4$ patchy microspheres. The different steps involved in the fabrication of PS-Fe$_3$O$_4$ patchy microspheres are shown in Fig. 5.2.
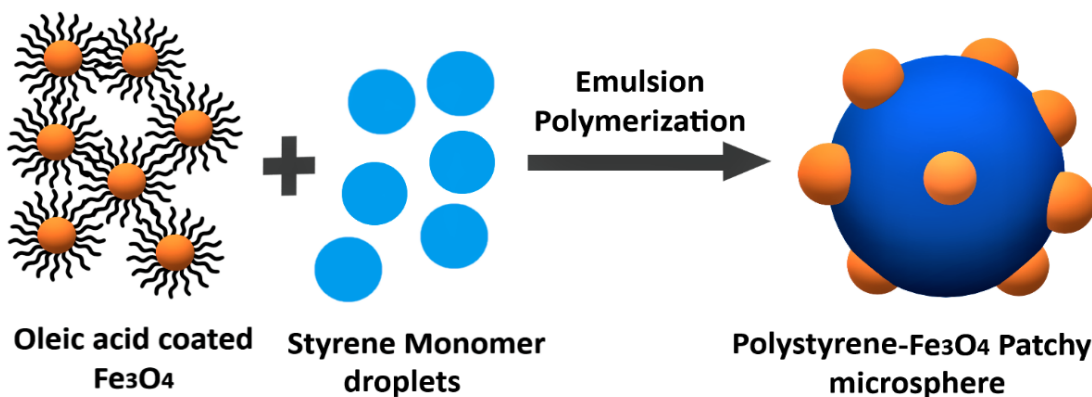
Figure 5.1 Schematic of PS-Fe$_3$O$_4$ patchy microsphere preparation via the Pickering emulsion route.
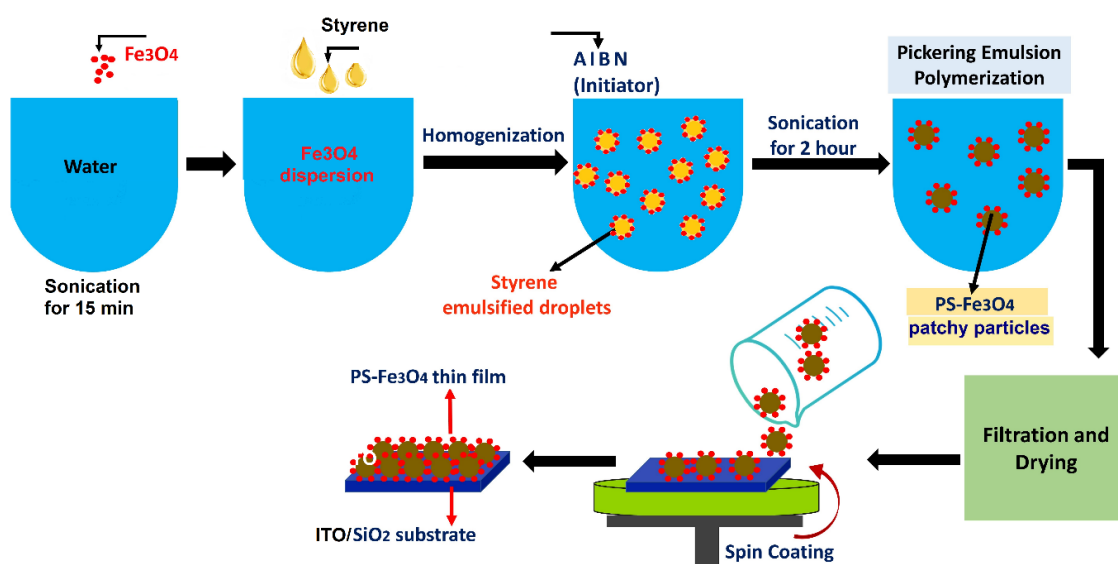
Figure 5.2 Different stages involved in the fabrication PS-Fe$_3$O$_4$ patchy microsphere and thin-film coating.

5.2.3 Characterization

Various techniques were used to characterize the PS-Fe$_3$O$_4$ patchy microspheres. Surface morphology and elemental analysis were done using scanning electron microscopy (SEM) on JEOL JSM 6400 attached with energy-dispersive X-ray spectroscopy (EDX). Images were taken at 20kV of accelerating voltage. The XRD pattern was recorded by Bruker D8 Advance X-ray powder diffractometer using Cu-

Kα radiation (40 kV, 40 mA) (wavelength $\lambda = 1.5406$ Å). Fourier transform infrared spectrophotometer (FTIR) (Perkin-Elmer, FTIR-100, UK) analysis was performed to determine the chemical structure. The spectra were taken in KBr pellets over the range $4000-400$ cm^{-1} in the deflection mode. Thermogravimetric analysis (TGA) (using TA instrument Q600) of dried powder was carried out by heating the powder samples under a nitrogen atmosphere from ambient temperature to 800 °C at a heating rate of 10 °C/min. For dielectric measurements, ITO/SiO$_2$ ($25\times25\times0.7$) mm^3 glass with a surface resistivity of 10 ohms/sq cleaned with acetone and treated in the ozone chamber for 40 s. PS-Fe$_3$O$_4$ patchy microsphere powder was dispersed in water/acetone (70/30) solvent mixture using a magnetic stirrer to make a coating solution. This solution was spin-coated on the ITO/SiO$_2$ substrate. The spinning speed with 1000 rpm for 15 s step up to 2500 rpm for 30 s with acceleration time 5 s was maintained using a vacuum-free spin coater (Navson-NT1200). The film substrate was annealed at 70 °C for 15 min. Spin-coating parameters were optimized after several attempts. Water/acetone (70/30) solvent mixture was selected for easy dispersion and fast solvent evaporation. ITO acts as a base electrode. Impedance analyzer's probe act as a top electrode. AC voltage is applied across a dielectric film. Dielectric permittivity, dielectric loss, real and imaginary impedance were measured at different frequencies in the range of 10 Hz to 1 MHz using an impedance analyzer (IM3536, Hioki, Japan). All impedance measurements were made at room temperature.

5.3 MODELING AND SIMULATION

The electrostatic 2D model of a single PS-Fe$_3$O$_4$ patchy microsphere was developed and simulated using the finite element method (FEM) based COMSOL Multi-physics software. Simulation studies require precise geometry, governing equations, and boundary conditions. It is essential to understand the charge build-up mechanism at the interface based on both electrical and chemical analysis. The patchy microsphere in 2D geometry was created by using the information obtained from SEM and impedance analysis. The shape of both PS and Fe$_3$O$_4$ particles were considered to be spherical. The radii of PS and Fe$_3$O$_4$ particles are 2.5 µm and 250 nm, respectively.

The position of Fe_3O_4 particles on a microsphere was chosen based on the symmetry. The number of Fe_3O_4 particles was varied as 8, 20, 24, 28, 32, 36, and 108. It took 108 Fe_3O_4 particles to cover the 2D surface of the PS microsphere fully. Simulation of each of these patchy microspheres containing a different number of Fe_3O_4 particles was performed. The electrostatics and radio-frequency modules in COMSOL for the simulation were selected. The electrostatics from AC/DC module calculates the electric field formation, displacement of an electric field, and polarization in dielectrics under conditions where the distribution of electric charge is prescribed. The physical interface solves the Maxwell constituent equations to determine the electric field formation, using the electric potential as the dependent variable. The dielectric behavior of patchy particles using the electrostatic 2D model as a physical interface was studied. Dielectric permittivity is a function of electric field and polarization according to the Maxwell constituent equation. The field elements are therefore chosen as polarization and electrical fields in the constant frequency domain. The equations include constitutive relations that describe the macroscopic properties of the medium. They are given as

$$\nabla \cdot \vec{D} = \rho_v \text{ and } \vec{P} = \frac{\overrightarrow{dp}}{dv}$$

where $(\nabla \cdot \vec{D})$ is the divergence of the electric field displacement, ε_0 is the dielectric permittivity of the vacuum, and ρ_v is the total electric charge density (charge per unit volume). $\vec{P}$ is the polarization vector, $\overrightarrow{dp}$ is the differential electric dipole moment vector, dv is the differential volume.

Boundary condition: across a material interface, the tangential component of the electric field is continuous. The model solves electric field displacement and polarization according to the governing equation given in the flow diagram shown in Fig. 5.3b. The experimental values of dielectric permittivity, Alternative Current (AC) conductivity, and dielectric loss of PS and Fe_3O_4 particles measured by impedance analyzer, were used as model input. These values are presented in Table 5.1. It also includes the experimentally measured values for PS-Fe_3O_4 patchy microspheres.

The model solves Maxwell's constituent equation (Eq. 5.2) (Maxwell, 1865) and Clausius-Mossotti relation (Eq. 5.3) (Rysselberghe, 2002) to describe a relationship

between the polarization, dielectric permittivity, and electric field formation of PS-Fe_3O_4 microspheres.

$$\vec{D} = \varepsilon_o \varepsilon_r E + \vec{P} \qquad (5.2)$$

$$\vec{P} = \frac{\varepsilon_r - 1}{\varepsilon_r + 2} = \frac{N\alpha}{3\varepsilon_0} \qquad (5.3)$$

Table 5.1: Dielectric properties of neat PS, Fe_3O_4, and PS-Fe_3O_4 patchy microspheres at a 1 kHz frequency measured from the impedance analyzer at room temperature. The values of the properties measured were used as material input parameters for neat PS and Fe_3O_4 particles in simulations.

Material	Dielectric permittivity (ε_r)	AC conductivity (σ_{ac}) S/m	Dielectric loss (tan δ)
Polystyrene (PS)	~2.9	4.8×10^{-12}	0.15
Fe_3O_4	~21	2.9×10^{-8}	0.6
PS-Fe_3O_4	~14.8	7×10^{-10}	0.32

Where ε_0 is the permittivity of a vacuum, ε_r is the relative permittivity of a material, D is electric displacement, E is an electric field, α is polarizability, N is the Avogadro constant. The electric polarization vector (P) describes how the material is polarized when an electric field (E) and electric displacement (D) are present. It can be defined as the volume density of electric dipole moments. P is generally a function of E. The mechanism contributing to dielectric properties is the electric field interaction with electronic, atomic, and dipole polarization.

In an electric field E, the dipole moment of the spheres is at the sphere's center. The magnitude and direction of the dipoles are x=1, y=-1 with the sphere diameter d_1=5µm, d_2=500 nm for PS and Fe_3O_4 particles, respectively, as shown in Fig. 5.3a.
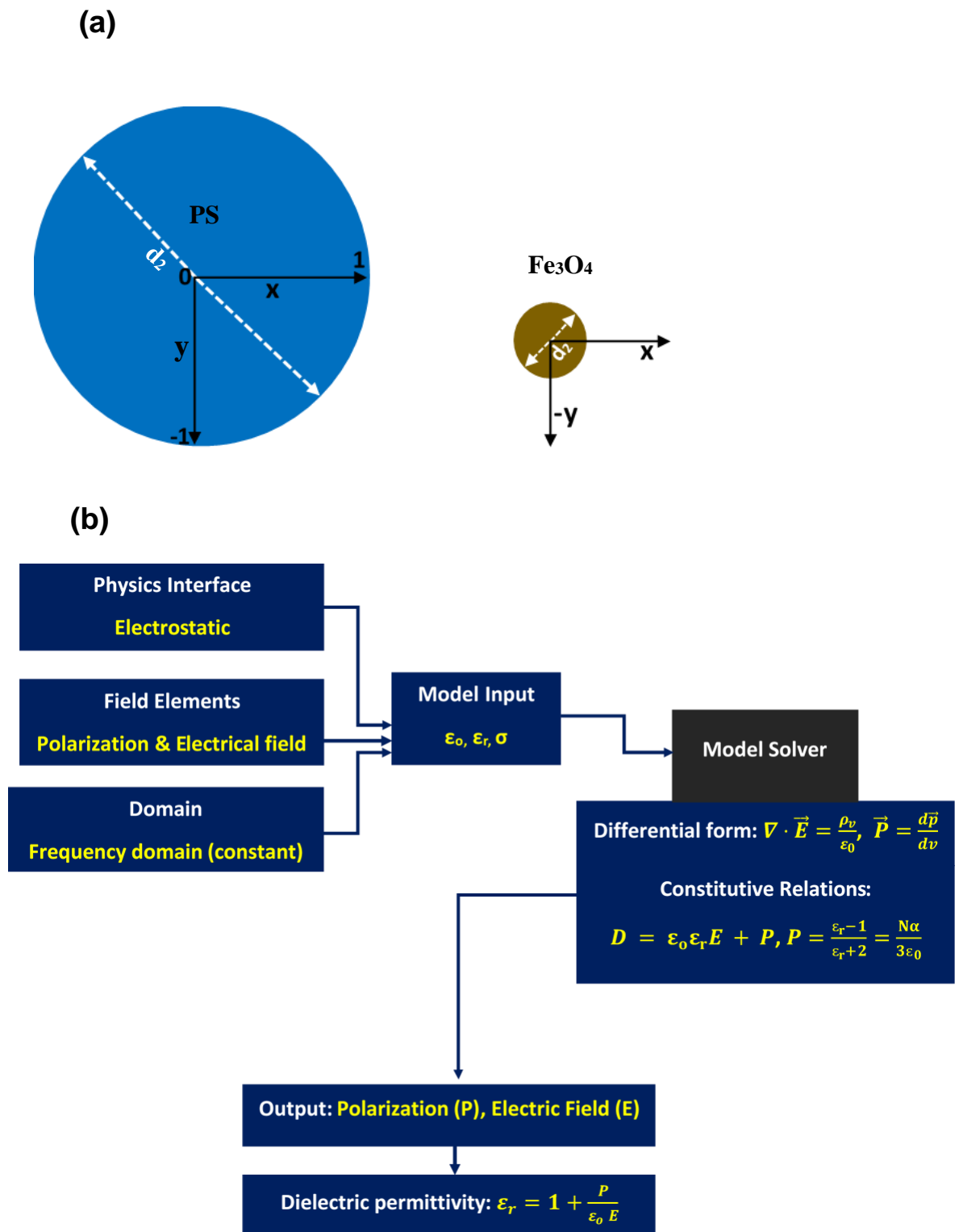
Figure 5.3 (a) Geometry and direction of dipoles considered (b) Flow diagram of electrostatic 2D modeling and simulation of PS microsphere and Fe_3O_4 particles.

5.4 RESULTS AND DISCUSSION

5.4.1 Structure, Morphology, and thermal analysis

Using the morphological details of PS-Fe$_3$O$_4$ particles obtained from SEM analysis, a 2D geometry of PS-Fe$_3$O$_4$ patchy microspheres was developed. The spherical shaped polystyrene microsphere with no Fe$_3$O$_4$ particles with a radius of ~2.5µm shown in Fig. 5.4a. The PS microsphere was decorated with Fe$_3$O$_4$ particles. The radius of Fe$_3$O$_4$ particles was in ~250 nm, as shown in Fig. 5.4b. SEM-EDX elemental color mapping analysis was performed to confirm the composition of the patchy microspheres. Element mapping exhibits the spatial distribution of constituent elements in a patchy sphere shown in Fig. 5.4d. It indicates individual atomic positions of the patchy spheres by their chemical signal (red is Fe$_3$O$_4$, green is PS), and elements can be readily differentiated.

Selective area EDX plot (highlighted in yellow and white color box) shows that the PS surface has no elements except carbon (from PS chain), and signals from smaller spheres correspond to Fe$_3$O$_4$. These images are based on raw data without post-processing signals to avoid bright spot coloring. The individual positions of Fe$_3$O$_4$ spheres on the patchy microsphere are noticeable and differentiated from their neighbors with quite high contrast and signal-to-noise quality. In Pickering emulsion polymerization, Fe$_3$O$_4$ particles dispersed in deionized water and then styrene droplets have only been stabilized by the organization of the Fe$_3$O$_4$ particles at the oil/water (O/W) interface. Styrene droplets begin to polymerize into polystyrene microspheres after adding the radical initiator (AIBN). Fe$_3$O$_4$ particles were eventually adsorbed to the PS microsphere surface. Ultrasonication provides a narrow size distribution of emulsion droplets to obtain uniform patches on microspheres. From the cross-sectional view of the film (Fig. 5.4c), it is verified that inside the film, there are PS-Fe$_3$O$_4$ patchy microspheres. Three different layers can be assigned to the substrate, ITO layer, and PS-Fe$_3$O$_4$ patchy spheres layer. Film thickness is measured to be 8.8 µm.
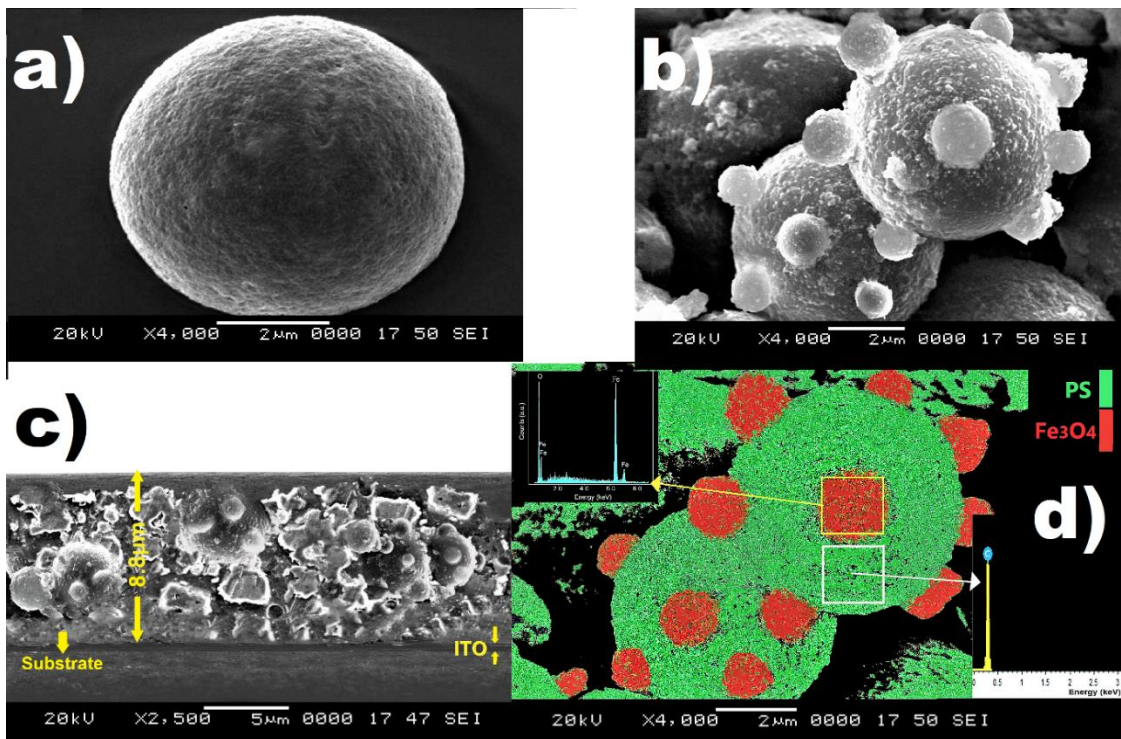
Figure 5.4 (a) Polystyrene microsphere prepared via emulsion polymerization with the aid of ultrasonication (b) PS-Fe$_3$O$_4$ patchy microspheres with the diameter of ~5 µm, uniformly attached Fe$_3$O$_4$ particles (c) Cross-sectional SEM image of PS-Fe$_3$O$_4$ film with a thickness of 8.8 µm coated on ITO substrate (d) SEM-EDX image of PS-Fe$_3$O$_4$ patchy microsphere, elemental color mapping confirms the presence of Fe$_3$O$_4$ (red color) particles on PS surface (green color).

A series of characteristic peaks appear in the XRD pattern of Fe$_3$O$_4$ particles at 2θ values of 30.02°, 35.6°, 42.24°, 53.7°, 57.32°, and 62.9° as shown in Fig. 5.5a. They correspond to the diffractions of 220, 311, 400, 422, 511, and 440 crystal faces of Fe$_3$O$_4$ spinel structure, respectively (JCPDS card 19-0629). The 2θ positions and relative intensities of the reflection signals of Fe$_3$O$_4$ particles are in good agreement with the XRD of standard Fe$_3$O$_4$ samples. Fe$_3$O$_4$ peak positions remained at the same 2θ values in the PS-Fe$_3$O$_4$ XRD pattern. However, due to the presence of polystyrene microspheres, an additional amorphous broad peak is observed at 2θ values of 15-25°.
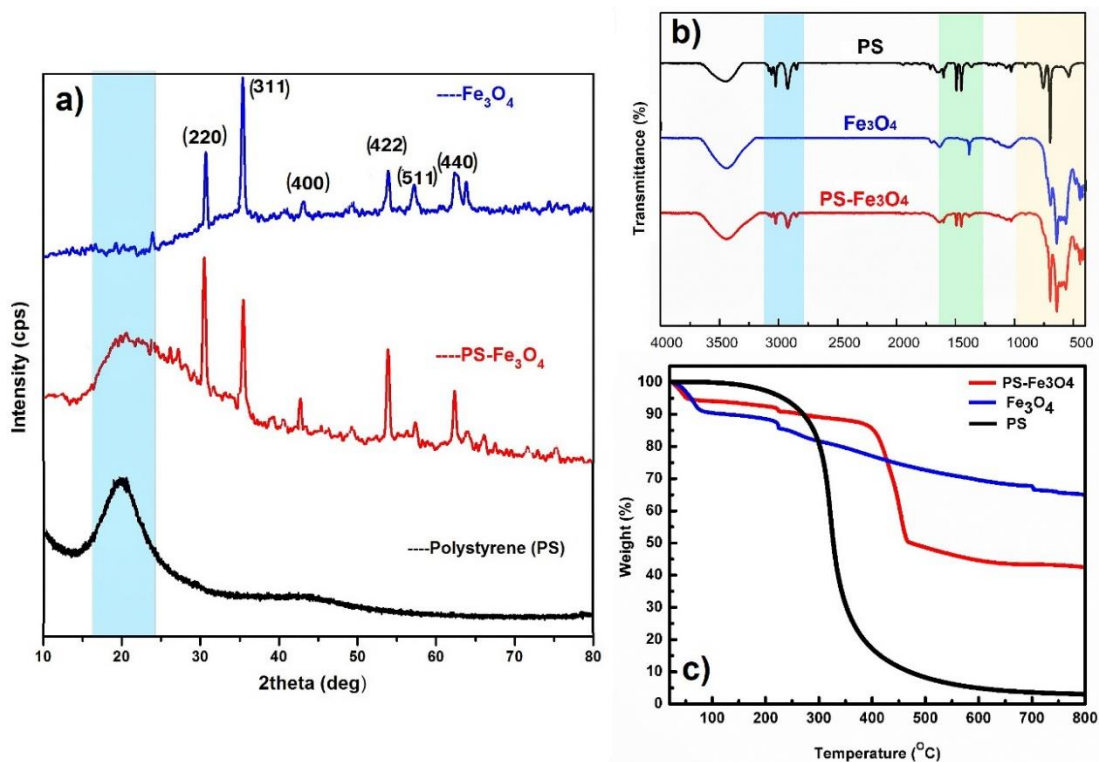
Figure 5.5 (a) X-ray diffraction pattern of PS, Fe_3O_4, and PS-Fe_3O_4 patchy microspheres, data recorded at room temperature. Combined amorphous and crystalline peaks in PS-Fe_3O_4 were highlighted (b) FTIR transmittance spectra of PS, Fe_3O_4, and PS-Fe_3O_4 patchy microspheres, characteristic peaks of both PS and Fe_3O_4 were highlighted (c) TGA weight loss curves of PS, Fe_3O_4, and PS-Fe_3O_4 patchy microspheres were taken in the temperature range of 30-800 °C.

FTIR spectroscopy was performed to investigate the chemical structures of the Fe_3O_4, PS, and PS-Fe_3O_4 microspheres. Samples were loaded into KBr pellets and scanned over a wavenumber of 4000-400 cm^{-1}. In Fig. 5.5b, Fe-O vibration modes are attributed to bands of approximately 560 cm^{-1}. The broadband with low intensity at 3400 cm^{-1} shows hydroxyl groups' presence on the surface of Fe_3O_4. The peaks of the aromatic ring stretching vibration at 1600-1430 cm^{-1} are observed from the FTIR spectrum of PS. The bands of approximately 760 cm^{-1} and 690 cm^{-1} confirm the presence of a single aromatic group. The C-H stretching vibration is also detected at 2975-2950 cm^{-1}. The FTIR spectrum of PS-Fe_3O_4 microspheres displays the typical chemical characteristics of PS and Fe_3O_4 particles.

The TGA curve of neat Fe_3O_4 indicates that the weight loss of Fe_3O_4 is because of the presence of oleic acid content shown in Fig. 5.5c. From the TGA curve of Fe_3O_4 and PS-Fe_3O_4, the weight loss that can be seen in till 100 °C is due to the presence of solvents and moisture and a weight loss of 3% at 220 °C is due to the presence of carboxylate group in oleic acid. In Fe_3O_4, from 250 to 700 °C, there is a prominent weight loss of 15%, and after 700 °C, weight loss is negligible. The weight loss over the temperature range from 250 °C to 700 °C is due to the decomposition of the sorbed oleic acid used as a coating agent to prevent the agglomeration of Fe_3O_4 particles. The weight loss of Fe_3O_4 particles themselves, attributed to the reducing gas produced by the coating agent, could be another reason. The peak at ~700 °C is attributed to the crystalline phase transition of Fe_3O_4. PS is stable up to 250 °C, the weight loss from 250-400 °C is due to the degradation of polymeric chains. The maximum rate of weight loss of PS-Fe_3O_4 occurred in the temperature range of 370-450 °C due to the thermal degradation of polystyrene. The improvement in the thermal stability of the PS-Fe_3O_4 patchy microsphere is attributed to the protective effect of the Fe_3O_4 particles on PS spheres. The PS-Fe_3O_4 interface restricts the thermal motion of the PS chains due to the chemical bonding (confirmed by FTIR) between PS and Fe_3O_4. The energy demand for breaking this interface bond is high and delays the PS microsphere degradation. It is known that at a temperature above 800 °C, the organic part of the patchy particles burns away, and the remaining percentage after calcination corresponds to the inorganic content. The TGA analysis exhibited the better thermal stability of PS-Fe_3O_4 patchy microspheres.

5.4.2 Dielectric properties of PS, Fe3O4, and PS-Fe3O4 patchy microspheres

Dielectric permittivity, dielectric loss, and AC conductivity were measured in the frequency range of 10 Hz to 1 MHz using impedance analyzer at room temperature shown Fig. 5.6. The values obtained for neat PS, Fe_3O_4, and PS-Fe_3O_4 patchy microspheres are tabulated in Table 5.1. The dielectric permittivity of PS increased from ~2.9 to 14.8 at 1 kHz frequency after decorating with Fe_3O_4 particles on its surfaces shown in Fig. 5.6a. It is ascribed to the space charge effects of Maxwell-

Wagner-Sillars interfacial polarization. Maxwell-Wagner-Sillars (MWS) model describes the polarization at both mesoscopic and microscopic scales in the low-frequency region (Zhang et al., 2005). This model applies to all inhomogeneous materials, like multiphase materials, and materials with a broad range of interfaces and defects. On the lines of this model, the reason for improved dielectric permittivity could be interpreted precisely. PS-Fe_3O_4 patchy microspheres have a phase anisotropy with different dielectric permittivity and electrical conductivity.
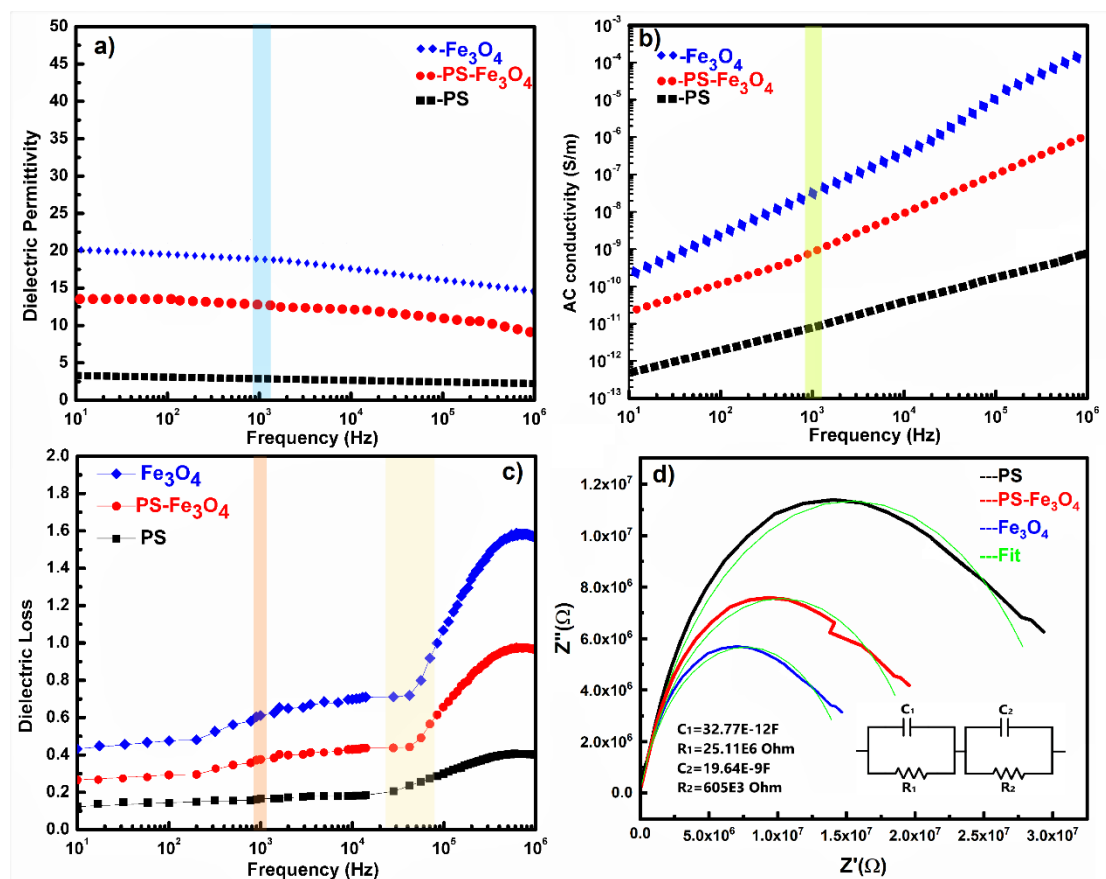
Figure 5.6 (a) Dielectric permittivity vs. frequency plot of PS, Fe_3O_4, and PS-Fe_3O_4 patchy microsphere dielectric film (b) AC conductivity vs. frequency plot. The value of dielectric permittivity and AC conductivity of all three samples were highlighted (c) Dielectric loss vs. frequency plot, the dielectric loss at 1 kHz and an exponential loss after 10^4 Hz were highlighted. Impedance data were recorded at room temperature in the frequency range 10-10^6 Hz (d) Nyquist plot-imaginary impedance (Z″) vs. real impedance (Z′) of PS, Fe_3O_4, and PS-Fe_3O_4 dielectric film. The inset shows the equivalent parallel circuit and the values of each component.

Two mechanisms for patchy microspheres can be witnessed in the applied electric field, according to MWS dispersion theory. First, the space charges present in the system could move and trap at the interfaces, leading to a high dipole moment. Second, the instantaneous charge builds up, and interfacial polarization occurs at the interface due to the difference in Fermi level and permittivity mismatch between Fe_3O_4 particle and PS microspheres. To describe how the interfaces react with changing electric field, Tanaka et al. (2005) proposed a multi-core model for a nanocomposite consisting of spherical inorganic nanoparticles embedded in a polymer matrix. Based on the multi-core model and our simulation results, a new charge build-up mechanism at the interface of polymer and inorganic particles was proposed, as shown in Fig. 5.7a. PS-Fe_3O_4 patchy microsphere can be considered as a three-phase system, namely Fe_3O_4 particles, PS microsphere, and interface created between them. When the electric field applied to the three-phase system, enhanced mobile charge interference from charge trapping, charge distribution mechanisms at the PS-Fe_3O_4 interface can be observed. Also, the surface of the Fe_3O_4 becomes charged due to the difference in the Fermi level or chemical potential of the Fe_3O_4 and PS.

To investigate surface charge formation, the surface current density for single Fe_3O_4 particle attached to the PS microsphere presented in Fig. 5.7d. The simulation results confirmed that the surface of Fe_3O_4 is more charged than the PS microsphere. Under an applied electric field, the interfacial charges present in the PS spheres form a Gouy-Chapman-Stern layer at the PS-Fe_3O_4 interface (Peng et al., 2019). Due to this layer and interface charge build-up, the superimposition of dipoles may arise from Fe_3O_4 particles and the PS sphere. Because of this superimposition, an induced electric field layer is witnessed in the interfacial region shown in Fig. 5.7b and magnified image Fig. 5.7c. It was anticipated that this interfacial superimposition could cause a collaborative effect among other microspheres to intensify the interface effects on the polarization and dielectric permittivity.
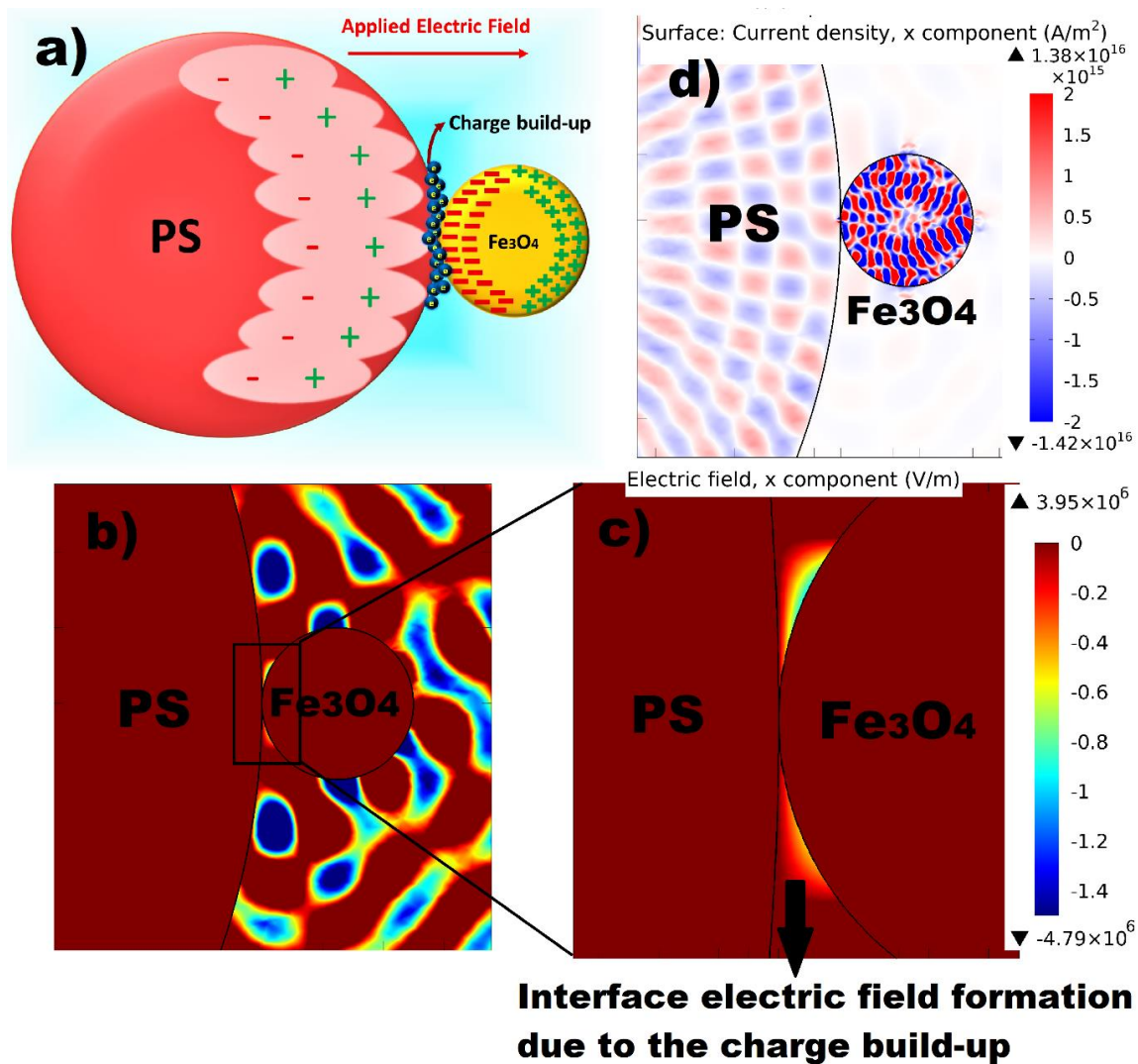
Figure 5.7 (a) Schematic of charge build-up due to the dipole-dipole interaction at the PS and Fe$_3$O$_4$ interface (b) Interface electric field formation in an applied electric field at 1 kHz frequency for a single PS-Fe$_3$O$_4$ patchy microsphere (c) Magnified PS-Fe$_3$O$_4$ interface image to confirm the formation charge build-up layer (d) Surface current density created on PS and Fe$_3$O$_4$ sphere surface under an applied electric field.
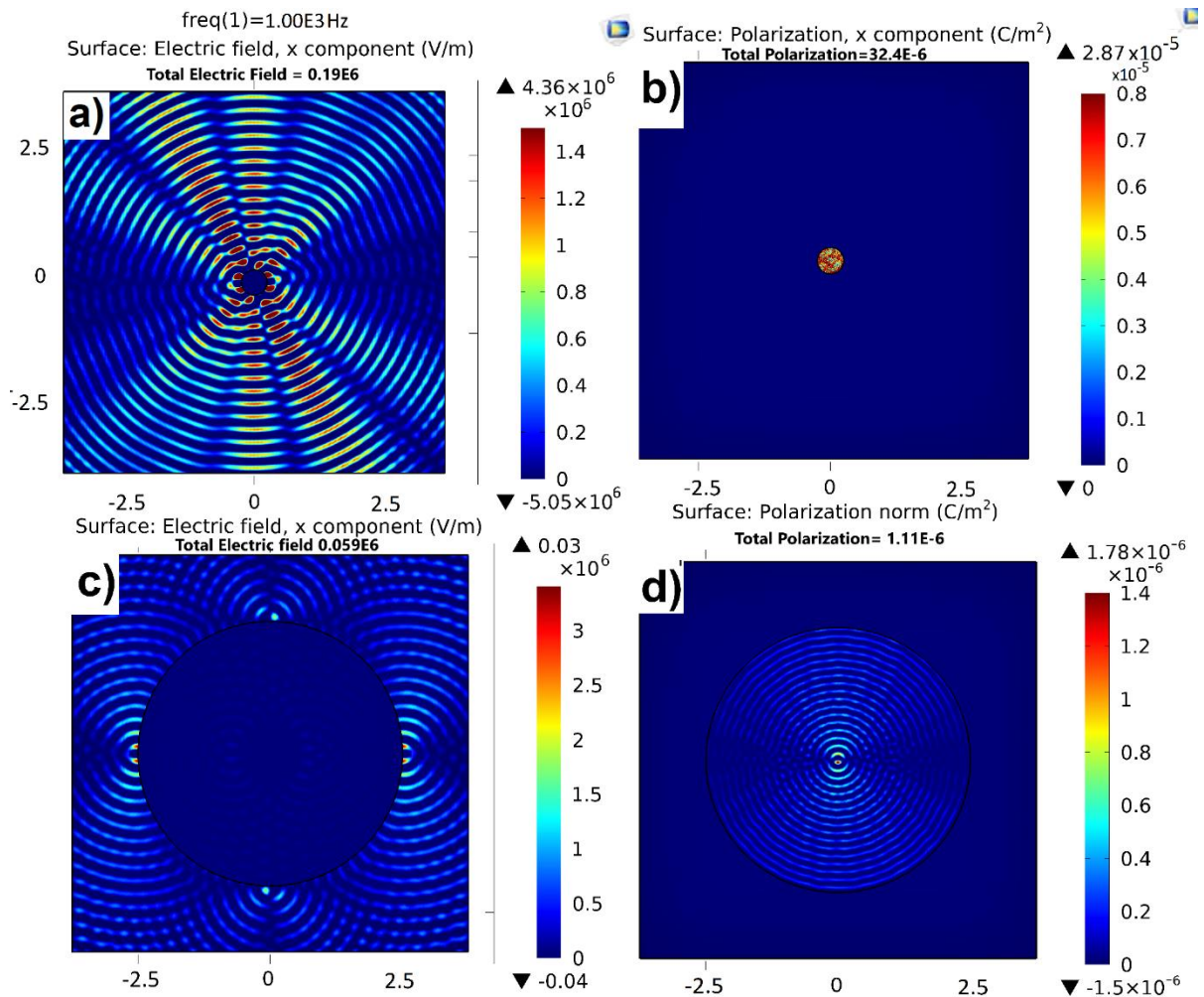
Figure 5.8 Individual electric field formation and polarization at 1 kHz frequency (a) Electric field formation from Fe_3O_4 particles with a radius of 250 nm (b) Polarization on the surface of the Fe_3O_4 particles (c) Electric field formation from the PS microsphere of size 2.5 µm radius (d) Polarization on the surface of a PS microsphere. Units on the x-y axis are in µm. All the simulations were done at room temperature in COMSOL Multiphysics.

The simulation data for Fe_3O_4, PS, PS-Fe_3O_4 patchy microsphere with 8 and 108 Fe_3O_4 particles. 108 Fe_3O_4 particles were sufficient enough to cover the PS microsphere in the 2D surface. The formation of an electric field (0.19×10^6 V/m) and polarization (32.4×10^{-6} C/m^2) in Fe_3O_4 at 1 kHz frequency is shown in Fig. 5.8a&b, respectively. Figure 5.8c shows the electric field of 0.059×10^6 V/m for neat PS, which

is lower than that of Fe_3O_4. A polarization of neat PS is shown in Fig. 5.8d. Polystyrene is nonpolar and does not have a conducting path, and hence, a lower value of polarization and the electric field was obtained.

The high electric field formation (Fig. 5.9a) and heterogeneous distribution of polarization (Fig. 5.9b) were observed at the interface due to the random dipole moment and dipole-dipole interaction at a polymeric-inorganic interface. The polarization of the particles mainly depends on the surface conductivity that depends on the particle size. That means the overall conductivity of Fe_3O_4 particles is higher than PS microspheres, making them more polarized than PS microsphere. The polarization of material may result from dipoles created by the chemical interaction of charges within the material (permanent dipoles) or by the application of an external electric field (induced dipoles). Enhancement of the electric field due to the increased dipole moment, charge build-up, and trapping at an interface is observed in the PS-Fe_3O_4 patchy microsphere compared to neat PS and Fe_3O_4 individually. This enhancement of the electric field distortion improves the alignment of the dipoles in the applied field direction. In the electric field, two polarizations are acting on the medium. One is the polarization of the PS microsphere, and another one is the surface-bound local polarization due to the Fe_3O_4 particles. These two polarizations contribute to effective interfacial polarization. As interfacial polarization increases, the dielectric permittivity of the patchy microspheres is also increasing. The polarization and electric field values obtained from the simulations are presented in Table 5.2. The dielectric permittivity values of PS, Fe_3O_4, and PS-Fe_3O_4 are calculated using the Eq. 5.1. Experimentally determined dielectric permittivity values are tabulated and compared with the values predicted by the model. The predicted values of the model are well in agreement with the actual values obtained from the experiment. The induced field formation improves the electric field due to the Fe_3O_4 particles. Zang and co-workers (Zhang et al., 2014) developed a phase-field model to understand the polarization and electric field distribution in TiO_2 nanofibers embedded with $BaTiO_3$ nanoparticles further fused with polyvinyl difluoride (PVDF) polymer matrix. According to their study, the TiO_2 interfacial layers create a percolation path for the accumulation of charges at the interfacial region of TiO_2-$BaTiO_3$ nanofibers, which further enhances the dielectric permittivity. The improved dielectric

permittivity of PS-Fe$_3$O$_4$ patchy microspheres is due to the charge accumulation in the interfacial region of PS and Fe$_3$O$_4$ by correlating the phase-field model with the present study.
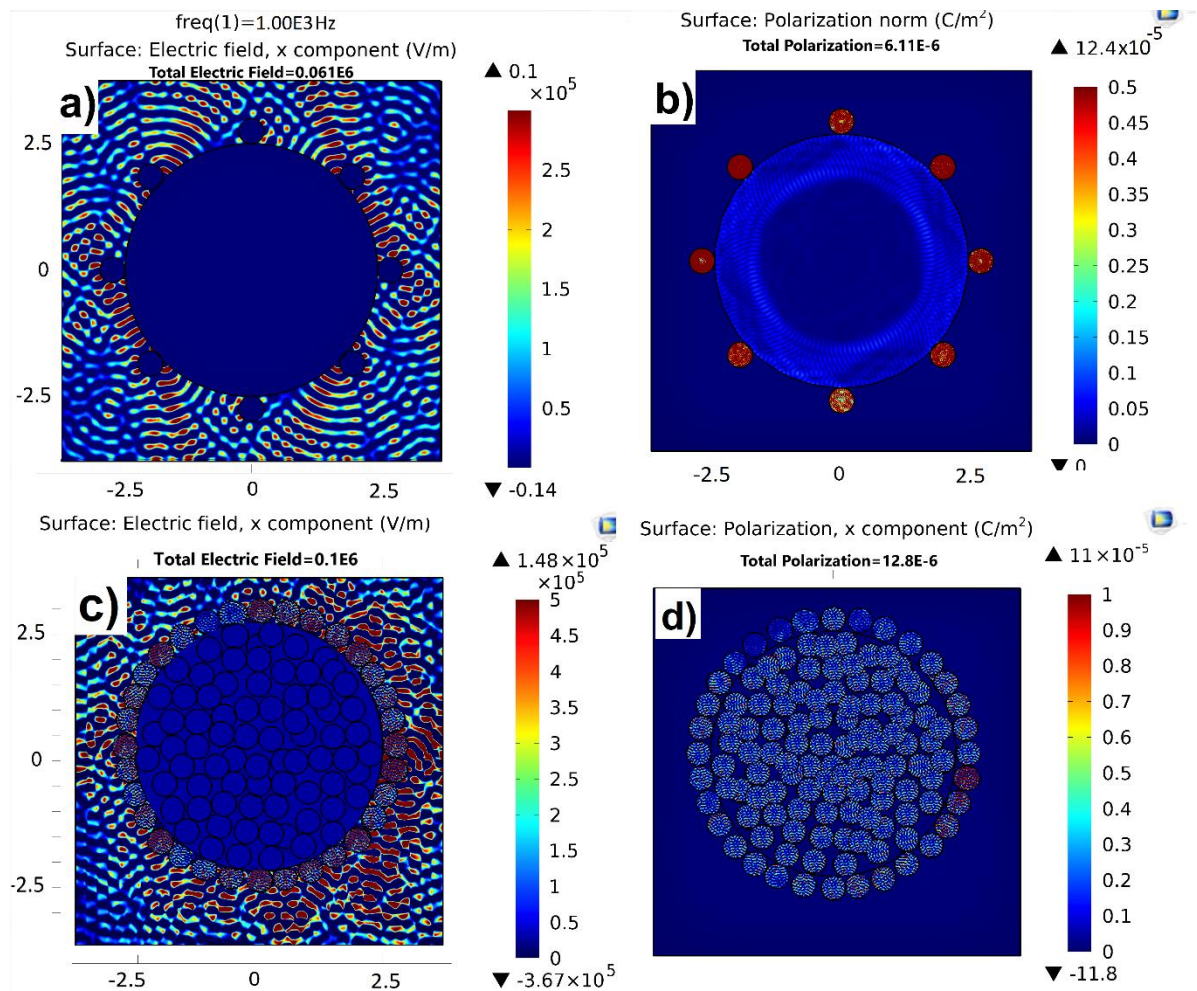
Figure 5.9 (a) Electric field formation from PS-Fe$_3$O$_4$ patchy microsphere with 8 Fe$_3$O$_4$ surface particles of radii 250 nm (b) Polarization on the surface of the PS-Fe$_3$O$_4$ patchy microsphere (c) Electric field formation from the PS microsphere covered with 108 Fe$_3$O$_4$ particles (d) Polarization on the surface of a PS-Fe$_3$O$_4$ patchy microsphere with 108 Fe$_3$O$_4$ particles. Units on the x-y axis are in μm.

In general, the dielectric interfaces are the ideal location for an accumulation of space charges. The conductivity of the dielectric material plays a vital role in the interface polarization process. From Fig. 5.6b, it can be observed that the increased AC

conductivity with an increase in frequency for both Fe_3O_4 and PS-Fe_3O_4 samples. In neat PS, since there is no conduction path, polymer chains act as a dielectric barrier at low frequency, and AC conductivity is less compare to Fe_3O_4. Whereas in high-frequency electronic polarization takes place in PS leads to increased AC conductivity. Koop's theory (Koops, 1951) can describe the frequency dependence of electrical conductivity and dielectric loss in Fe_3O_4 and PS-Fe_3O_4. In Koop's theory, conductivity is associated with the presence of grains with high conductivity and their boundaries with high resistance in higher frequencies ($f>10^4$ Hz at room temperature). The increased conductivity in the high-frequency region can be understood by the increased hopping of the charge carrier phenomenon. This conductivity is related to the occurrence of Fe^{3+} and Fe^{2+} ions in the magnetite structure and has been ascribed to electron hopping between them. Since there is an electron hopping between Fe^{2+} and Fe^{3+} ions, the electric field formation in Fe_3O_4 and PS-Fe_3O_4 is higher than the neat PS. In PS-Fe_3O_4 patchy microspheres, the charge carriers are localized at the PS-Fe_3O_4 interface, and all Fe^{2+} ions in the octahedral site participate in the hopping transport. Hence, AC conductivity is increased in both Fe_3O_4 and PS-Fe_3O_4. The dielectric loss is low at lower frequencies for all the three samples (Fig. 5.6c). The maximum dielectric loss occurs in the frequency range of 10^4 to 10^6 Hz highlighted in Fig. 5.6c.

Polarization oscillates with the changes in the alternating current field. It takes some time for dipoles to align in the material. Dipolar alignments can respond quickly enough at a low frequency so that all three samples show a less dielectric loss, almost static behavior. However, there is not enough time for dipoles to react to the changing field at high-frequency dipoles. Therefore, the maximum dielectric loss in both Fe_3O_4 and PS-Fe_3O_4 was observed. Because only electronic polarization occurs in polystyrene, its dielectric permittivity and dielectric loss are relatively static at high frequencies. Impedance data are displayed in the form of Nyquist plot imaginary impedance Z″ (capacitive) against real impedance Z′ (resistive). From the Nyquist plot (Fig. 5.6d), a single semi-circle in both neat PS and Fe_3O_4 is seen, and it behaves electrically as an RC network with a single relaxation process. Whereas in PS-Fe_3O_4, one semi-circle followed by a sharp step-down line is identified. This behavior indicates that these patchy microspheres offer two types of impedance, one from the bulk PS-

Fe_3O_4 particles and another from the interface of PS and Fe_3O_4. Due to the rapid accumulation of charges, the charge transport process at the PS-Fe_3O_4 interface is high compared to the bulk PS-Fe_3O_4. Consequently, the impedance offered by the PS-Fe_3O_4 film identified by a first semi-circle assigned to bulk PS-Fe_3O_4. However, the sharp step-down line followed by a second semi-circle of PS-Fe_3O_4 attributed to higher charge transport from the interface of PS-Fe_3O_4.

Table 5.2: Polarization, electric field, predicted dielectric permittivity, and experimentally obtained dielectric permittivity values of PS, Fe_3O_4, and PS-Fe_3O_4 at a 1 kHz frequency under AC field obtained from COMSOL Multiphysics.

Material	Polarization ($\mu C/m^2$)	Electric field (MV/m)	Predicted Dielectric Permittivity	Experimental Dielectric Permittivity
Fe_3O_4	32.4	0.190	20.26	21
Polystyrene	01.11	0.059	03.12	2.9
PS with 8 Fe_3O_4	06.11	0.061	12.31	14.8
PS with 20Fe_3O_4	06.82	0.065	12.85	
PS with 24Fe_3O_4	07.24	0.071	12.52	
PS with 28 Fe_3O_4	09.93	0.082	14.68	
PS with 32 Fe_3O_4	10.41	0.086	14.67	
PS with 36 Fe_3O_4	10.73	0.090	14.45	
PS with 108 Fe_3O_4	12.80	0.100	15.46	

The neat PS shows step-upward at the end of the semi-circle with higher impedance. In neat PS, dipolar alignments cannot respond quickly at high frequency to the changing electric field, which provides a high resistance to charge transfer. Further, the Nyquist plot allows describing various components and their values in the equivalent circuit. From Fig. 5.6d, the inset shows the two parallel Resistive-Capacitive (RC) circuit, a model connected in series, and the values of each component in the equivalent circuit. The capacitance values obtained from the equivalent-circuit model could be assigned to bulk capacitance and surface layer capacitance of the sample. It means that the first RC circuit is assigned to bulk PS- Fe_3O_4 and the second one to the interface of PS and Fe_3O_4. The interface is more capacitive than the PS-Fe_3O_4 bulk. It is due to the increased polarization at the interface that can drive more electric charges in the electric field applied. Simulation results also confirmed the increased electric field formation (Fig. 5.9c) and polarization (Fig. 5.9d) at the interface of PS-Fe_3O_4 than the individual materials. From Fig. 5.6d, it can be understood that modulus of impedance decreases with an increase in frequency in neat PS and Fe_3O_4. However, in the case of PS-Fe_3O_4 patchy microspheres, two impedance behavior is noticed. The interface of PS and Fe_3O_4 tends to behave more capacitive at high-frequency so that the variation can be noticed compared with the low-frequency behavior. The capacitance of the material can be engineered by tuning the interfacial region and surface morphology. By changing the orientation and amount of Fe_3O_4 particle microscopically, one can design a capacitor or a transistor with the desired value of dielectric permittivity.

5.5 EXPERIMENTAL METHOD

5.5.1 Synthesis of La_2O_3-ZrO_2 dumbbell-shaped Janus particles

Dumbbell shaped La_2O_3-ZrO_2 Janus particles were synthesized using sonochemical assisted the phase-separation method. 0.5g of lanthanum chloride was dissolved in 50ml distilled water. It was sonicated first for 15 min, which results in La_2O_3, followed by the addition of 0.5g of zirconium oxynitrate. The mixture was sonicated for 30 min to get Janus particles. A 20 kHz frequency probe sonicator with a

500 W ultrasonic generator and 13.2 mm diameter probe was used. The sonicator was operated at a 40% power amplitude in a pulsed mode (on/off ratio of 5s/3s).

5.6 RESULTS AND DISCUSSION

Figure 5.10a confirms the formation of La_2O_3-ZrO_2 dumbbell-shaped Janus particles. Contrast color mapping from EDX analysis shows the presence of La_2O_3 (blue) and ZrO_2 (red) elements (Fig. 5.10b).

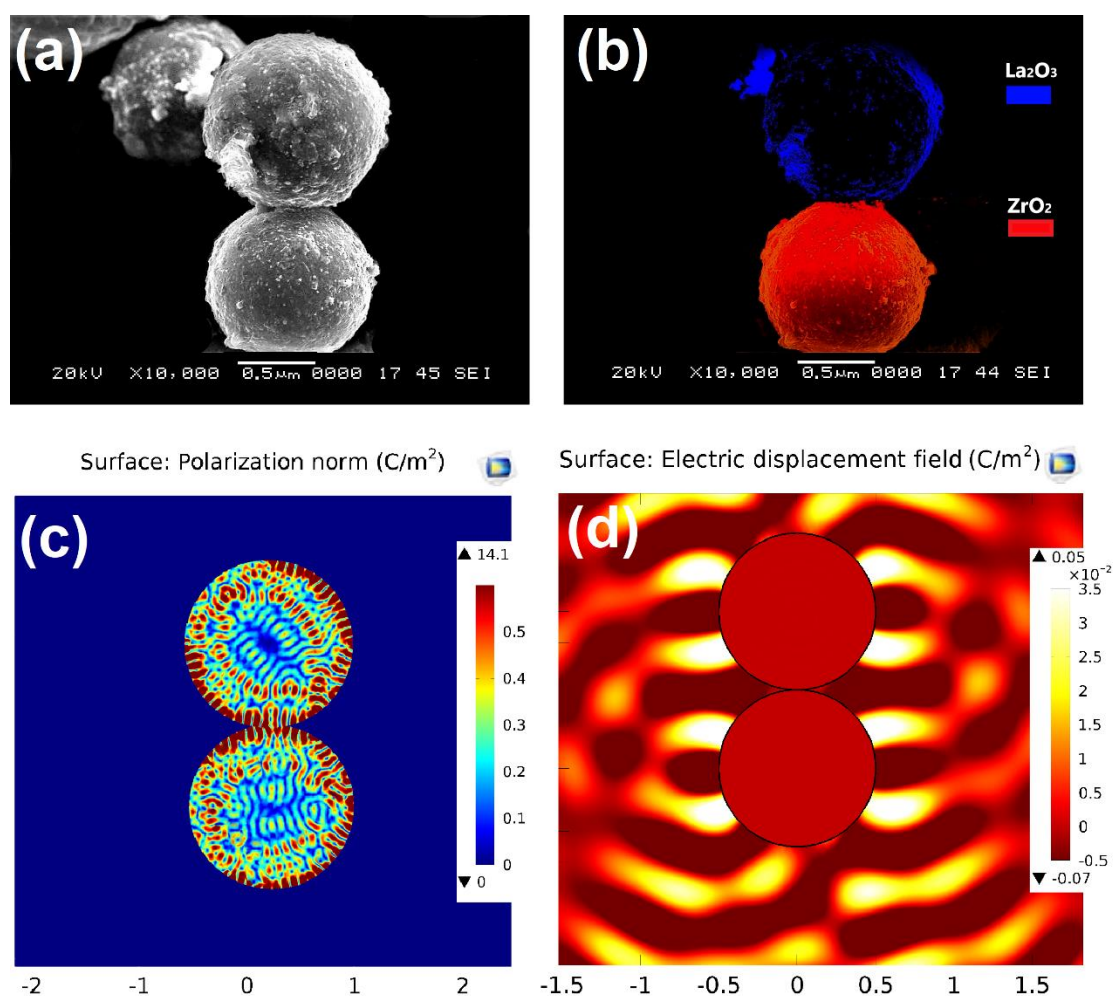Figure 5.10 (a) SEM image of dumbbell shape Janus particles captured at 0.5 µm scale (b) EDX image confirms the presence of two different metal oxide microspheres which are La_2O_3 and ZrO_2 further confirmed by contrast color mapping (c) Polarization on the surface of the dumbbell shape Janus particles (d) Electric field formation from La_2O_3-ZrO_2 distribution around the microspheres.

The microscopic visualization of the electric field and polarization is important to understanding the dielectric behavior of dumbbell shape Janus particles. The polarization is caused by charge asymmetry, i.e., the center of gravity of the positive charges varies from that of the negative charges when there is an external electric field. The polarization formation (Fig. 5.10c) on both the particles was comparable, and the interface between them shows the highest polarization due to the rapid physiochemical changes under an applied electric field. Changes may involve phase transformation, such as crystallization or phase separation, and chemical reactions between adjacent layers, including inter-diffusion. The electric field formation of Janus particles obtained from the computational simulation is shown in Fig. 5.10d. The uneven distribution of the electric field around the Janus particles was observed, and it could lead to the enhanced dielectric properties of Janus Particles. Overall, the interface of the La_2O_3-ZrO_2 Janus particles exhibited a vital role in interfacial polarization.

For the comparison, the dielectric analysis was carried out for the $La_2Zr_2O_7$ (LZO) sample, a single-phase system. Figure 5.11a presents the dielectric permittivity of LZO powder and La_2O_3-ZrO_2 dumbbell shape Janus particle. La_2O_3-ZrO_2 shows the k value of 320, which is 11 times higher than the LZO powder sample. The increment in dielectric permittivity due to the rapid electric field formation and surface polarization. The interface between these Janus particles is energy storage spots where electric dipole drastically changes its path of potential. In general, there will only be a few of the possible polarizations in a given material. The maximum value of dielectric permittivity would be at the low frequency when there are multiple polarizations such as electronic, ionic, interfacial polarization present in a material. Also, these polarizations will contribute to the overall dielectric permittivity at a given AC frequency.

The dielectric loss of the Janus particle is a minimum below 1 MHz frequency range, and the rapid increase in a loss at a higher frequency than the LZO sample has shown in Fig. 5.11b. The reason could be the charged defects and no time for interfacial dipoles to respond to the external electric field immediately, which leads to the dielectric loss.

The breakdown strength of LZO and Janus particle is calculated using a probability of failure vs. electric field shown in Fig. 5.11c. The breakdown strength of the Janus particle is 40.8 MV/m 6 times higher than the LZO sample, which is 6.2 MV/m, possibly due to the strong interfacial metal-oxygen-metal (M-O-M) bond between La_2O_3 and ZrO_2. The energy storage density of LZO is 20.6 J/cm^3, and the Janus particle is 136 J/cm^3 shown in Fig. 5.11d. The plausible explanation for this high energy storage density is the accumulation of charges between the three-dielectric media at the interfaces. Such charge accumulation at the interfaces produces Maxwell-Wagner-Sillars (MWS) polarization. The MWS polarization arises when the current, including the dipole reorientation component, passes via materials of electrical inhomogeneity. The bonded charges accumulate at the interfaces between two different dielectric media.
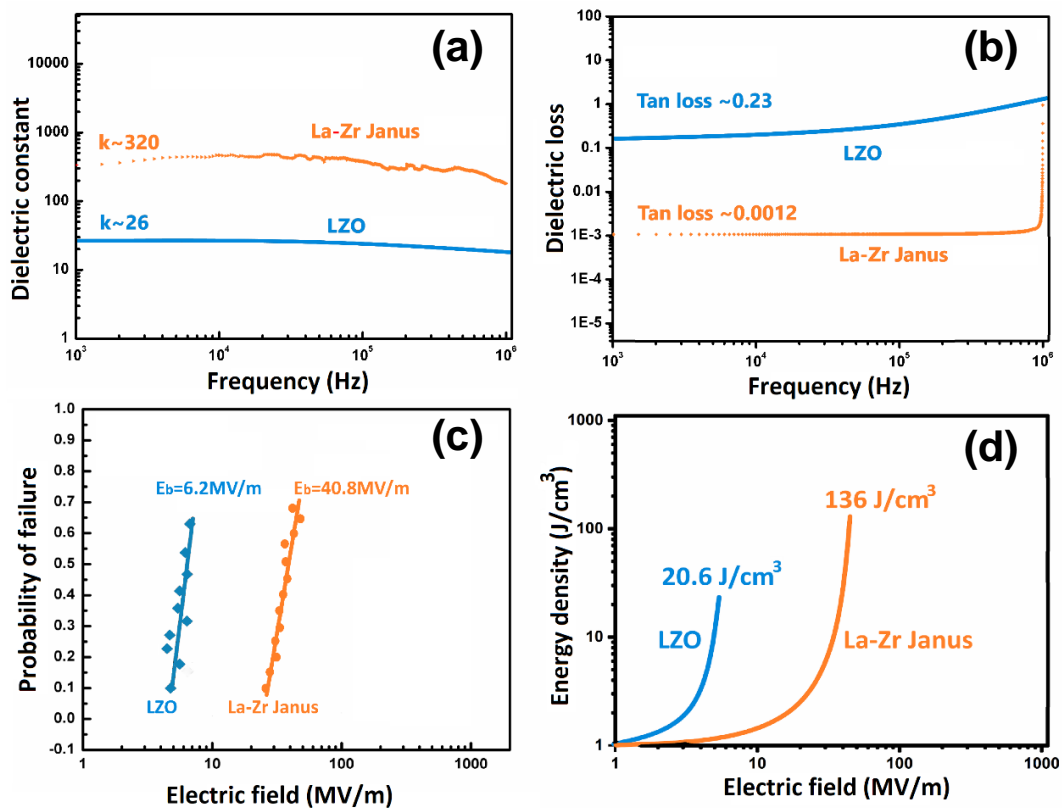

Figure 5.11 Frequency-dependent (a) Dielectric permittivity and (b) Dielectric loss of the LZO and La_2O_3-ZrO_2 Janus particles in the range 1kHz-1MHz at room temperature (c) Breakdown strength is calculated using a probability of failure vs. the electric field (d) Energy storage density vs. electric field of LZO and La_2O_3-ZrO_2 Janus particles.

In Janus particles that enhance the dielectric properties, dielectric breakdown strength, interfacial contribution, interparticle surface chemistry, and contamination due to ionic species are significant. The function of the interface must be taken into account, not just in terms of its nature and also the way it influences the overall system. (Sudeep and Emrick, 2007) used experimental results and mathematical calculations for molecular dipole polarization to explore the effect of the interface on the dielectric properties. They have demonstrated that the dielectric characteristics of metal oxide-polymer regions influence the material's overall dielectric reaction. The interphase area is largely reliant on the chemical bonding at the filler interface and is capable of forming covalent or hydrogen bonds to the filler surface. The interface material has unique dielectric characteristics; it is an interface area of dielectrics consisting of mismatch and phase difference.

5.7 SUMMARY

A 2D electrostatic model for a neat Fe_3O_4, neat PS, and PS-Fe_3O_4 patchy microsphere with a specific geometry was developed based on experiments to understand the dielectric behavior of the PS-Fe_3O_4 interface. A new charge build-up mechanism at the interface was proposed based on computational results along with experimental outcomes. Due to enhanced polarization and induced electrical field formation, charge build-up at the PS-Fe_3O_4 interface is greater than that in bulk. Dielectric responses are dominated by the interfacial region of polystyrene and Fe_3O_4. The size, shape, and position of Fe_3O_4 particles are crucial in developing patchy microspheres. Local morphology, interface area, crystallinity, and ionization of the interfacial region of polymer-inorganic surface determine the overall dielectric permittivity of the patchy microspheres. Controllable patchy particle design can provide excellent paradigms for the design and development of high-performance polymer dielectrics. Tailoring the patch surface and tuning the size of the polymer microsphere are critical approaches to meeting future functional electronic devices. Polymer-inorganic interface chemistry and design opens up a new avenue to develop efficient hybrid materials for future electronics.

The present approach of sonochemical synthesis has offered a new route to the preparation of dumbbell shape Janus particles with tuneable shapes and novel properties. The La_2O_3-ZrO_2 Janus particles show high dielectric permittivity and better energy storage density with an improved breakdown strength. Computational results exhibit the effect of the M-O-M interface on the polarization and electric field. The Janus particles find potential uses in areas such as electroactive energy storage systems, targeted drug delivery, magnetically operated optical switches, processing of micro engines, assembly of colloid crystal systems with novel symmetries, and stabilization/destabilization processes of emulsions.

This page intentionally left blank

CHAPTER 6

SUMMARY AND CONCLUSIONS

In this work, three types of dielectrics, such as metal oxide, metal oxide reinforced polymers, and metal oxide decorated high-k polymer dielectrics, were fabricated at low temperatures (below 100 ºC) using a sonochemical method. The lowest fabrication temperature reported so far. A new way of preparing metal oxide-based dielectric ink using the sonochemical approach have been reported. The sonochemical approach allows a greener and inherently safer way to create microscopically supercritical conditions of high temperatures and pressures in liquids. This is not readily achievable by other conventional methods such as hydrothermal, solvothermal, solution combustion, and microemulsion. This exciting approach benefits the low-temperature solution process and aids in dispersing metal oxides better in a polymer medium.

Metal oxide dielectrics, namely, Lanthanum Cerium Oxide (LCO) and Lanthanum Zirconium Oxide (LZO), have been successfully synthesized by a sonochemical method at a relatively lower temperature. LZO dielectric ink was directly used for the fabrication of a thin film capacitor. Various characterization techniques were used to examine the crystallinity, particle size, phase purity, the thickness of the thin film. Performance of the LZO-PMMA and P(VDF-HFP)/LZO dielectric film has been studied with different LZO loading. Dielectric analysis exhibit that 10-15% LZO loading is sufficient to obtain high energy storage thin films with a minimum dielectric loss. Uniform distribution of the LZO particles in a polymer matrix is crucial to achieving high dielectric permittivity and energy storage density with a minimum dielectric loss. The sonochemical method helps to overcome the difficulty of LZO particle agglomeration and their phase separation in the polymer matrix. It also enhances the interfacial interaction between LZO particles and the polymer phase.

Computational modeling helps us to avoid wastage of material and to optimize the filler content to achieve the most desirable dielectric properties of the dielectric composites. The present findings suggest that the modeling approach can be used to model thin-film capacitors with polymer composite as a dielectric layer to estimate the energy density.

Next, the anisotropic particles named Polystyrene-iron oxide (PS-Fe_3O_4) patchy particles and lanthanum oxide-zirconium oxide dumbbell shape Janus particles were fabricated. The unique structure of patchy particles opens up a new research possibility, especially the interface of PS-Fe_3O_4 particles. The computational model using COMSOL was developed to understand the behavior of polymer-inorganic interface under an applied electric field. The studies showed exciting results, such as rapid polarization and electric field formation at the interface were found. Interfaces play a vital role in virtually all materials and devices, encompassing a wide variety of applications related to bulk and surface processes. A new mechanism at the interface was proposed after validating computational results with experimental outcomes. The interfacial region of anisotropic particles dominates in determining dielectric responses.

The outcome of both the computational simulation and experiment analysis inferred that the energy storage capacity is more at the interface than in bulk. It is the first sort of report that describes the role of patchy particle and Janus particle interface in improving dielectric properties. By interface study, it is possible to design and synthesize materials with new functionalities with molecular-level accuracy, enabling new frontiers in electroactive materials.

FUTURE SCOPE

Application areas that remain open for further study for lanthanum zirconium oxide dielectrics and Janus particle include epitaxial oxide integration on Silicon. PMMA and PVDF-HFP polymers exhibit excellent dielectric properties with suitable metal oxide fillers. Such polymer composite dielectrics can be used as lightweight, flexible, transparent high-capacitive thin-films in biosensors. Applicability of these polymer composite dielectrics at high-temperature (>200 ℃) operation can be explored.

Computer modeling and polarization imaging will contribute to a deeper understanding of interfacial interactions and provide a picture of the local breakdown phenomenon's impact on the electric field. With these computational details, an electronic device of interest can be designed and manufactured.

Metal oxide-based anisotropic particles such as patchy and Janus particles could be utilized as a potential hybrid material in drug delivery and medical diagnosis.

This page intentionally left blank

REFERENCES

Ameduri, B. (2009). "From vinylidene fluoride (VDF) to the applications of VDF-containing polymers and copolymers: recent developments and future trends." *Chem. Rev.,* 109**,** 6632-6686.

Arbatti, M., Shan, X. & Cheng, Z. Y. (2007). "Ceramic–polymer composites with high dielectric permittivity." *Adv. Mater.,* 19**,** 1369-1372.

Baek, Y., Lim, S., Kim, L. H., Park, S., Lee, S. W., Oh, T. H., Kim, S. H. & Park, C. E. (2016). "Al2O3/TiO2 nanolaminate gate dielectric films with enhanced electrical performances for organic field-effect transistors." *Org. Electron.,* 28**,** 139-146.

Bai, Y., Cheng, Z.-Y., Bharti, V., Xu, H. & Zhang, Q. (2000). "High-dielectric-constant ceramic-powder polymer composites." *Appl. Phys. Lett.,* 76**,** 3804-3806.

Bécu, S., Crémer, S. & Autran, J. (2006). "Capacitance non-linearity study in Al2O3 MIM capacitors using an ionic polarization model." *Microelectron. Eng.,* 83**,** 2422-2426.

Benvenho, A. R., Machado, W. S., Cruz-Cruz, I. & Hümmelgen, I. A. (2013). "Study of poly (3-hexylthiophene)/cross-linked PVA as semiconductor/insulator for low voltage organic field effect transistors." *J. Appl. Phys.,* 113**,** 214509.

Bergman, R., Alvarez, F., AlegríA, A. & Colmenero, J. (1998). "Dielectric relaxation in PMMA revisited." *J. Non-Cryst. Solids.* 235**,** 580-583.

Bettinger, C. J. & Bao, Z. (2010). "Organic thin-film transistors fabricated on resorbable biomaterial substrates." *Adv. Mater.,* 22**,** 651-655.

Bordi, F., Cametti, C. & Colby, R. H. (2004). "Dielectric spectroscopy and conductivity of polyelectrolyte solutions." *J. Phys.: Condens. Matter.* 16**,** R1423.

Brusso, B. & Chaparala, S. (2014). "The Evolution of Capacitors [History]." *IEEE Industry Applications Magazine.* 20**,** 8-12.

Chen, T., Lamm, M. H. & Glotzer, S. C. (2004). "Biomolecule-directed assembly of nanoscale building blocks studied via lattice Monte Carlo simulation."*J. chem. phys.* 121**,** 3919-3929.

Chen, Z. H., Li, H. F., Xie, G. Y. & Yang, K. (2018). "Core-shell structured Ag@C nanocables for flexible ferroelectric polymer nanodielectric materials with low percolation threshold and excellent dielectric properties." *Rsc Adv.* 8**,** 1-9.

Cheng, Z.-Y., Zhang, Q. & Bateman, F. B. (2002). "Dielectric relaxation behavior and its relation to microstructure in relaxor ferroelectric polymers: high-energy electron irradiated poly (vinylidene fluoride–trifluoroethylene) copolymers." *J Appl Phys.* 92**,** 6749-6755.

Chernyak, Y. (2006). "Dielectric permittivity, dipole moment, and solubility parameters of some cyclic acid esters." *J. Chem. Eng. Data.* 51**,** 416-418.

Chu, B., Zhou, X., Ren, K., Neese, B., Lin, M., Wang, Q., Bauer, F. & Zhang, Q. (2006). "A dielectric polymer with high electric energy density and fast discharge speed." *Science.* 313**,** 334-336.

Chung, S.-Y., Lee, S.-I., Choi, J.-H. & Choi, S.-Y. (2006). "Initial cation stoichiometry and current-voltage behavior in Sc-doped calcium copper titanate." *Appl. Phys. Lett.,* 89**,** 191907.

Cloet, V., Feys, J., Hühne, R., Hoste, S. & Van Driessche, I. (2009). "Thin La2Zr2O7 films made from a water-based solution." *J. Sol. Sta. Chem.* 182**,** 37-42.

Dang, Z.-M., Yuan, J.-K., Zha, J.-W., Zhou, T., Li, S.-T. & Hu, G.-H. (2012). "Fundamentals, processes and applications of high-permittivity polymer–matrix composites." *Prog. Mater. Sci..* 57**,** 660-723.

Dang, Z. M., Yuan, J. K., Yao, S. H. & Liao, R. J. (2013). "Flexible nanodielectric materials with high permittivity for power energy storage." *Adv. Mater.* 25**,** 6334-6365.

Debye, P. (1922). "Methods to determine the electrical and geometrical structure of molecules." *Nobel Lectures, Chemistry.* 1941**,** 383-401.

Deegan, R. D., Bakajin, O., Dupont, T. F., Huber, G., Nagel, S. R. & Witten, T. A. (1997). "Capillary flow as the cause of ring stains from dried liquid drops." *Nature.* 389**,** 827-829.

Dimitrakopoulos, C., Purushothaman, S., Kymissis, J., Callegari, A. & Shaw, J. (1999). "Low-voltage organic transistors on plastic comprising high-dielectric permittivity gate insulators." *Science.* 283**,** 822-824.

Doktycz, S. J. & Suslick, K. S. (1990). "Interparticle collisions driven by ultrasound." *Science.* 247**,** 1067-1069.

Dziaugys, A., Macutkevic, J., Svirskas, S., Juskenas, R., Wencka, M., Banys, J., Motria, S. & Vysochanskii, Y. (2015). "Maxwell–Wagner relaxation and anomalies of physical properties in Cu0. 15Fe1. 7PS3 mixed material." *J. Alloy Compd.* 650**,** 386-392.

Esro, M., Vourlias, G., Somerton, C., Milne, W. I. & Adamopoulos, G. (2015). "High-Mobility ZnO Thin Film Transistors Based on Solution-processed Hafnium Oxide Gate Dielectrics." *Adv. Funct. Mater.,* 25**,** 134-141.

Felderhof, B., Ford, G. & Cohen, E. (1983). "The Clausius-Mossotti formula and its nonlocal generalization for a dielectric suspension of spherical inclusions." *J. Stat. Phys.* 33**,** 241-260.

Feng, Y., Zhang, J., Hu, J., Li, S. & Peng, C. (2018a). "Significantly elevated dielectric and energy storage traits in boron nitride filled polymer nano-composites with topological structure." *Ele. Mater. Lett.* 14**,** 187-197.

Feng, Z., Hao, Y., Bi, M., Dai, Q. & Bi, K. (2018b). "Highly dispersive Ba 0.6 Sr 0.4 TiO 3 nanoparticles modified P (VDF-HFP)/PMMA composite films with improved energy storage density and efficiency." *IET Nanodielectrics.* 1**,** 60-66.

Gerhard-Multhaupt, R. (1987). "Poly (vinylidene fluoride): A piezo-, pyro-and ferroelectric polymer and its poling behaviour." *Ferroelectrics.* 75**,** 385-396.

Grieser, F. 1997. Sonochemistry in colloidal systems. *Stud. Surf. Sci. Catal.*: Elsevier.

Groner, M., Elam, J., Fabreguette, F. & George, S. M. (2002). "Electrical characterization of thin Al2O3 films grown by atomic layer deposition on silicon and various metal substrates." *Thin Solid Films.* 413**,** 186-197.

Guo, N., Dibenedetto, S. A., Kwon, D.-K., Wang, L., Russell, M. T., Lanagan, M. T., Facchetti, A. & Marks, T. J. (2007). "Supported metallocene catalysis for in situ synthesis of high energy density metal oxide nanocomposites." *J. Am. Chem. Soc.,* 129**,** 766-767.

Hannay, J. (1983). "The Clausius-Mossotti equation: an alternative derivation." *Eur. J. Phys.* 4**,** 141.

Ho, J., Jow, T. R. & Boggs, S. (2010). "Historical introduction to capacitor technology." *IEEE Electrical Insulation Magazine.* 26**,** 20-25.

Ho, J. S. & Greenbaum, S. G. (2018). "Polymer capacitor dielectrics for high temperature applications." *ACS Appl. Mater. Interfaces.* 10**,** 29189-29218.

Hoshina, T. (2013). "Size effect of barium titanate: fine particles and ceramics." *J. Ceram. Soc. Jpn.,* 121**,** 156-161.

Hu, G. X., Gao, F., Kong, J., Yang, S. J., Zhang, Q. Q., Liu, Z. T., Zhang, Y. & Sun, H. J. (2015). "Preparation and dielectric properties of poly(vinylidene fluoride)/Ba0.6Sr0.4TiO3 composites." *J Alloy Compd.* 619**,** 686-692.

Huang, X. & Jiang, P. (2015). "Core–shell structured high-k polymer nanocomposites for energy storage and dielectric applications." *Ad. Mater.* 27**,** 546-554.

Jang, J., Kang, H., Chakravarthula, H. C. N. & Subramanian, V. (2015). "Fully Inkjet-Printed Transparent Oxide Thin Film Transistors Using a Fugitive Wettability Switch." *Adv. Electron Mater.,* 1**,** 1500086.

Jayasundere, N. & Smith, B. (1993). "Dielectric permittivity for binary piezoelectric 0-3 composites." *J. App. Phys.* 73**,** 2462-2466.

Kahlaoui, M., Chefi, S., Inoubli, A., Madani, A. & Chefi, C. (2013). "Synthesis and electrical properties of co-doping with La3+, Nd3+, Y3+, and Eu3+ citric acid-nitrate prepared samarium-doped ceria ceramics." *Ceram. Int.,* 39**,** 3873-3879.

Kang, G.-W., Park, K.-M., Song, J.-H., Lee, C. & Hwang, D. (2005). "The electrical characteristics of pentacene-based organic field-effect transistors with polymer gate insulators." *Current Applied Physics.* 5**,** 297-301.

Kang, K., Kim, I.-D., Lim, M.-H., Kim, H.-G. & Hong, J.-M. (2008). "Annealing effect on dielectric and leakage current characteristics of Mn-doped Ba0. 6Sr0. 4TiO3 thin films as gate insulators for low voltage ZnO thin film transistor." *Thin Solid Films.* 516**,** 1218-1222.

Karaman, M., Kooi, S. E. & Gleason, K. K. (2008). "Vapor deposition of hybrid organic–inorganic dielectric bragg mirrors having rapid and reversibly tunable optical reflectance." *Chem. Mater.,* 20**,** 2262-2267.

Kepler, R. & Anderson, R. (1978). "Ferroelectricity in polyvinylidene fluoride." *J. Appl. Phys.,* 49**,** 1232-1235.

Khan, M. Z. R., Hasko, D., Saifullah, M. & Welland, M. (2008). "Characterization of a sol-gel based high-k dielectric field effect transistor for cryogenic operation." *J. Vac Sci & Tech B:* 26**,** 1887-1891.

Kharton, V. V., Yaremchenko, A. A., Naumovich, E. N. & Marques, F. M. (2000). "Research on the electrochemistry of oxygen ion conductors in the former Soviet Union." *J. Solid State Electrochem.,* 4**,** 243-266.

Khastgir, D., Maiti, H. & Bandyopadhyay, P. (1988). "Polystyrene-titania composite as a dielectric material." *Mater. Sci. Eng.,* 100**,** 245-253.

Kim, C.-H., Bae, J.-H., Lee, S.-D. & Choi, J. S. (2007a). "Fabrication of organic thin-film transistors based on high dielectric nanocomposite insulators." *Mol. Crys. Liq. Crys.* 471**,** 147-154.

Kim, C. S., Jo, S. J., Lee, S. W., Kim, W. J., Baik, H. K. & Lee, S. J. (2007b). "Surface-modified high-k oxide gate dielectrics for low-voltage high-performance pentacene thin-film transistors." *Adv. Funct. Mater.,* 17**,** 958-962.

Kim, K. M., Kim, J. C. & Ryu, K. S. (2006). "Characteristics of PVdF-HFP/TiO2 composite electrolytes prepared by a phase inversion technique using dimethyl acetamide solvent and water non-solvent." *Macromol Mater Eng.* 291**,** 1495-1502.

Kim, M.-G., Kanatzidis, M. G., Facchetti, A. & Marks, T. J. (2011a). "Low-temperature fabrication of high-performance metal oxide thin-film electronics via combustion processing." *Nature materials.* 10**,** 382-388.

Kim, S. J., Yoon, D. H., Rim, Y. S. & Kim, H. J. (2011b). "Low-temperature solution-processed ZrO2 gate insulators for thin-film transistors using high-pressure annealing." *Electrochem. Solid-State Lett.,* 14**,** E35-E37.

Ko, J., Kim, J., Park, S. Y., Lee, E., Kim, K., Lim, K.-H. & Kim, Y. S. (2014). "Solution-processed amorphous hafnium-lanthanum oxide gate insulator for oxide thin-film transistors." *J. Mater. Chem. C.* 2**,** 1050-1056.

Koops, C. (1951). "On the dispersion of resistivity and dielectric permittivity of some semiconductors at audiofrequencies." *Phys Rev.* 83**,** 121.

Kumar, R. V., Diamant, Y. & Gedanken, A. (2000). "Sonochemical synthesis and characterization of nanometer-size transition metal oxides from metal acetates." *Chem. Mater.,* 12**,** 2301-2305.

Lee, K.-H., Park, B. J., Choi, H. J., Park, J. & Choi, J. S. (2007). "Effect of surfactant on preparation of poly (4-vinylphenol)/titanium dioxide composite for a gate insulator of organic thin film transistors." *Molecular Crystals and Liquid Crystals.* 471**,** 173-179.

Lewis, T., Llewellyn, J., Van Der Sluijs, M., Freestone, J. & Hampton, R. A new model for electrical ageing and breakdown in dielectrics. Seventh International Conference on Dielectric Materials, Measurements and Applications (Conf. Publ. No. 430), 1996. IET, 220-224.

Li, Q., Chen, L., Gadinski, M. R., Zhang, S., Zhang, G., Li, H. U., Iagodkine, E., Haque, A., Chen, L.-Q. & Jackson, T. N. (2015). "Flexible high-temperature dielectric materials from polymer nanocomposites." *Nature.* 523**,** 576-579.

Liu, A., Liu, G., Zhu, H., Shin, B., Fortunato, E., Martins, R. & Shan, F. (2015). "Eco-friendly water-induced aluminum oxide dielectrics and their application in a hybrid metal oxide/polymer TFT." *RSC Advances.* 5**,** 86606-86613.

Liu, A., Zhu, H., Sun, H., Xu, Y. & Noh, Y. Y. (2018). "Solution Processed Metal Oxide High-κ Dielectrics for Emerging Transistors and Circuits." *Adv. Mater.,* 30**,** 1706364.

Lotierzo, A., Longbottom, B. W., Lee, W. H. & Bon, S. A. (2018). "Synthesis of Janus and Patchy Particles Using Nanogels as Stabilizers in Emulsion Polymerization." *ACS nano.* 13**,** 399-407.

Lovinger, A. J., Davis, G. T., Furukawa, T. & Broadhurst, M. G. (1982). "Crystalline forms in a copolymer of vinylidene fluoride and trifluoroethylene (52/48 mol %)." *Macromolecules.* 15**,** 323-328.

Luo, B., Wang, X., Wang, Y. & Li, L. (2014). "Fabrication, characterization, properties and theoretical analysis of ceramic/PVDF composite flexible films with high dielectric permittivity and low dielectric loss." *J. Mater. Chem. A.* 2**,** 510-519.

Luo, H., Zhang, D., Jiang, C., Yuan, X., Chen, C. & Zhou, K. (2015). "Improved dielectric properties and energy storage density of poly (vinylidene fluoride-co-

hexafluoropropylene) nanocomposite with hydantoin epoxy resin coated BaTiO3." *ACS App. Mater. Interfaces.* 7**,** 8061-8069.

Luo, H., Zhou, X., Ellingford, C., Zhang, Y., Chen, S., Zhou, K., Zhang, D., Bowen, C. R. & Wan, C. (2019). "Interface design for high energy density polymer nanocomposites." *Chem. Soc Rev.*

Mao, Y., Mao, S., Ye, Z.-G., Xie, Z. & Zheng, L. (2010). "Size-dependences of the dielectric and ferroelectric properties of BaTiO 3/polyvinylidene fluoride nanocomposites." *J. Appl. Phys.,* 108**,** 014102.

Maxwell, J. C. (1865). "VIII. A dynamical theory of the electromagnetic field." *Philosophical transactions of the Royal Society of London.* 459-512.

Mccloskey, B. D. (2015). Expanding the Ragone plot: Pushing the limits of energy storage. ACS Publications.

Meeporn, K. & Thongbai, P. (2020). "Flexible La1. 5Sr0. 5NiO4/Poly (vinylidene fluoride) composites with an ultra high dielectric permittivity: A comparative study." *Compos Part B: Engineering.* 184**,** 107738.

Mehandru, R., Luo, B., Kim, J., Ren, F., Gila, B., Onstine, A., Abernathy, C., Pearton, S., Gotthold, D. & Birkhahn, R. (2003). "AlGaN/GaN metal–oxide–semiconductor high electron mobility transistors using Sc 2 O 3 as the gate oxide and surface passivation." *Appl. Phys. Lett.,* 82**,** 2530-2532.

Naegele, D. & Yoon, D. (1978). "Orientation of crystalline dipoles in poly (vinylidene fluoride) films under electric field." *Appl. Phys. Lett.,* 33**,** 132-134.

Nan, C.-W., Shen, Y. & Ma, J. (2010). "Physical properties of composites near percolation." *Annual Rev. Mater. Res.* 40**,** 131-151.

Nisa, V., Rajesh, S., Murali, K., Priyadarsini, V., Potty, S. & Ratheesh, R. (2008). "Preparation, characterization and dielectric properties of temperature stable SrTiO3/PEEK composites for microwave substrate applications." *Compos. Sci. Technol.,* 68**,** 106-112.

Noh, H., Seol, Y., Kim, S. & Lee, N.-E. (2008). "Mechanically flexible low-leakage nanocomposite gate dielectrics for flexible organic thin-film transistors." *Electrochem. Solid-State Lett.,* 11**,** H218-H221.

Norrman, K., Ghanbari-Siahkali, A. & Larsen, N. (2005). "6 Studies of spin-coated polymer films." *Annual Reports Section" C"(Physical Chemistry).* 101**,** 174-201.

Panda, D. & Tseng, T.-Y. (2013). "Growth, dielectric properties, and memory device applications of ZrO2 thin films." *Thin Solid Films.* 531**,** 1-20.

Pasquarelli, R. M., Ginley, D. S. & O'hayre, R. (2011). "Solution processing of transparent conductors: from flask to film." *Chem. Soc. Rev.,* 40**,** 5406-5441.

Pastorczak, M., Kozanecki, M. & Ulanski, J. (2009). "Water–Polymer interactions in PVME hydrogels–Raman spectroscopy studies." *Polymer.* 50**,** 4535-4542.

Pawar, A. B. & Kretzschmar, I. (2009). "Multifunctional patchy particles by glancing angle deposition." *Langmuir.* 25**,** 9057-9063.

Pei, Z., Pereira, L., Gonçalves, G., Barquinha, P., Franco, N., Alves, E., Rego, A., Martins, R. & Fortunato, E. (2009). "Room-Temperature Cosputtered HfO2–Al2O3 Multicomponent Gate Dielectrics." *Electrochem. Solid-State Lett.,* 12**,** G65-G68.

Peng, S., Yang, X., Yang, Y., Wang, S., Zhou, Y., Hu, J., Li, Q. & He, J. (2019). "Direct detection of local electric polarization in the interfacial region in ferroelectric polymer nanocomposites." *Advanced Materials.* 31**,** 1807722.

Philip, J., Punnoose, A., Kim, B., Reddy, K., Layne, S., Holmes, J., Satpati, B., Leclair, P., Santos, T. & Moodera, J. (2006). "Carrier-controlled ferromagnetism in transparent oxide semiconductors." *Nature materials.* 5**,** 298-304.

Pinjari, D. V. & Pandit, A. B. (2011). "Room temperature synthesis of crystalline CeO2 nanopowder: advantage of sonochemical method over conventional method." *Ultrason. Sonochem.,* 18**,** 1118-1123.

Pötschke, P., Dudkin, S. M. & Alig, I. (2003). "Dielectric spectroscopy on melt processed polycarbonate—multiwalled carbon nanotube composites." *Polymer.* 44**,** 5023-5030.

Qian, D., Jiang, J. & Hansen, P. L. (2003). "Preparation of ZnO nanocrystals via ultrasonic irradiation." *Chem. Commun.***,** 1078-1079.

Rabuffi, M. & Picci, G. (2002). "Status quo and future prospects for metallized polypropylene energy storage capacitors." *IEEE transactions on plasma science.* 30**,** 1939-1942.

Rahimabady, M., Mirshekarloo, M. S., Yao, K. & Lu, L. (2013a). "Dielectric behaviors and high energy storage density of nanocomposites with core-shell BaTiO3@TiO2 in poly(vinylidene fluoride-hexafluoropropylene)." *Phys Chem Chem Phys : PCCP.* 15**,** 16242-16248.

Rahimabady, M., Mirshekarloo, M. S., Yao, K. & Lu, L. (2013b). "Dielectric behaviors and high energy storage density of nanocomposites with core–shell BaTiO 3@ TiO 2 in poly (vinylidene fluoride-hexafluoropropylene)." *Phys Chem Chem Phys.* 15**,** 16242-16248.

Randall, C., Newnham, R. & Cross, L. (2004). "History of the first ferroelectric oxide, BaTiO3." *Materials Research Institute, The Pennsylvania State University, University Park, Pa, USA.* 1-11.

Richards, W. T. & Loomis, A. L. (1927). "The chemical effects of high frequency sound waves I. A preliminary survey." *J. Am. Chem. Soc.,* 49**,** 3086-3100.

Ruiz-Hitzky, E., Aranda, P., Darder, M. & Ogawa, M. (2011). "Hybrid and biohybrid silicate based materials: molecular vs. block-assembling bottom–up processes." *Chem. Soc. Rev.* 40**,** 801-828.

Rysselberghe, P. V. (2002). "Remarks concerning the Clausius-Mossotti law."*J. Phys. Chem.* 36**,** 1152-1155.

Samant, S. P., Grabowski, C. A., Kisslinger, K., Yager, K. G., Yuan, G., Satija, S. K., Durstock, M. F., Raghavan, D. & Karim, A. (2016). "Directed self-assembly of block copolymers for high breakdown strength polymer film capacitors." *ACS applied materials & interfaces.* 8**,** 7966-7976.

Schneller, T., Waser, R., Kosec, M. & Payne, D. (2013). *Chemical solution deposition of functional oxide thin films*. Springer.

Scholz, F. (2011). "From the Leiden jar to the discovery of the glass electrode by Max Cremer." *J. Solid State Electrochem.,* 15**,** 5-14.

Shannon, R. D. (1976). "Revised effective ionic radii and systematic studies of interatomic distances in halides and chalcogenides." *Acta crys. section A:* 32**,** 751-767.

Shen, Y., Gu, A., Liang, G. & Yuan, L. (2010). "High performance CaCu3Ti4O12/cyanate ester composites with excellent dielectric properties and thermal resistance." *Compos. Part A: App. Sci. Manuf.* 41**,** 1668-1676.

Shen, Y., Shen, D., Zhang, X., Jiang, J., Dan, Z., Song, Y., Lin, Y., Li, M. & Nan, C.-W. (2016). "High energy density of polymer nanocomposites at a low electric field induced by modulation of their topological-structure." *J Mater Chem A.* 4**,** 8359-8365.

Skryabin, I., Radchik, A., Moses, P. & Smith, G. (1997). "The consistent application of Maxwell–Garnett effective medium theory to anisotropic composites." *Appl. Phys. Lett.,* 70**,** 2221-2223.

Sousa, R., Nunes-Pereira, J., Ferreira, J., Costa, C., Machado, A., Silva, M. & Lanceros-Mendez, S. (2014). "Microstructural variations of poly (vinylidene fluoride co-hexafluoropropylene) and their influence on the thermal, dielectric and piezoelectric properties." *Polym. Test.,* 40**,** 245-255.

Sudeep, P. & Emrick, T. (2007). "Polymer-Nanoparticle Composites: Preparative Methods and Electronically Active Materials." *Polymer Reviews.* 47**,** 155-163.

Suematsu, K., Arimura, M., Uchiyama, N., Saita, S. & Makino, T. (2016). "Synthesis of BaTiO3/polymer composite ink to improve the dielectric properties of thin films." *Compos Part B-Eng.* 104**,** 80-86.

Sung, S., Park, S., Lee, W.-J., Son, J., Kim, C.-H., Kim, Y., Noh, D. Y. & Yoon, M.-H. (2015). "Low-voltage flexible organic electronics based on high-performance sol–gel titanium dioxide dielectric." *ACS Appl. Mater. Interfaces.* 7**,** 7456-7461.

Suslick, K. S. (1990). "Sonochemistry." *Science.* 247**,** 1439-1445.

Tan, D. Q. (2019). "Review of Polymer-Based Nanodielectric Exploration and Film Scale-Up for Advanced Capacitors." *Adv. Funct. Mater.,* 1808567.

Tanaka, T., Kozako, M., Fuse, N. & Ohki, Y. (2005). "Proposal of a multi-core model for polymer nanocomposite dielectrics." *IEEE transactions on dielectrics and electrical insulation.* 12**,** 669-681.

Tardy, J., Erouel, M., Deman, A., Gagnaire, A., Teodorescu, V., Blanchin, M., Canut, B., Barau, A. & Zaharescu, M. (2007). "Organic thin film transistors with HfO2 high-

k gate dielectric grown by anodic oxidation or deposited by sol–gel." *Microelectronics reliability.* 47**,** 372-377.

Tarnuzzer, R. W., Colon, J., Patil, S. & Seal, S. (2005). "Vacancy engineered ceria nanostructures for protection from radiation-induced cellular damage." *Nano Lett.,* 5**,** 2573-2577.

Thakur, V. K. & Gupta, R. K. (2016). "Recent progress on ferroelectric polymer-based nanocomposites for high energy density capacitors: synthesis, dielectric properties, and future aspects." *Chem. Rev.,* 116**,** 4260-4317.

Tian, B. B., Liu, Y., Chen, L. F., Wang, J. L., Sun, S., Shen, H., Sun, J. L., Yuan, G. L., Fusil, S. & Garcia, V. (2015). "Space-charge effect on electroresistance in metal-ferroelectric-metal capacitors." *Scientific reports.* 5**,** 1-9.

Triyoso, D. H., Hegde, R. I., Jiang, J., Schaeffer, J. K. & Raymond, M. V. (2007). "Improved Electrical Properties of ALD $\hbox {Hf} _ {x}\hbox {Zr} _ {1-x}\hbox {O} _ {2} $ Dielectrics Deposited on Ultrathin PVD Zr Underlayer." *IEEE electron device letters.* 29**,** 57-59.

Tseng, G. Y. & Ellenbogen, J. C. (2001). "Toward nanocomputers." *Science.* 294**,** 1293-1294.

Tyunina, M. & Levoska, J. (2006). "Application of the interface capacitance model to thin-film relaxors and ferroelectrics." *Appl. Phys. Lett.,* 88**,** 262904.

Ushakov, S. V., Brown, C. E. & Navrotsky, A. (2004). "Effect of La and Y on crystallization temperatures of hafnia and zirconia." *J. Mater. Res.,* 19**,** 693-696.

Vanpoucke, D. E., Bultinck, P., Cottenier, S., Van Speybroeck, V. & Van Driessche, I. (2014). "Aliovalent doping of CeO2: DFT study of oxidation state and vacancy effects." *J. Mater. Chem. A.* 2**,** 13723-13737.

Vold, T. G. (1993). "An introduction to geometric calculus and its application to electrodynamics." *Am J Phys.* 61**,** 505-513.

Walther, A., Drechsler, M., Rosenfeldt, S., Harnau, L., Ballauff, M., Abetz, V. & MüLler, A. H. (2009). "Self-assembly of Janus cylinders into hierarchical superstructures." *J. Am. Chem. Soc.* 131**,** 4720-4728.

Wang, B., Huang, W., Chi, L., Al-Hashimi, M., Marks, T. J. & Facchetti, A. (2018). "High-k gate dielectrics for emerging flexible and stretchable electronics." *Chem. Rev.,* 118**,** 5690-5754.

Wang, B., Yu, X., Guo, P., Huang, W., Zeng, L., Zhou, N., Chi, L., Bedzyk, M. J., Chang, R. P. & Marks, T. J. (2016). "Solution-processed all-oxide transparent high-performance transistors fabricated by spray-combustion synthesis." *Adv. Electron Mater.,* 2**,** 1500427.

Wang, G., Huang, X. & Jiang, P. (2015). "Tailoring dielectric properties and energy density of ferroelectric polymer nanocomposites by high-k nanowires." *ACS app. mater. interfaces.* 7**,** 18017-18027.

Wang, Z., Ren, X., Leung, C. W., Shi, S. & Chan, P. K. L. (2013). "A UV-ozone treated amorphous barium–strontium titanate dielectric thin film for low driving voltage flexible organic transistors." *J. Mater. Chem. C.* 1**,** 3825-3832.

Xie, L., Huang, X., Huang, Y., Yang, K. & Jiang, P. (2013). "Core@ double-shell structured BaTiO3–polymer nanocomposites with high dielectric permittivity and low dielectric loss for energy storage application."*J. Phy. Chem C.* 117**,** 22525-22537.

Xu, H., Zeiger, B. W. & Suslick, K. S. (2013). "Sonochemical synthesis of nanomaterials." *Chem. Soc. Rev.,* 42**,** 2555-2567.

Yang, C., Song, H. S. & Liu, D. B. (2013). "Effect of coupling agents on the dielectric properties of CaCu3Ti4O12/PVDF composites." *Compos Part B-Eng.* 50**,** 180-186.

Yang, K., Huang, X., Xie, L., Wu, C., Jiang, P. & Tanaka, T. (2012). "Core–shell structured polystyrene/BaTiO3 hybrid nanodielectrics prepared by in situ RAFT polymerization: a route to high dielectric permittivity and low loss materials with weak frequency dependence." *Macro. rapid comm.* 33**,** 1921-1926.

Yeo, Y.-C., King, T.-J. & Hu, C. (2002). "Direct tunneling leakage current and scalability of alternative gate dielectrics." *Appl. Phys. Lett.,* 81**,** 2091-2093.

Yoon, K. H., Noh, J. S., Kwon, C. H. & Muhammed, M. (2006). "Photocatalytic behavior of TiO2 thin films prepared by sol–gel process." *Mater. Chem. Phys.,* 95**,** 79-83.

Youm, M., Sim, H. S., Jeon, H., Kim, S.-I. & Kim, Y. T. (2003). "Metal oxide semiconductor field effect transistor characteristics with iridium gate electrode on atomic layer deposited ZrO2 high-k dielectrics." *Jap. j. app. phys.* 42**,** 5010.

Zhang, G., Wang, D. & Möhwald, H. (2005). "Decoration of microspheres with gold nanodots—giving colloidal spheres valences." *Angewandte Chemie.* 117**,** 7945-7948.

Zhang, X., Chen, W., Wang, J., Shen, Y., Gu, L., Lin, Y. & Nan, C.-W. (2014). "Hierarchical interfaces induce high dielectric permittivity in nanocomposites containing TiO 2@ BaTiO 3 nanofibers." *Nanoscale.* 6**,** 6701-6709.

Zhang, Z. & Glotzer, S. C. (2004). "Self-assembly of patchy particles." *Nano Letters.* 4**,** 1407-1413.

Zhao, X. Y. & Liu, H. J. (2010). "Review of polymer materials with low dielectric permittivity." *Polym. Int.,* 59**,** 597-606.

Zhou, Y., Kojima, N. & Sasaki, K. (2008). "Growth and dielectric properties of tetragonal ZrO2 films by limited reaction sputtering." *J. Phys. D: Appl. Phys.,* 41**,** 175414.

This page intentionally left blank

RESEARCH PUBLICATIONS

PATENTS

Kishor Kumar M. J. Pavan Pujar, and Jagannathan T. Kalathi, Method and system for preparing a lanthanum zirconium based dielectric ink for microelectronics, *Indian patent Granted.* Grant Number:347616 dated on 24-09-2020.

Kishor Kumar M. J. and Jagannathan T. Kalathi, Method and composition for fabricating a high-k dielectric material, *Indian patent filed*. Application Number: 201941047909 dated 23rd November 2019.

PEER-REVIEWED JOURNAL PUBLICATIONS

Kishor Kumar M. J. and Jagannathan T. Kalathi (2020). Investigation on the dielectric performance of PVDF-HFP/LZO composites, Journal of Alloys and Compounds, 843, 155889.

Kishor Kumar M. J. and Jagannathan T. Kalathi (2019). Interface dominated dielectric response of PS-Fe$_3$O$_4$ patchy microspheres, Langmuir 35, 13923-13933.

Kishor Kumar M. J. and Jagannathan T. Kalathi (2019). PMMA-LZO composite dielectric film with an improved energy storage density, Journal of Electronic Materials 48, 7654.

Kishor Kumar M. J. and Jagannathan T. Kalathi (2018). Low-temperature sonochemical synthesis of high dielectric Lanthanum doped Cerium oxide nanopowder, Journal of Alloys and Compounds 748, 348-354.

Pavan Pujar, **Kishor Kumar M. J**, Muhammad Naqi, Srinivas Gandla, Hae Won Cho, Sung Hyeon Jung, Hyung Koun Cho, Jagannathan T Kalathi, Sunkook Kim (2020), High-intensity ultrasound-assisted low-temperature formulation of lanthanum zirconium oxide nanodispersion for thin-film transistors, ACS Applied Materials & Interfaces 12, 44926-44933.

CONFERENCE PRESENTATIONS

Kishor Kumar M. J. and Jagannathan T. Kalathi. "Sonochemical preparation of LZO dielectric ink for thin-film capacitor" IUMRS-ICEM-2018, Daejeon DCC, South Korea.

Kishor Kumar M. J. and Jagannathan T. Kalathi. "PMMA-LZO composite dielectric film with an improved energy storage density" RACEEE-2019, SSN College, Chennai.

Kishor Kumar M. J, and Jagannathan T. Kalathi. "A facile sonochemical synthesis of La_2O_3" CHEMCON 2016, AC Tech, Anna University and IIT Madras (**Best paper award**).

Jagannathan T. Kalathi, **Kishor Kumar M. J.,** Satabdi Hazarika, Sanjeevan G Akshay. "Sonochemical fabrication of polystyrene-iron oxide composite particles for thin film dielectric ICSM 2018, December 2018, MNIT, Jaipur.

BIODATA

KISHOR KUMAR M. J.

✉ kish.divine@gmail.com   📅 Doctoral Student at NITK

🎁 November 26, 1991   📞 +91-9113556225

📍 Mangalore, Karnataka

🎓 **EDUCATION** ─────────────────────────

Doctor of Philosophy (Ph.D.)   July 2015 to June 2020
Chemical Engineering, National Institute of
Technology, Karnataka, (NITK) Surathkal, India

Masters of Technology (M.Tech.)   June 2013 - July 2015

Chemical Engineering, Manipal Institute of
Technology (MIT) Manipal, Karnataka, India

Bachelor of Engineering (BE)   July 2009 - July 2013
Polymer Science and Technology
Sri Jayachamarajendra College of Engineering,
Mysuru, Karnataka, India

🏅 **AWARDS & HONOURS** ─────────────────────

1. **Young Scientist Award** *from* **DST-SERB**, **Government of India** (*Grant Number: ITS/2018/002921*) to attend an International conference IUMRS-ICEM 2018, DCC, Daejeon, **South Korea**.
2. **Elected Associate Member** of the **Indian Institute of Chemical Engineers** in 2017 (IIChe) LAM-61772.
3. **Best Research Paper/Presentation Award** from **IIT Madras**-AC Tech during **CHEMCON-2016**, Chennai.